

SENSORS & TRANSDUCERS

ISSN 1726-5479

vol. 208

1/17

**Nanosensors and Sensors
in Medical Applications**

International Frequency Sensor Association Publishing



Sensors & Transducers

**International Official Open Access Journal of the
International Frequency Sensor Association (IFSA)
Devoted to Research and Development
of Sensors and Transducers**

Volume 208, Issue 1, January 2017

Editor-in-Chief

Prof., Dr. Sergey Y. YURISH



IFSA Publishing: Barcelona • Toronto

Sensors & Transducers is an open access journal which means that all content (article by article) is freely available without charge to the user or his/her institution. Users are allowed to read, download, copy, distribute, print, search, or link to the full texts of the articles, or use them for any other lawful purpose, without asking prior permission from the publisher or the author. This is in accordance with the BOAI definition of open access. Authors who publish articles in *Sensors & Transducers* journal retain the copyrights of their articles. The *Sensors & Transducers* journal operates under the Creative Commons License CC-BY.

Notice: No responsibility is assumed by the Publisher for any injury and/or damage to persons or property as a matter of products liability, negligence or otherwise, or from any use or operation of any methods, products, instructions or ideas contained in the material herein.

Published by International Frequency Sensor Association (IFSA) Publishing. Printed in the USA.





Editors-in-Chief: Professor, Dr. Sergey Y. Yurish, tel.: +34 696067716, e-mail: editor@sensorsportal.com

Editors for Western Europe

Meijer, Gerard C.M., Delft Univ. of Technology, The Netherlands
Ferrari, Vittorio, Università di Brescia, Italy
Mescheder, Ulrich, Univ. of Applied Sciences, Furtwangen, Germany

Editor for Eastern Europe

Sachenko, Anatoly, Ternopil National Economic University, Ukraine

Editors for North America

Katz, Evgeny, Clarkson University, USA
Datskos, Panos G., Oak Ridge National Laboratory, USA
Fabien, J. Josse, Marquette University, USA

Editor for Africa

Maki K., Habib, American University in Cairo, Egypt

Editors South America

Costa-Felix, Rodrigo, Inmetro, Brazil
Walsole de Reca, Noemi Elisabeth, CINSO-CITEDEF
UNIDEF (MINDEF-CONICET), Argentina

Editors for Asia

Ohyama, Shinji, Tokyo Institute of Technology, Japan
Zhengbing, Hu, Huazhong Univ. of Science and Technol., China
Li, Gongfa, Wuhan Univ. of Science and Technology, China

Editor for Asia-Pacific

Mukhopadhyay, Subhas, Massey University, New Zealand

Editorial Board

Abdul Rahim, Ruzairi, Universiti Teknologi, Malaysia
Abramchuk, George, Measur. Tech. & Advanced Applications, Canada
Aluri, Geetha S., Globalfoundries, USA
Ascoli, Giorgio, George Mason University, USA
Atalay, Selcuk, Inonu University, Turkey
Atghiaee, Ahmad, University of Tehran, Iran
Augutis, Vygtantas, Kaunas University of Technology, Lithuania
Ayesh, Aladdin, De Montfort University, UK
Baliga, Shankar, B., General Monitors, USA
Barlingay, Ravindra, Larsen & Toubro - Technology Services, India
Basu, Sukumar, Jadavpur University, India
Booranawong, Apidet, Prince of Songkla University, Thailand
Bousbia-Salah, Mounir, University of Annaba, Algeria
Bouvet, Marcel, University of Burgundy, France
Campanella, Luigi, University La Sapienza, Italy
Carvalho, Vitor, Minho University, Portugal
Changhai, Ru, Harbin Engineering University, China
Chen, Wei, Hefei University of Technology, China
Cheng-Ta, Chiang, National Chia-Yi University, Taiwan
Cherstvy, Andrey, University of Potsdam, Germany
Chung, Wen-Yaw, Chung Yuan Christian University, Taiwan
Cortes, Camilo A., Universidad Nacional de Colombia, Colombia
D'Amico, Arnaldo, Università di Tor Vergata, Italy
De Stefano, Luca, Institute for Microelectronics and Microsystem, Italy
Ding, Jianning, Changzhou University, China
Djordjevic, Alexandar, City University of Hong Kong, Hong Kong
Donato, Nicola, University of Messina, Italy
Dong, Feng, Tianjin University, China
Erkmen, Aydan M., Middle East Technical University, Turkey
Fezari, Mohamed, Badji Mokhtar Annaba University, Algeria
Gaura, Elena, Coventry University, UK
Gole, James, Georgia Institute of Technology, USA
Gong, Hao, National University of Singapore, Singapore
Gonzalez de la Rosa, Juan Jose, University of Cadiz, Spain
Goswami, Amarjyoti, Kaziranga University, India
Guillet, Bruno, University of Caen, France
Hadjiloucas, Sillas, The University of Reading, UK
Hao, Shiyang, Michigan State University, USA
Hui, David, University of New Orleans, USA
Jaffrezic-Renault, Nicole, Claude Bernard University Lyon 1, France
Jamil, Mohammad, Qatar University, Qatar
Kaniusas, Eugenijus, Vienna University of Technology, Austria
Kim, Min Young, Kyungpook National University, Korea
Kumar, Arun, University of Delaware, USA
Lay-Ekuakille, Aime, University of Lecce, Italy
Li, Fengyuan, HARMAN International, USA
Li, Jingsong, Anhui University, China
Li, Si, GE Global Research Center, USA
Lin, Paul, Cleveland State University, USA
Liu, Aihua, Chinese Academy of Sciences, China
Liu, Chenglian, Long Yan University, China
Liu, Fei, City College of New York, USA
Mahadi, Muhammad, University Tun Hussein Onn Malaysia, Malaysia

Mansor, Muhammad Naufal, University Malaysia Perlis, Malaysia
Marquez, Alfredo, Centro de Investigacion en Materiales Avanzados, Mexico
Mishra, Vivekanand, National Institute of Technology, India
Moghavvemi, Mahmoud, University of Malaya, Malaysia
Morello, Rosario, University "Mediterranea" of Reggio Calabria, Italy
Mulla, Imtiaz Sirajuddin, National Chemical Laboratory, Pune, India
Nabok, Aleksey, Sheffield Hallam University, UK
Neshkova, Milka, Bulgarian Academy of Sciences, Bulgaria
Passaro, Vittorio M. N., Politecnico di Bari, Italy
Patil, Devidas Ramrao, R. L. College, Parola, India
Penza, Michele, ENEA, Italy
Pereira, Jose Miguel, Instituto Politecnico de Seteбал, Portugal
Pillarsetti, Anand, Sensata Technologies Inc, USA
Pogacnik, Lea, University of Ljubljana, Slovenia
Pullini, Daniele, Centro Ricerche FIAT, Italy
Qiu, Liang, Avago Technologies, USA
Reig, Candid, University of Valencia, Spain
Restivo, Maria Teresa, University of Porto, Portugal
Rodríguez Martínez, Angel, Universidad Politécnica de Cataluña, Spain
Sadana, Ajit, University of Mississippi, USA
Sadeghian Marnani, Hamed, TU Delft, The Netherlands
Sapozhnikova, Ksenia, D. I. Mendeleyev Institute for Metrology, Russia
Singhal, Subodh Kumar, National Physical Laboratory, India
Shah, Kriyang, La Trobe University, Australia
Shi, Wendian, California Institute of Technology, USA
Shmaliy, Yuriy, Guanajuato University, Mexico
Song, Xu, An Yang Normal University, China
Srivastava, Arvind K., Systron Donner Inertial, USA
Stefanescu, Dan Mihai, Romanian Measurement Society, Romania
Sumriddetchajorn, Sarun, Nat. Electr. & Comp. Tech. Center, Thailand
Sun, Zhiqiang, Central South University, China
Sysoev, Victor, Saratov State Technical University, Russia
Thirunavukkarasu, I., Manipal University Karnataka, India
Thomas, Sadiq, Heriot Watt University, Edinburgh, UK
Tian, Lei, Xidian University, China
Tianxing, Chu, Research Center for Surveying & Mapping, Beijing, China
Vanga, Kumar L., ePack, Inc., USA
Vazquez, Carmen, Universidad Carlos III Madrid, Spain
Wang, Jiangping, Xian Shiyu University, China
Wang, Peng, Qualcomm Technologies, USA
Wang, Zongbo, University of Kansas, USA
Xu, Han, Measurement Specialties, Inc., USA
Xu, Weihe, Brookhaven National Lab, USA
Xue, Ning, Agiltron, Inc., USA
Yang, Dongfang, National Research Council, Canada
Yang, Shuang-Hua, Loughborough University, UK
Yaping Dan, Harvard University, USA
Yue, Xiao-Guang, Shanxi University of Chinese Traditional Medicine, China
Xiao-Guang, Yue, Wuhan University of Technology, China
Zakaria, Zulkarnay, University Malaysia Perlis, Malaysia
Zhang, Weiping, Shanghai Jiao Tong University, China
Zhang, Wenming, Shanghai Jiao Tong University, China
Zhang, Yudong, Nanjing Normal University China

Contents

Volume 208
Issue 1
January 2017

www.sensorsportal.com

ISSN 2306-8515
e-ISSN 1726-5479

Research Articles

Gas Sensors Built with Nanomaterials and Provided with a Heating Double Purpose Hot-plate <i>Cristian L. Arrieta, Mario F. Bianchetti, Claudio A. Gillari, Lidia T. Alaniz, Héctor A. Lacomí, Matías A. Marando and Noemí E. Walsöe de Reca</i>	1
Simple Colorimetric DNA Biosensor Based on Gold Nanoparticles for Pork Adulteration Detection in Processed Meats <i>Bambang Kuswandi, Agus A Gani, Nia Kristiningrum and Musa Ahmad</i>	7
Surface Stress Effects on the Electrostatic Pull-in Instability of Nanomechanical Systems <i>Hamed Sadeghian</i>	14
Trajectory Tracking Optimal Control for Nonholonomic Mobile Robot <i>Jianwei Ma, Jiayu Shi and Haitao Zhang</i>	22
Photoplethysmography Based Mental Stress Analysis Algorithm and System for Human Wellbeing Life <i>Jong-Ha Lee</i>	28
Fuzzy System of Diagnosing in Oncology Telemedicine <i>Oleh Berezsky, Serhiy Verbovy, Lesia Dubchak and Tamara Datsko</i>	32
Non-rigid Point Matching using Topology Preserving Constraints for Medical Computer Vision <i>Jong-Ha Lee</i>	39
Regions Matching Algorithms Analysis to Quantify the Image Segmentation Results <i>Oleh Berezsky, Grygory Melnyk, Yuriy Batko and Oleh Pitsun</i>	44
Evaluating Image Precision of Acoustical Imaging Diffraction by Focused Ultrasound Beam <i>Jinwen Ding, Dewen Zheng, Han Ding, Kang LI, Qichen Ma, Guochao He, Jingjing Liu and Junhua Chen</i>	51

Authors are encouraged to submit article in MS Word (doc) and Acrobat (pdf) formats
by e-mail: editor@sensorsportal.com. Please visit journal's webpage with preparation instructions:
<http://www.sensorsportal.com/HTML/DIGEST/Submition.htm>



3rd International Conference on Sensors and Electronic Instrumentation Advances

20-22 September 2017
Moscow, Russia



The 3rd International Conference on Sensors and Electronic Instrumentation Advances (SEIA' 2017) is a forum for presentation, discussion, and exchange of information and latest research and development results in both theoretical and experimental research in sensors, transducers and their related fields. It brings together researchers, developers, and practitioners from diverse fields including international scientists and engineers from academia, research institutes, and companies to present and discuss the latest results in the field of sensors and measurements.

The conference is organized by the International Frequency Sensor Association (IFSA) and Asian Society of Applied Mathematics and Engineering (ASAME) in technical cooperation with National Research Center Kurchatov Institute and National Research Nuclear University (both from Moscow, Russia).

The conference is focusing any significant breakthrough and innovation in Sensors, Electronics, Measuring Instrumentation and Transducers Engineering Advances and its applications. Topics of Interest include any aspects of:

- Sensor Technology;
- Instruments and Measuring Technology.

Submission (2-page abstract) 20 March 2017
Notification of acceptance 20 April 2017
Registration 20 May 2017
Camera Ready 30 June 2017

Contribution Types:

Regular papers
Posters

One event - three publications !

1. All registered abstracts will be published in the conference proceedings.
2. Selected extended papers will be published in Sensors & Transducers journal.
3. The best full-page papers will be recommended to extend to book chapters for 'Advances in Sensors: Reviews' Book Series.

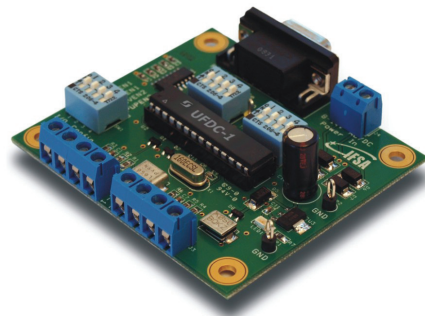
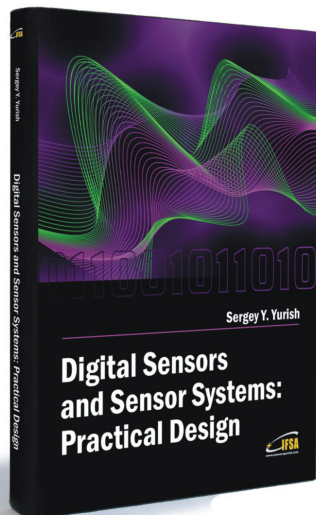


http://www.sensorsportal.com/SEIA_2017/

Digital Sensors and Sensor Systems: Practical Design

and

Development Board
EVAL UFDC-1/UFDC-1M-16



Buy book and Evaluation board together. **Save 30.00 EUR.**

Development Board EVAL UFDC-1 / UFDC-1M-16

Full-featured development kit for the Universal Frequency-to-Digital Converters UFDC-1 and UFDC-1M-16. 2 channel, 16 measuring modes, high metrological performance, RS232/USB interface, master and slave communication modes. On-board frequency reference (quartz crystal oscillator). Operation from 8 to 14 V AC/DC. Development board software is included.

All existing frequency, period, duty-cycle, time interval, pulse-width modulated, pulse number and phase-shift output sensors and transducers can be directly connected to this 2-channel DAQ system. The user can connect TTL-compatible sensors' outputs to the Development Board, measure any output frequency-time parameters, and test out the sensor systems functions.

Applications:

- Digital sensors and sensor systems
- Smart sensors systems
- Data Acquisition for frequency-time parameters of electric signals
- Frequency counters
- Tachometers and tachometric systems
- Virtual instruments
- Educational process in sensors and measurements
- Remote laboratories and distance education

Order online:

http://www.sensorsportal.com/HTML/BOOKSTORE/Digital_Sensors_and_Board.htm

Gas Sensors Built with Nanomaterials and Provided with a Heating Double Purpose Hot-plate

^{1,2} Cristian L. ARRIETA, ³ Mario F. BIANCHETTI,
¹ Claudio A. GILLARI, ¹ Lidia T. ALANIZ, ² Héctor A. LACOMI,
² Matías A. MARANDO and ³ Noemí E. WALSÖE DE RECA

¹ Microelectronics Division, DEA-CITEDEF, Villa Martelli, Bs.As., Argentina

² Electronics Dept. (SyCE), National Technology University UTN FRH, Paris 532, (1706)
Mariano J. Haedo, Prov. Bs.As., Argentina

³ DEINSO-Materials Department-CITEDEF (UNIDEF-MINDEF-CONICET),
Juan Bautista de La Salle 4387 (B1603ALO). Villa Martelli, Prov. Bs. As., Argentina

³ Tel.: 54 11 4709-8100, fax: 54 11 4709-8158

E-mail: walsoe@citedef.gob.ar, carrieta@citedef.gob.ar

Received: 4 October 2016 /Accepted: 30 December 2016 /Published: 31 January 2017

Abstract: Pure or doped SnO₂, has been used to build resistive type gas sensors from several decades. This subject has been retaken using pure or doped nanocrystalline SnO₂ to build the sensors, finding considerable advantages in devices performance. The sensors working temperature (Tw) decreases from (350-450) °C to (180-200) °C in comparison with that of devices built with microcrystalline conventional material. Sensitivity of sensors built with nanocrystalline material in comparison with that of devices built with conventional microcrystalline material, increases from 30% to 37%. In this work, SnO₂ is synthesized using two different modified techniques based on gel-combustion and reactive oxidation and results of both syntheses are compared. Nanomaterials are characterised with X-ray diffraction (XRD), High Resolution Transmission Electron Microscopy (HRTEM) and Field Emission Electron Scanning Microscopy (FESEM) and absorption techniques (BET). An electronic system, already patented by the authors, enables to alternatively measure the sensor resistivity (which is proportional to the adsorbed gas concentration) and set a constant working temperature, thus contributing to considerably save energy.

Keywords: Resistive gas sensors, MEMS, Nanocrystalline SnO₂, Reactive oxidation synthesis, VOCs.

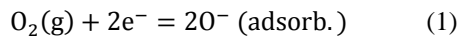
1. Introduction

Pure or doped SnO₂ semiconductor has been used for many years to build resistive type gas sensors [1-7]. When the size of the oxide particles decreases to the nanometric scale, important changes are observed in gas sensors built with nanocrystalline material directly depending on the oxide crystallite size. An increase of sensitivity (30%-37%) is observed in sensors built with nanocrystalline material in

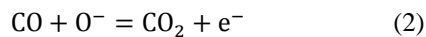
comparison with the sensitivity of sensors built with the same material but microcrystalline. The working temperature (Tw) decreases from (350-450) °C to a range (180-200) °C [8-10]. In sensors previously built by the authors, the microcrystalline semiconductor has been deposited on one face of an AlSiMg substrate, building on the opposite face, a heating circuit to reach the high Tw. In this work, the nanosemiconductor is deposited as a MEMS type microheater, which functioning is based on an electronic circuit that

implements a switching logic. This circuit enables to measure the variation of film surface resistivity which is related to the analyte concentration and, conveniently heated, it enables to save energy.

The gas detection process is affected by several factors, among them: the microstructure of the gas adsorbing surface. The metallic oxide previously reacts with the air oxygen forming adsorbates on oxide surface (O^- , O^{2-} , O_2^-) [11-13] of which the most active is O^- . The adsorbates play an important role in the sensing process, covering the semiconductor oxide surface and grain boundaries and reacting at a working temperature: $T_w \sim (350-450)^\circ\text{C}$ if the sensor is built with the microcrystalline semiconducting oxide (SCO). In case of n-type metallic oxides, the adsorbates formation generates a charge space region, resulting in an electron depleted surface layer, due to the electrons transference towards the adsorbates according to:



The charge space depth is a function of the surface covering with the oxygen adsorbates and of the intrinsic electron concentration in the bulk. The n-type SCO resistance is consequently high because a potential barrier is formed by the electronic conduction in each grain boundary [11]. If the sensor is exposed to a reducing gas (i.e. CO) at T_w , the gas reacts with the oxygen adsorbate according to:



The oxygen adsorbates are consumed in subsequent reactions so as to reach a lower steady state, the potential barrier height decreases and the resistance falls being the resistance variation, the sensor measurement parameter. A simple schematic model of the grain boundary effects on the surface resistivity was proposed by Yamazoe et al. [11] in which it was accepted that the sensor sensitivity increases as the grain size decreases. The sensor sensitivity (S) is defined as:

$S = R_{\text{air}} / R_{\text{air+gas}}$, where: R_{air} is the resistance in air and $R_{\text{air+gas}}$ is the resistance in a gas mixture containing a reducing gas component. The oxygen adsorbates resistivity is a function of the reducing gas type and of sensor temperature.

The microstructure and morphology of Al-doped or In-doped nanocrystalline SnO_2 (with different crystallites size) has been studied, contributing the doping to increase the sensor selectivity to different gases [14]. Nanomaterials were prepared by sol-gel [15] and by reactive oxidation with H_2O_2 [16] and the found similar results were analysed [7, 14]. Characterisation has been performed with X-ray diffraction (XRD), absorption techniques by Brunauer-Emmer-Teller (BET) isotherms and High Resolution Transmission Electron Microscopy (HRTEM). Authors' previous works generated interesting results since the sensors sensitivity increased from 30% to 37% and the T_w considerably

decreased from $350^\circ\text{C} - 450^\circ\text{C}$ to $250^\circ\text{C} - 350^\circ\text{C}$ for Al-doped nanocrystalline SnO_2 and, similarly, to $180^\circ\text{C} - 220^\circ\text{C}$ for In-doped nano- SnO_2 , corresponding the minor T_w to pure nano- SnO_2 [8-10]. The detection process is also affected by other factors, like the oxide microstructure, among them.

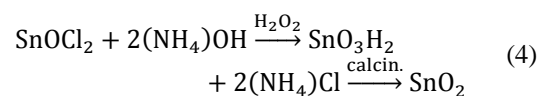
2. Experimental Procedure and Results

2.1. Pure SnO_2 Synthesis

Pure SnO_2 nanopowders were synthesized by two techniques (gel-combustion and reactive oxidation) and results were compared [7]: modified gel-combustion with nitrate-citrate [15] and reactive oxidation with H_2O_2 [16].

The gel-combustion is a fuel rich synthesis [15] beginning with a precursor preparation (an aqueous solution with metallic p/a Sn), 70% - HNO_3 - CH_3COOH and 25% - NH_4OH . Citric acid is the organic fuel with a rate: $[\text{Sn}/\text{fuel}] = 1:6$; pH is controlled with $(\text{NH}_4)\text{OH}$ (approaching to neutrality and maintaining the solution homogeneity). The solution is thermally evaporated till reaching a gel. Upon keeping the heating, the gel is transformed into a dark foam which ignites. The intensive combustion in the final stage is due to a highly isothermic redox reaction which is produced between the oxidant nitrate ions and the organic fuel at $\sim 80^\circ\text{C}$ and ignition is produced at $\sim 200^\circ\text{C} - 300^\circ\text{C}$. Combustion usually generates an ignition which is independent of the provided atmospheric oxygen since the foam bubbles are filled either with NH_4NO_3 vapor or with NO_x ($1 < x < 2$) restricting the oxygen access to the site bottom where the reaction is produced. The combustion duration is short, usually half a minute. The gas liberation produces a fast disintegration of the precursor gel at high temperature causing decomposition. If the oxide contains carbonaceous residues by fuel excess, they must be removed by calcination and nanometric crystallites are produced (9 nm - 15 nm). Parameters to be controlled are: type of organic fuel, combustion temperature and process duration. After the synthesis, the crystallites size and homogeneity, the morphology and the impurities retention during the synthesis process have been carefully evaluated.

In the second method, the SnCl_2 reacts with H_2O_2 and the product is afterwards treated with $(\text{NH}_4)\text{OH}$ in H_2O_2 medium. The stannic acid is produced treating the SnO_2 powder by calcination:



The oxidative reaction with H_2O_2 disintegrates the product particles generating small crystallites with sizes in a range: 2 nm - 9 nm.

2.2. Synthesis of Doped SnO₂

The gas sensor to detect hydrogen was built with pure nanocrystalline SnO₂ [9]. The device to sense CO (g) ppm was built with Al-doped nanocrystalline SnO₂ [8] and that to sense VOCs was built with In-doped nanocrystalline SnO₂ [10]. The method to prepare the two first materials: pure and Al-doped SnO₂ was gel-combustion using CH₃COOH as fuel, being the crystallite size: 2 nm - 4 nm. In the case of In-doped nanocrystalline SnO₂ [10], the synthesis method consisted in precipitating together SnCl₂·2H₂O and InCl₃, in NH₄NO₃ medium to produce the stannic oxyhydroxide which is intensively oxidized with 30-250 vol. H₂O₂, thus producing stannic acid in nanocrystalline powder. This solution is precipitated with (NH₄)OH to get a homogeneous compound of stannic acid and indium hydroxide, being the resulting crystallite size ~2 nm - 4 nm.

2.3. Nanomaterials Characterisation

The X-ray diffraction enabled to identify the material, to evaluate the crystalline structure and to measure the crystallites size (applying the Scherrer equation); the adsorption BET (Brunauer-Emmer-Teller isotherms) measurements have been used to determine the specific area and the HRTEM, Fig. 1 is a HRTEM micrograph of pure nano-SnO₂ lattice, oriented [101] and the e-diffraction pattern.

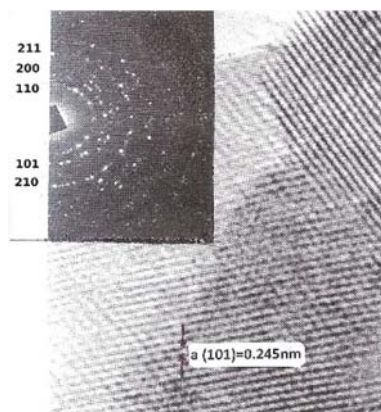


Fig. 1. HRTEM micrograph of pure nano-SnO₂ lattice (calcinated at: 700 °C) oriented along [101] with the electron diffraction pattern. The atomic ordering is clearly resolved.

2.4. Heating Hot-plate and Related Electronics

As it was pointed out before, if the working temperature (T_w) is in the range: 300 °C-400 °C, the heater needs a high electric power, which is a problem in the application field. Reliable control of the operating temperature prolongs the life of the assembly sensor-capsule.

The micro hot-plate, used to perform measurement and heating [17], involves a minimal power consumption and exhibits an architecture enabling the manufacture on a MEMS type support. Fig. 2 shows the micro hotplate architecture, which support is a silicon <100> wafer coated with a non-stoichiometric Si_xN_y film. The coating exhibits a low residual stress (< 200 MPa) and 1 micron thick grown by LPCVD enabling the system thermal isolation and the structure resistance and mechanical stability. Square windows: 1.5 mm x 1.5 mm, are usually got.

The micro hotplate, connected to a TO-8 capsule, is shown in Fig. 3. Hot-plates were built with platinum including a TiO₂ adherent interface. The hot-plate consists of a micromachined silicon support and windows are got by wet etching technique with KOH. The Si_xN_y substrate coating stops the etching of micromachining process and acts as thermal isolation between the hot zone and the substrate body which is joined to the capsule. To reach an optimal thermal isolation it is of the highest importance to get reliable welding between the capsule contacts and the sensor (on the wafer). A platinum heater with double-meander structure (heating – pick-up contacts) is integrated to the Si_xN_y film.

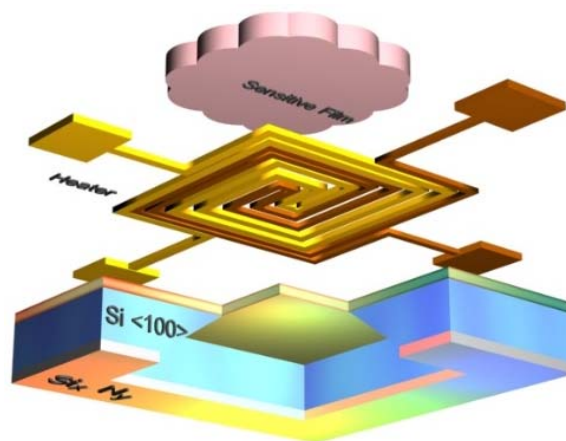


Fig. 2. Architecture of the MEMS hot-plate.

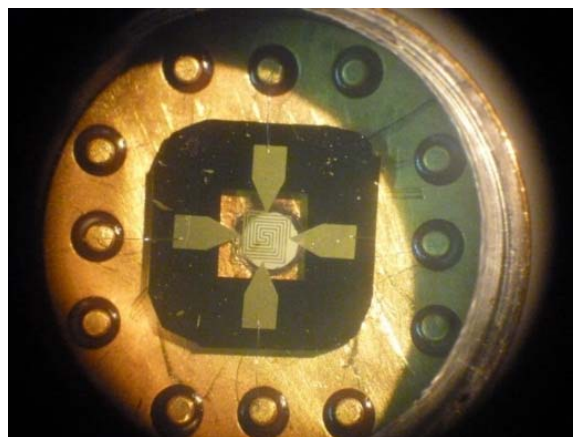


Fig. 3. Microheater.

The double meander structure is centered in the window of the Si_xN_y membrane released from the substrate, by micromachining the $\langle 100 \rangle$ Si. This arrangement is used to improve the device thermal efficiency with regards to minimal power consumption [18-20].

The double meander structure is used to heat the sensitive film and to extract the signal. This new structure not only achieves a performance similar to conventional sensors heaters deposited on alumina substrates, but also reduces 10-15 times the device power consumption [20]. Otherwise, the thermal and electrical contact is directly produced with the nanostructured sensitive film, being the film printed with a thick film technology through handicraft techniques, similar to those of screen printing [20]. To explain the use of the Pt double meander as heater and as contact to pick-up the signal, the ad-hoc electronics as described in [17, 19] is considered, Fig. 4.

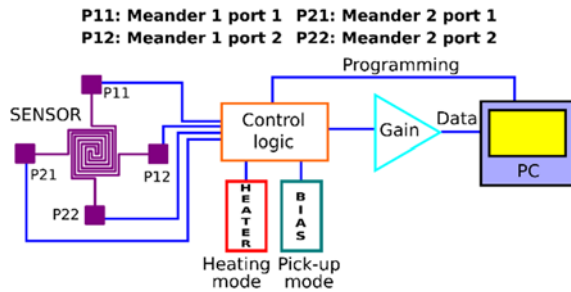


Fig. 4. Electronic control system diagram.

The portable electronic system consists of a microcontroller and discrete electronics components [17]. The description of the elements of the diagram shown in Fig. 4 is detailed:

- PC (data acquisition and calculation): it enables the storage of resistivity values of the sensitive film in function of time to transform these values into the concentration of the gas to be measured. The signal is filtered to reduce measurement noise. The processed data are then transmitted to an external device for later use.
- Gain: amplifies and conditions the signal picked up by the sensitive film, which is then acquired and processed by the PC block.
- Control logic: switches the heater-contact between both two functions (sensitive film heater or contacts).
- Heating: includes the electronic components that apply the necessary power level (temperature) which is convenient to reach the optimal response of the sensitive semiconductor film (T_w).
- Bias: electronic circuit that generates the SnO_2 film bias.
- Sensor (heating-contacts): sensitive film printed on the double meander (double purpose).

The logic obeying the device functioning is as follows: the control logic switches the connection of

the double meander electrodes to use them as heaters or contacts capable of picking up the signal according to a predetermined timing stored in the system memory. The working principle is based on the application of a simple pulsed type strategy [19]: for a time lapse (ms), the sensor electrodes are excited through the heating block (which supplies the necessary power for the correct operation of the SnO_2 sensing film). In this heating stage, the two resistors which form the double meander are connected in series. The Si_xN_y membrane exhibits a thermal isolation enabling, once removed the heating power, to maintain the sensor temperature during a short lapse (ms). After heating, the control logic switches the double meander contacts to the pick-up mode enabling the bias block to excite the terminals with convenient bias levels on the sensitive film. The double meander structure and the connection of the electrodes in heating and pick-up modes are shown in Figs. 5a, 5b, 5c and 5d.

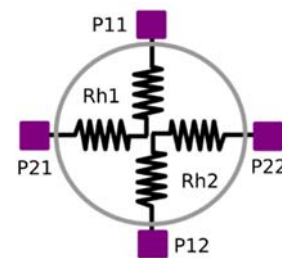


Fig. 5a. Double meander resistors diagram.

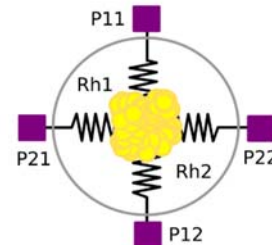


Fig. 5b. Idem Fig. 5a with the sensitive film (yellow).

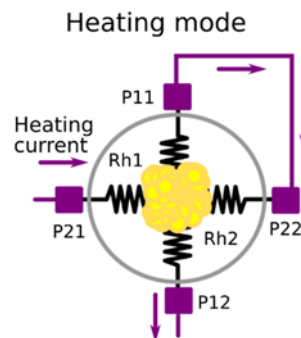


Fig. 5c. Diagram of the double meander resistors in heating mode: Rh1 and Rh2 resistors are connected in series.

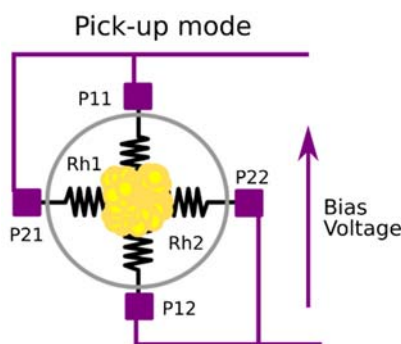


Fig. 5d. Diagram of the double meander resistors in pick-up mode: the electrodes of each resistor (Rh1 and Rh2) are short circuited.

The acquired data are presented, stored and used to calculate the analyte concentration periodically repeating this process according to the required application. A time plot corresponding to the described signals is shown in Fig. 6. It is qualitatively observed the difference between the heating times (heating mode) and the measurement of the sensitive film (pick-up mode). The electrodes, configured as heaters, excite the sensitive film only a few milliseconds. The sensitive film can reach a temperature of about 350 °C to heat and clean the system to avoid gases that could interfere the measurements. Before measuring the sensitive film resistivity, a preheating is performed at ~250 °C to allow evaporation of interfering molecules.

Once removed the heating power (heating mode), the film resistivity is measured with the signal conditioning circuit in pick-up mode, for a short time (less than one millisecond) after the heating effect is completed. Fig. 7 shows the described timing.



Fig. 6. Double meander resistors diagram.

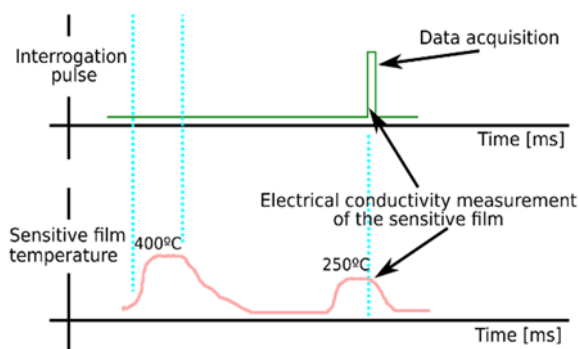


Fig. 7. Double meander resistors diagram.

Fig. 8 is an infrared micrograph showing the different temperature stages of the heater from room temperature to working temperature.

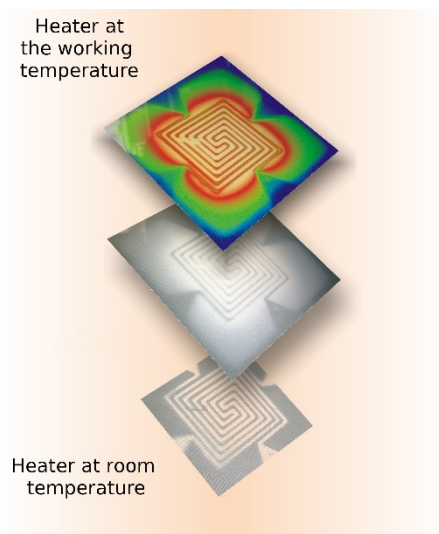


Fig. 8. Infrared images showing the heater different temperature stages a) heater image at T_w and b) heater image at room temperature.

The film temperature does not change fast due to the inertial effect of the system. After the heating time, a temperature value close to the preheating is maintained [20]. During this short time, the sensitive film can be biased to measure its resistivity, which is proportional to the adsorbed gas concentration.

3. Conclusions

The nanocrystalline pure, Al-doped or In-doped SnO_2 was synthesized with different crystallite size (ϕ : crystallite diameter) to build resistive type gas sensors to detect: H_2 , CO and VOCs. Synthesis was performed by gel-combustion method [$\phi = 9$ nm-15 nm] and by reactive oxidation with H_2O_2 [$\phi = 2$ nm - 9 nm]. Several techniques: DRX, BET isotherms adsorption method and HRTEM were used to characterise the microstructural and morphologic properties of the pure and doped nanocrystalline SnO_2 . The calcination temperature produced an increase of grain size contributing to decrease the specific absorption area. The analysis of DRX spectra of doped SnO_2 with different crystallite size, always enabled to identify the structure of the crystallographic phase of tetragonal rutile as found in pure SnO_2 . HRTEM micrographs show nanoparticles (with very small ϕ), with rounded borders and high defects density, which are homogeneously distributed. Calcination at higher temperature caused larger size crystallites exhibiting a faceted form and with considerably minor defects density. Sensors to detect H_2 , built with pure nano- SnO_2 , showed a ~35 % higher sensitivity in

comparison with that of reference sensors. The working temperature (T_w) decreased to $\sim 180^\circ\text{C}$ - 200°C according to the smallest crystallite size. An electronic switching system was developed and applied to sensors, alternatively measuring the sensor resistivity proportional to the adsorbed gas concentration and setting the working temperature. Details of the MEMS microheater were carefully described.

Acknowledgements

Thanks are given to Eng. Federico Checozzi (UTN-FRH) for his help in the characterisation of micro-heaters and to Techn. Daniel E. Gasulla for his valuable work to build the prototypes and special devices. The authors thank to Damian Fernández for his thermography assistance at the Images Control Laboratory (CITEDEF).

References

- [1]. L. B. Fraigi, D. G. Lamas, N. E. Walsöe de Reca, Quím. Analít. (España), 18, Suppl. 1, 1999, pp. 71-75.
- [2]. L. B. Fraigi, D. G. Lamas, N. E. Walsöe de Reca, Solid State Microsensors for Environmental Monitoring, CYTED, Proy. IX.2, Ed. Control S. R. L., Bs. As., 1999, pp. 57-72.
- [3]. L. B. Fraigi, PhD Thesis (Engin.) FI-UBA, 2006.
- [4]. N. E. Walsöe de Reca, Anales Academia Nacional de Ciencias Exactas, Físicas y Naturales, ANCEFYN, 59, 2007, pp. 59-93.
- [5]. L. B. Fraigi, D. G. Lamas, N. E. Walsöe de Reca, Novel method to prepare nanocrystalline SnO₂ powders by a gel-combustion process, Nanostruct. Mater., 11, 1999, p. 311-318.
- [6]. L. B. Fraigi, D. G. Lamas, N. E. Walsöe de Reca, Comparison between two combustion routes for the synthesis of nanocrystalline SnO₂ powders, Mater. Lett., 47, 2001, p. 262-262.
- [7]. M. F. Bianchetti, I. Bracko, S. D. Skapin, N. E. Walsöe de Reca, Nanocrystalline Tin Oxide to be Applied in a Gas Sensor, Sensors & Transd. J. 137, 2, 2012, pp. 155-164.
- [8]. M. Cabezas, D. G. Lamas, E. Cabanillas, N. E. Walsöe de Reca, Method to build a Gas Sensor with nanostructured Al₂O₃-doped SnO₂ to sense CO (gas), R. A. Patent P20130101356, Dec. 2013, in procedure.
- [9]. M. Bianchetti, N. E. Walsöe de Reca, Gas sensor built with pure nanocrystalline SnO₂ to sense H₂, Patente R. A. P 20130100781, in procedure.
- [10]. M. Bianchetti, M. E. Fernández, R. Juárez, N. E. Walsöe de Reca, Gas sensor of gas built with nanocrystalline In₂O₃-doped SnO₂ to sense VOCs, Patent R. A. P2013101426, in procedure.
- [11]. N. Yamazoe, J. Fuchigami, M. Kishikawa, T. Seiyama, Interactions of tin oxide surface with O₂, H₂O AND H₂, Surf. Sci., 86, 1979, pp. 335-344.
- [12]. Yu. A. Dobrovolskii, G. V. Kalinnikov, Oxygen chemisorption by SnO₂-based oxide electrodes in solid electrolytes, Élektrokimiya, 28, 10, 1992, pp. 1567-1575.
- [13]. Y. Shimidzu, M. Egashira, Basic concepts and challenges of semiconductor gas sensors, MRS Bulletin, 26, 4, 1999, p. 18-24.
- [14]. N. E. Walsöe de Reca, M. F. Bianchetti, C. L. Arrieta, Sensors and Actuators, B (Chemical), 2014, Vol. 190.
- [15]. G. E. Lascalea, Materials Science and Technology, PhD Thesis, Inst. Jorge Sabato, CNEA-UNSAM, 2008.
- [16]. M. F. Bianchetti, N. E. Walsöe de Reca., Novel method to synthesize nanostructured metallic oxides, R. A. Patent P20130100781, in procedure.
- [17]. L. T. Alaniz, C. L. Arrieta, M. F. Bianchetti, C. A. Gillari, J. F. Giménez, H. A. Lacomí, D. F. Valerio and N. E. Walsöe de Reca, Gas sensor provided with a heating device and the method to sense, R. A. Patent P-070105987, granted on December 28th, 2013.
- [18]. G. Cardinali, L. Dori, M. Fiorini, I. Sayago, G. Faglia, C. Perego, G. Sverbeglieri, V. Liberati, F. Maloberti, D. Tonietto, Annual Report, Consiglio delle Recherche, LAMEL, 1998, pp. 71-74.
- [19]. J. F. Giménez J. F., C. A. Gillari, C. A. Valerio, D. F. Gasulla, L. T. Alaniz, H. A. Lacomí, C. L. Arrieta., Pampa III Electronic Nose, The Journal of the Argentine Chemical Society, Vol. 93, 1/3, 2005, pp. 115-122.
- [20]. D. Briand, A. Krauss, B. van der Schoot, U. Weimar, N. Barsan, W. Göpel, N. F. Rooij, Design and fabrication of high-temperature micro-hotplates for drop-coated gas sensors, Sensors & Actuators B., 68, 2000, pp. 223-233.



Simple Colorimetric DNA Biosensor Based on Gold Nanoparticles for Pork Adulteration Detection in Processed Meats

¹ Bambang KUSWANDI, ¹ Agus A GANI, ¹ Nia KRISTININGRUM
and ² Musa AHMAD

¹ Fakultas Farmasi, Universitas Jember, Jl. Kalimantan 37 Jember, 68121, Indonesia

² Faculty of Science & Technology, USIM Bandar Baru Nilai, Malaysia

¹ Tel.: +62-331-324736, fax: +62-331-324736

¹ E-mail: b_kuswandi.farmasi@unej.ac.id

Received: 10 December 2016 /Accepted: 30 December 2016 /Published: 31 January 2017

Abstract: In order to develop simple sensing system for pork adulteration in processed meats, the DNA biosensor based on 20 nm gold nanoparticles (AuNPs) with aggregation property has been developed as a simple colorimetric detection of target DNA. Adsorption of single-stranded (ss) DNA on AuNPs protects the particles against salt-induced aggregation. However, mixing and annealing of a 27-nucleotide (nt) ssDNA probe on AuNPs with denatured DNA of different processed meats differentiated between perfectly matched and mismatch hybridization at a critical annealing temperature (55 °C). The AuNPs change color from red to purple, in 10 mM phosphate buffer saline (PBS). At a hybridizing temperature (55 °C), non-target mismatched DNA provided hybridization products allowing probe to be free and adsorbed to AuNPs. This prevented AuNPs from salt-induced aggregation as the color still red. In matched DNA, hybridization would occurred, allowing probe to be occupied. This facilitated AuNPs from salt-induced aggregation and induced colorimetric change of particles from red to purple. These signals could be observed easily with naked eye. This label-free DNA nanobiosensor should find applications in food analysis and other DNA based screening.

Keywords: Colorimetric sensors, DNA biosensor, Gold nanoparticles, Pork adulteration, Processed meats.

1. Introduction

Detection of specific sequences of DNA has important applications in medical and diagnosis [1, 2], food analysis [3, 4] and forensic study [5]. Usually, the detection of DNA specific sequence via hybridization has been perform after the DNA target has been amplified by polymerase chain reaction (PCR). PCR is widely used to selectively amplify a segment of longer DNA from as little as a single copy to easily detectable quantities. The application of PCR addresses sensitivity issues and requires sample

purification steps [3]. For these main features, PCR amplification has become a mandatory step for the analysis of genomic DNA. Although, there are many sensing approaches available without PCR amplification, such as surface plasmon resonance (SPR) [6], fluorescent microarrays [7], semiconductor [8], nanoparticle or polymer based biosensors [9, 10]. Besides PCR, most assays identify DNA specific sequence via hybridization of an immobilized DNA probe toward a target DNA after the target has been linked with a label or tag [11]. DNA detection schemes that avoid labeling or tagging such as surface plasmon

resonance [12], ellipsometry [13], and lately, an assay using functionalized gold nanoparticles [14, 15] have been developed. Generally, these approaches use surface chemistry functionalization and usually require sophisticated instrumentation system for detection of hybridization even. On the other hand as reported in the literature, there is a difference in electrostatic properties of single- and double-stranded DNA (ssDNA and dsDNA) that can be used to design a colorimetric sensor to detect DNA hybridization [16, 17, 18]. Here, the color change derives from colloidal gold particle aggregation, with no modification of the gold or the ssDNA probe or target DNA is required. Furthermore, hybridization is completely separate from detection so that it can be done under optimal conditions and makes the method more efficient and effective.

The color change derives from colloidal gold particle aggregation occurs due to ssDNA and dsDNA have different electrostatic properties, which resulted the distinction on their surface plasmon resonance (SPR) characters of aggregated dsDNA–AuNPs and disperse colloidal ssDNA–AuNPs, which are interesting as they can be monitored by colorimetry and also observed easily by naked eye [11–19]. The essential difference arises as ssDNA can uncoil to expose its bases sufficiently, whereas dsDNA has a stable double-helix structure that presents the negatively charged phosphate backbone [20]. Typically, in solution AuNPs are stabilized by adsorbed negative ions (e.g., citrate ions) whose repulsion prevents the strong van der Waals attraction between AuNPs from aggregation [21]. In dsDNA, repulsion between its charged phosphate backbone and the adsorbed citrate ions dominates the electrostatic interaction between AuNPs and dsDNA so that dsDNA will not adsorb. While in ssDNA, is sufficiently flexible to uncoil its bases partially, they can be exposed to the AuNPs. Under these conditions, the negative charge on the backbone is sufficiently distant so that attractive van der Waals forces between the bases and the AuNPs are sufficient to make ssDNA to stick to the gold, thus make them still as colloidal nanoparticles. However, this mechanism is not applied with dsDNA, due to the duplex structure does not permit the uncoiling needed to expose the bases, and thus make them in aggregated nanoparticles [11].

In this article, the selective adsorption of ssDNA on AuNPs was employed as a basic mechanism for colorimetric detection of specific DNA sequence in processed meat, i.e. meatballs. This is due to the fact that adsorption of ssDNA stabilizes AuNPs against aggregation at high concentrations of salt [11–13]. Since, the color of AuNPs is determined principally by SPR, and affected by aggregation of AuNPs drastically [22], therefore, we used this mechanism to design a simple colorimetric sensor for detection of DNA hybridization. The sensor can be used for sequence-specific detection of unlabelled DNA by using unmodified commercially available 20 nm AuNPs [23, 24]. The DNA nanobiosensor was applied to detect pork DNA in processed meat (i.e. pork in

beef and chicken meatballs) as a pork adulteration issue in meatballs increases currently. The sensor is easy to implement for visual detection and successfully applied to detect hybridization between ssDNA probe and its complementary. The assay also directly detected pork DNA in genomic DNA mixtures extracted from processed meats, avoiding PCR amplification, electrophoresis and sample purification chemistry. Thus, it does not need any instrument or surface modification chemistry of nanoparticles and directly detects hybridization even in non-amplified mixed genomic DNA.

2. Materials and Methods

2.1. Chemicals

Design of porcine-specific oligoprobe was chosen using a 27-nt AluI-cut fragment (428–454 bp) of porcine (*Sus scrofa*) cytb gene (GenBank accession no. Gu135837.1 in NCBI data base) and used as a porcine-specific marker. This fragment demonstrated a high degree of polymorphism between the species and similarities within the species by NCBI-BLAST analysis against non-redundant nucleotide collections and also by ClustalW alignment analysis. The probe and synthetic targets (complementary, non-complementary) were supplied by the 1st Base, Malaysia. The probe and oligosequences are shown in Table 1. All other chemicals used were of analytical grade or of the highest purity available and were purchased from Sigma-Aldrich (USA). All glassware was cleaned thoroughly with freshly prepared aqua regia (3:1 (v/v) HCl/HNO₃) and rinsed thoroughly with Milli-Q water prior to use. Milli-Q water was used to prepare all the solutions in this study.

Table 1. Sequences of oligonucleotides used.

Name	Sequence (5'→ 3')
Probe	CTG ATA GTA GAT TTG TGA CCG TAG
Complementary target	CTA CGG TCA CAA ATC TAC TAT CAG
Non-complementary target	ACG TAA CTG CTG TGG CCT GGT CGC TGA

2.2. Preparation of Meatballs and DNA Extraction

In order to detect pork adulteration in processed meat products, meatballs are used as an example. Meatballs are prepared according to Kuswandi et al. [25] both with pure and mixed emulsified meats of pork, beef, and chicken, along with the addition of starch, seasonings, and salts in certain ratios. All the meatballs are cooked in boiling water for 20 min prior to DNA extraction. DNA extraction is performed from 100 mg of cooked meatball of each formulations using

MasterPure DNA Purification Kit (Epicenter Biotechnologies, USA) as per the manufacturer instructions. The DNA concentration is determined with a biophotometer (Eppendorf, Germany) based on triplicate readings. The purity (A260/A280) of all DNA samples used in all experiments is 2.0 ± 0.05 .

2.3. DNA Nanobiosensors Preparation

A 27 nt pork specific probe (5')- CTA CGG TCA CAA ATC TAC TAT CAG -(3') was employed as porcine specific probe. A gold nanoparticles (AuNPs) 20 nm in size in water solution were purchased from Sigma-Aldrich (USA). The DNA probe-AuNPs binding was performed as follows. In brief, 30 μ L of 27-mer ssDNA of 100 nM was added to a mixture of 100 μ L of 1.8 nM colloidal AuNPs. After mixing, they were incubated in a water bath at 50 °C for 3 min to facilitate DNA probe adsorption onto AuNPs. The final products were loose red pellets and ready used as the DNA nanosensor.

In order to test that DNA probe was successfully adsorb onto AuNPs, the DNA nanosensor was tested by adding 100 μ L of 10 mM PBS was added in vial (c) (inset Fig. 1), and 50 μ L complementary target products (500 μ g/ml) were added in vial (d), where both contain 400 μ L of the DNA nanobiosensor (100 nM). Finally, 100 μ L of 10 mM PBS was added to vial (d) (inset Fig. 1). The final volume was adjusted to 1 ml with DI (deionized) water (18.2 M Ω) and the absorption spectra were measured by UV-vis spectroscopy (Ocean Optics® USB2000, Dunedin, FL, USA) along with absorption spectra of AuNP colloids in DI water (a), and in 10 mM PBS buffer (b) as shown in Fig. 1 as comparison.

2.4. Complementary and Non-complementary Target Detection

For hybridization and mismatch detection, 50 μ L complementary target products (500 μ g/ml) and 400 μ L of DNA nanobiosensor (100 nM) were added in vials (a) and (b) as given in Fig. 3. Equal volumes of non-complementary target and DNA nanobiosensor were added in vials (c) and (d) as given in Fig. 3 respectively. The mixtures were denatured at 95 °C for 3 min and then annealed at 55 °C for 2 min. Finally, 100 μ L of 10 mM PBS was added to each vial (Fig. 3). The final volume was adjusted to 1 ml with DI water and the absorption spectra were measured by UV-vis spectroscopy.

2.5. Detection of Pork in Processed Meat Sample

In order to detect pork adulteration in processed meat products, meatballs were used as a model. The meatballs were prepared by emulsifying the mixed

meatballs of pork-beef and pork-chicken, binary mixtures in 1:1 (w/w) ratios. Pure meatballs of each species (pork, beef and chicken) are formulated with pure meats under identical conditions. After 20 min of cooking in boiling water, DNA extractions are performed. Approximately 100 mg mixed and pure meatball samples from each specimen were autoclaved at 120 °C for 30 min at a pressure of 3 bar. By this treatment, all samples lost their normal textures and turned into a liquid broth. DNA extraction was performed as described previously. One hundred microliters (100 μ L) of mixed genomic DNA (200 μ g/ml) was taken in vials (a)–(c) as shown in Fig. 4. Equal amounts of pure genomic DNA (pork, beef and chicken) were taken in vials (d), (e) and (f) as shown in (Fig. 4). All vials were incubated with 250 μ L of DNA nanosensor at 95 °C for 3 min and then annealed at 55 °C for 2 min. Finally, 100 μ L of 10 mM PBS was added to each vial (Fig. 4). The final volume was made up to 1 ml with DI water and the spectra were characterized by absorption spectroscopy.

2.6. Determination of the Limit of Detection

To determine the LOD (limit of detection), pork meatball and beef meatball was mixed at concentration 1 %, 5 %, 10 %, 15 %, 20 % and 30 % (w/w) as well 100 % (pure pork). DNA extraction was performed from the mixed meatballs and 100 μ L of mixed DNA (300 μ g ml⁻¹), extracted from the above specimens, was taken in six separate vials marked. All vials were incubated with 15 μ L of (100 nM) DNA nanobiosensor (27-nucleotide shown in Table 1) at 95 °C for 3 min and then annealed at 55 °C for 2 min. Finally, 100 μ L of 10 mM PBS was added to each vial. The final volume was made up to 1 ml with DI water and the absorbance intensity was measured at 525 nm by visible absorption spectroscopy. The concentration of porcine DNA in mixed samples at concentration 1 %, 5 %, 10 %, 15 %, 20 % and 30 % (w/w) is calculated to be 0.4, 2.0, 4.0, 6.0, 8.0 and 1.2 μ g/ml respectively.

3. Results and Discussion

3.1. Characterization of DNA Nanobiosensor

The particle size (20 nm) was employed according to previously proposed methods [24, 26]. The vials in Figs. 1(a) and (c) revealed the distribution of disperse small particles in the bulk sample as shown by the red color. The aggregates (one on another) in vials were seen after addition of the salt (Figs. 1(b) and (d)) as shown by the purple color. Visible of absorption spectra of disperse colloidal (non-aggregated) and aggregated 20 nm AuNPs in DI water and 10 mM PBS are shown in Fig. 1. The aggregated particles exhibited a plasmon shift from 525 nm to 700 nm as seen in Figs. 2b and 2d while no such a change was observed in non-aggregated ones (Figs. 2a and 2c). Naturally,

this surface plasmon resonance mode, which gives colloidal gold (non-aggregated), its characteristic red color, is well understood, as it depends on particle size and shape [3, 15, 16, 27-29]. However, the aggregated colloidal particles in this report lost the absorption peak at 525 nm in PBS as they turned from red to purple.

The visible spectra of AuNPs in PBS lost its absorption peak at 525 nm, which indicating aggregation as the red color turn to purple. The procedure for determining the critical concentration of salt can be found elsewhere [27]. The hybridization between complementary targets DNA toward porcine probe DNA could not prevent salt-induced aggregation of AuNPs. This was also confirmed by the loss of the 525 nm peak (spectrum (d) in Fig. 1). However, a slightly reduced level of aggregation was observed in the visible spectrum (Fig. 1, spectrum (d)). The aggregation reduction could be due to the presence of some ssDNA that not all react with complementary target during hybridization reaction, which might interfere with the aggregation. This was also reported elsewhere [19]. The spectrum of AuNPs immobilized with porcine probe ssDNA (DNA nanobiosensor) produced a less intense peak at 525 nm, indicating some degree of aggregation upon the addition of salt. This was revealed by the higher base line in the region of 620–800 nm in the absorption spectrum (Figs. 1b and 1d).

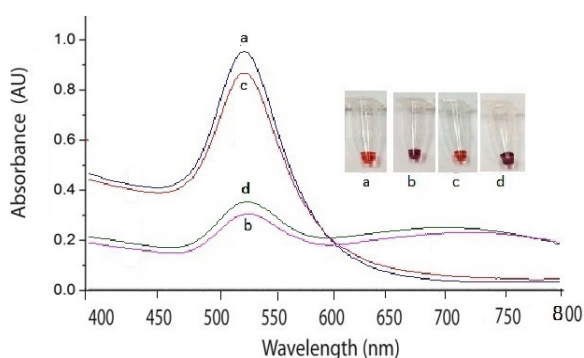


Fig. 1. Absorption spectra of disperse and aggregated AuNPs. Shown are absorption spectra of AuNP colloids in DI water (a), in 10 mM PBS buffer (b) and in 10 mM PBS buffer with porcine probe-AuNPs colloids (c), and in after reaction with complementary target DNA (d). Insets are the color photographs of AuNP colloids in DI water (a), PBS buffer (b), PBS buffer in porcine probe-AuNPs (c) and PBS buffer after hybridization between porcine probe-AuNPs with complementary target DNA (d).

3.2. Complementary and Non-complementary Target Detection

Colloidal AuNPs is bio-compatible and commercially available at reasonable prices for desirable sizes. Therefore, AuNPs used to identify species specific sequences in complementary target products before applied to detect genomic DNA, in

order to proof the mechanism of the method that it could detect complementary and non-complementary target detection as described in the Fig. 2.

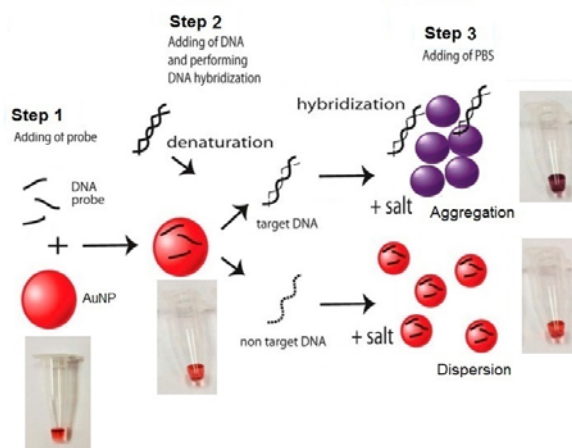


Fig. 2. Schematic of a colorimetric DNA detection based on AuNPs.

A 27-mers probe that had 100 % matches with complementary target product and mismatch with non-complementary target were used as given in Fig. 3 (see inset). The key to the successful DNA detection was the control of particle dispersion and aggregation with complementary target DNA products of interest and DNA probe. Addition of single-strand DNA probes to AuNPs as DNA nanobiosensor, as the first step allowed the adsorption of the probes on the surface of AuNPs via nitrogenous base/gold van der Waals forces [17]. Here, it was found that at a critical temperature (55 °C), porcine-specific probe (27-mer ssDNA) and its complementary target product was hybridized and could not prevent from salt-induced aggregation of AuNPs (vial (a) and (b) in the inset of Fig. 3), and it is used DNA hybridization detection. However, the porcine-specific probe was not hybridized from the non-complementary products and used as mismatch detection. Therefore, the detection of DNA hybridization and mismatch were observed after the addition of salt at a critical concentration (0.2 M NaCl), where hybridized probe and non-hybridized probes (27-mer ssDNA) interact with AuNPs to form aggregation and non-aggregation, respectively. This produces a rapid and drastic color change in the reaction mixtures, which can be detected by nude eye (vial (a) and (b) in the inset of Fig. 3) without the need of any instrumentation.

The visible spectra of AuNPs in PBS lost its absorption peak at 525 nm, which indicating aggregation as the red color turn to purple. In this case, it clearly observed that absorption at 525 nm gradually decreased, and between 620 and 800 nm increased, as the particles undergo aggregation. A slight variation in spectral shape and base line was observed between the samples, which could be explained for different dielectric properties of the solution due to different

level of nucleic acids, proteins or other impurities [28, 29]. In addition, experimental errors (e.g. pipetting error etc.) could also contribute to this variation. However, this variation was not affected to our visual detection. Furthermore, visible absorption spectroscopy strongly supported the visual observation through the spectral intensity at 525 nm and 700 nm (Fig. 3).

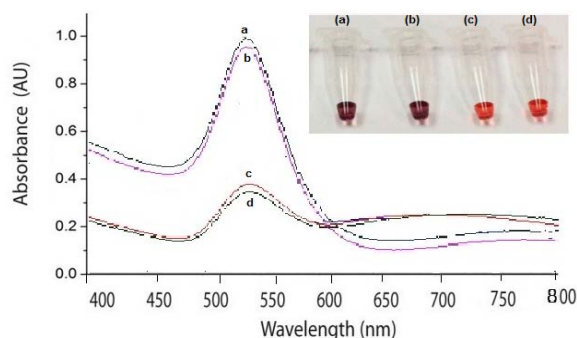


Fig. 3. Identification of complementary target as nucleotide hybridization and non-complementary target as nucleotide mismatch by porcine probe AuNPs. In the illustration vials (a) and (b) represent the color of gold colloids in complementary target product annealed with the porcine probe DNA at 55 °C, and vials (c) and (d) shows the same in non-complementary target products respectively, annealed with the same probe at the same temperatures. The sequence of the corresponding spectra is also shown alphabetically.

3.3. Detection of Pork in Processed Meat Sample

The porcine-specificity of the probes was confirmed by detecting porcine DNA in binary admixtures (1:1 w/w) of pork–beef, pork–chicken and beef–chicken DNA extracted from autoclaved mixed meatballs, and the results are given as shown in Fig. 4A and its corresponding absorption spectra are given in Fig. 4B. The purpose of autoclaving was to see whether partially degraded DNA could be detected by AuNPs, as several literature reports have demonstrated that such treatment breaks down genomic DNA into small fragments [8, 10]. In addition, a certain level of genomic DNA degradation is also obvious during physical and chemical processing of meat and processed meat products [8, 10]. Therefore, the procedure for sample preparation in heat-treated and pressurized processed meat mixture was appropriate to detect specific DNA sequences. Incubation of the nano-biosensor (27-mer ssDNA probe-AuNPs) with pure and mixed genomic DNA, clearly demonstrated that only the porcine DNA-containing vials (Fig. 4A (a)–(c)) changed colour from red to purple, reflecting hybridization of the probe to the porcine genomic DNA at 55 °C. No detectable change in color was observed in beef–chicken meatball mixture (Fig. 4A (d)) or pure genomic DNA of beef and chicken meatball (Fig. 4A (e) and (f)) indicating that the probe did not hybridize to mismatch containing genomic DNA under similar

conditions. In addition, visible absorption spectroscopy (Fig. 4B) strongly supported the visually results, suggesting that the color change was real.

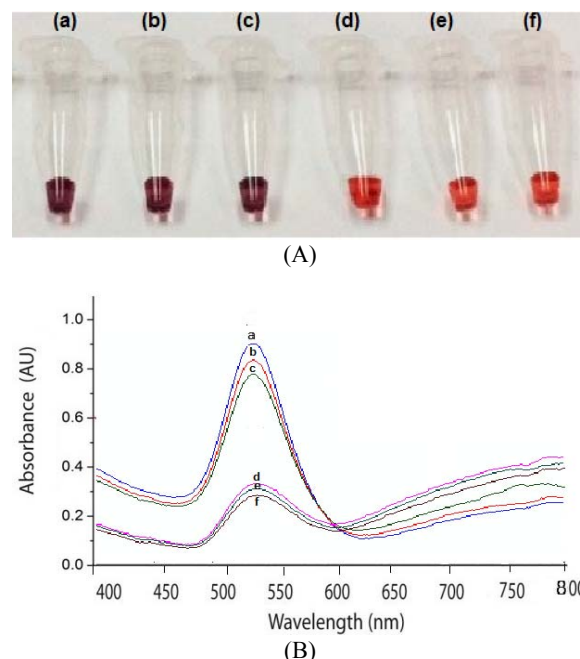


Fig. 4. Detection of porcine DNA in mixed meatballs (A). Vials ((a)–(f)) represent color of AuNPs in genomic DNA extracted from meatballs prepared with pure pork (a), 1 : 1 (w/w) mixtures of pork–beef (b), pork–chicken (c), chicken–beef (d), pure beef (e), and pure chicken (f). The corresponding absorption spectra are labeled alphabetically (B). All vials are incubated at 95 °C for 3 min and annealed at 55 °C for 2 min with 27 mer ssDNA-AuNPs before adding the 10 mM PBS.

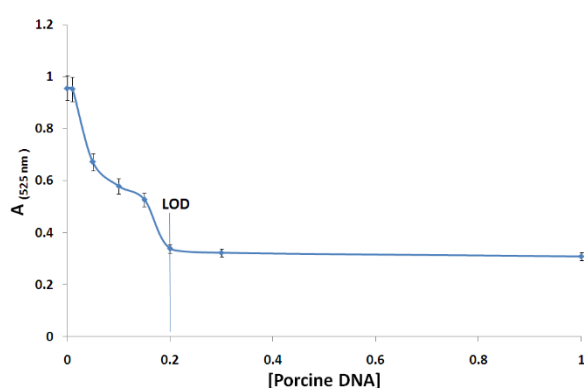
In order to support the experimental findings, the comparison between the nucleotide sequence of cytb genes of these species (pork, beef and chicken) could be aligned with the probe by ClustalW alignment program. The number of mismatches and mismatched nucleotides of each species is shown in Table 2. Only the *Sus scrofa* (pork) species showed 100% matching, and other species (beef and chicken) showed 6 nucleotide mismatching (shown in red). It is reflecting the specificity of the designed probe used in this work.

3.4. Determination of LOD

The visible absorption intensity of 27 mer ssDNA-AuNPs in various percentages of pork–beef binary admixtures is shown in Fig. 5. It was very clear from the visually observed results, as well as the intensity of the absorbance data, that 1 % pork-containing vial still retained the absorbance intensity of original color of colloidal AuNPs. However, 5 % and 10 % pork containing vial reduced at 30–40 % color of AuNPs, reflecting partial aggregation. On the other hand, 20 % and 30 % pork containing vials changed color from red to purple demonstrating aggregation.

Table 2. The comparison between the nucleotide sequence of probe used toward the nucleotide sequence cytb genes of these species (pork, beef and chicken).

Species	Sequences	Mismatch	Genbank	Meat
<i>S. Scrofa</i>	CTA CGG TCA CAA ATC TAC TAT CAG	0	GU 135837.3	Pork
Pork	CTA CGG TCA CAA ATC TAC TAT CAG			
<i>B. taurus</i>	CAA CAG TCA CAA ACC TCT TAT CAG	6	EU 807948.1	Beef
<i>G. gallus</i>	CCA CCG TAA TCA CAA ACC TAT TCT CAG	6	EU 839454.1	Chicken

**Fig. 5.** Determination of LOD for pork in the beef meatballs at 525 nm, where the LOD is shown to be 20 % (6 µg/ml) of porcine DNA in mixed meatball preparation.

Absorption intensity reflected the surface plasmon features of 20 nm diameter of non -aggregated particles and reduced of the intensity, when aggregated particles formed at 525 nm. Concentration of porcine DNA in 20 % pork-containing vial was 6 µg/ml. Thus, the LOD was determined at 6 µg/ml porcine DNA for pork meatball in mixed samples. In this LOD, since the intensity of observed absorbance decrease was less than the 30 % pork-containing vial, meaning that not all the particles change color. These might be due to the fact that the unreacted ssDNA probe-bound particles tolerated the salinity stress.

3.5. Effectiveness and Limitation

The spectra of the results were measured by visual absorption spectroscopy. However, the assay could not provide quantitative information, since linear correlation (*r*) of the calibration curve from their absorption spectra was low (Fig. 5). The LOD of the assay was slightly higher compared to other [24]. However, ss-AuNPs-based sequence detection can reduce both the cost and time, and can be afforded by

ordinary laboratories. UV–vis spectroscopy, which is available in most laboratories, can complement the spectra of the visually identified results of DNA nanobiosensor. In addition, the developed assay can be applied to detect specific sequences and mismatch without the need of PCR amplification if adequate sample is available. Currently, we are also developing this method as a chip based DNA nanobiosensor on the microwells for easily handle and simple measurement of genomic DNA detection. Besides using simple visual detection, in order to increase sensitivity and eliminates any color-error as well as low-cost, the measurement could be coupled with a conventional flatbed scanner as a reader for quantitative signal measurement as a novel “scanometric” chip-based detection system for genomic DNA detection.

4. Conclusions

A simple colorimetric sensor for rapid and reliable detection of specific sequences and nucleotide mismatch in non-amplified DNA employing aggregation properties of 20 nm AuNPs was developed. The DNA biosensor was label free, without surface functionalization, instrumental detection and was applied for detection pork DNA in processed meats, which really useful in food analysis and halal authentication. The DNA nanobiosensor was prepared by a simple and ease method. In addition, the procedure of measurement is very simple and relies on the color change of 20 nm AuNPs following salt addition. The visual finding is solid and can be further confirmed their spectra by an inexpensive, widely available and reliable technique, i.e. absorption visible spectroscopy. The use of absorption spectroscopy increases sensitivity and eliminates any sort of color-blindness error or ambiguity in visual detection by producing well defined spectrum of aggregated and non-aggregated colloidal AuNPs. Thus, the method was successfully identified porcine DNA, particularly in 20 % pork-containing samples without PCR amplification and just by using visual observation.

Acknowledgements

The authors thank the DitLitabMas, Higher Education, Ministry of Education and Culture, Republic of Indonesia, for supporting this work via the International Research Collaboration & Publication Program No. 244/UN25.3.1/LT/2015.

References

- [1]. S. B. Primrose, and R. M. Twyman, Principles of Genome Analysis and Genomics, 3rd Ed, Blackwell, Malden, MA, USA, 2003.
- [2]. J. Rees, Complex disease and the new clinical sciences, *Science*, Vol. 296, No. 5568, 2002, pp. 698–701.

- [3]. C. Murugaiah, Z. M. Noor, M. Mastakim, L. M. Bilung, J. Selamat, and S. Radu, Meat species identification and Halal authentication analysis using mitochondrial DNA, *Meat Science*, Vol. 83, No. 1, 2009, pp. 57–61.
- [4]. N. Z. Ballin, F. K. Vogensen, and A. H. Karlsson, Species determination - can we detect and quantify meat adulteration?, *Meat Science*, Vol. 83, No. 2, 2009, pp. 165–174.
- [5]. J. M. Butler, Forensic DNA Typing-Biology, Technology and Genetics of STR Markers, 2nd edition, Elsevier, NY, USA, 2005.
- [6]. Nelson B. P., Grimsrud T. E., Liles M. R., Goodman R. M. and Corn R. M. Surface plasmon resonance imaging measurements of DNA and RNA hybridization adsorption onto DNA microarrays, *Analytical Chemistry*, Vol. 73, No. 1, 2001, pp. 1–7.
- [7]. S. Sueda, J. L. Yuan and K. Matsumoto, A homogenous DNA hybridization system by using a new luminescence terbium chelate, *Bioconjugation Chemistry*, Vol. 13, No. 2, 2002, pp. 200–205.
- [8]. D. Garion, W. J. Parak, S. C. Williams, D. Zanchet, Michael C. M. and A. P. Alivisatos, Sorting Fluorescent Nanocrystals with DNA, *Journal of American Chemical Society*, Vol. 124, No. 24, 2002, pp. 7070–7074.
- [9]. K. Sato, K. Hosokawa and M. Maeda, Rapid aggregation of gold nanoparticles induced by non-cross-linking DNA hybridization, *Journal of American Chemical Society*, Vol. 125, No. 27, 2003, pp. 8102–8103.
- [10]. B. S. Gaylord, A. J. Heeger and G. C. Bazan, DNA hybridization detection with water-soluble conjugated polymers and chromophore-labeled single-stranded DNA, *Journal of American Chemical Society*, Vol. 125, No. 4, 2003, pp. 896–900.
- [11]. B. D. Hames and S. J. Higgins, Gene Probes 1, *IRL*, New York, USA, 1995.
- [12]. Brockman, J. M., Frutos, A. G. and Corn, R. M. Multi-step-chemical modification procedure to create DNA arrays on gold surface to study of protein DNA interaction with surface plasmon resonance imaging, *Journal of American Chemical Society*, Vol. 121, No. 1 1999, pp. 8044–8051.
- [13]. R. M. Ostroff, D. Hopkins, A. B. Haeberli, W. Baouchi and B. Polisky, Thin film biosensor for rapid visual detection of nucleic acid targets, *Clinical Chemistry*, Vol. 45, No. 9, 1999, pp. 1659–1664.
- [14]. Y. C. Cao, R. C. Jin and C. A. Mirkin, Nanoparticles with Raman spectroscopic fingerprints for DNA and RNA detection, *Science*, Vol. 297, No. 5586, 2002, pp. 1536–1540.
- [15]. S. J. Park, T. A. Taton and C. A. Mirkin, Array-based electrical detection of DNA with nanoparticle probes, *Science*, Vol. 295, No. 5559, 2002, pp. 1503–1506.
- [16]. H. Li and L. Rothberg, Colorimetric detection of DNA sequences based on electrostatic interactions with unmodified gold nanoparticles, *Proceedings of the National Academy of Sciences of the United State of America*, Vol. 101, 39, 2004, 14037–1409.
- [17]. H. Li and L. Rothberg, Colorimetric detection of DNA sequences based on electrostatic interactions with unmodified gold nanoparticles, *Proceedings of the National Academy of Sciences of the United State of America*, Vol. 101, No. 39, 2004, pp. 14036–14039.
- [18]. H. Li and L. Rothberg Label-free colorimetric detection of specific sequences in genomic DNA amplified by the polymerase chain reaction, *Journal America Chemical Society*, Vol. 126, No. 35, 2004, pp. 10958–10961.
- [19]. M. E. Ali, U. Hashim, S. Mustafa et al., Nanoparticle sensor for label free detection of swine DNA in mixed biological samples, *Nanotechnology*, Vol. 22, No. 19, 2011, Article ID 195503.
- [20]. V. A. Bloomfield, D. M. Crothers, Jr., and I. Tinoco, Nuclei Acids: Structures, Properties, and Functions, *University Science Books*, Sausalito, CA, USA, 1999.
- [21]. R. J. Hunter, Foundations of Colloid Science, *Oxford Univ. Press*, New York, USA, 2001.
- [22]. S. Link, and M. A. El-Sayed, Shape and size dependence of radiative, non-radiative and photothermal properties of gold nanocrystals, *Int. Rev. Phys. Chem.*, 19, 2000, pp. 409–453.
- [23]. F. Xia, X. Zuo, R. Yang, Y. Xiao, D. Kang, A. Vallée-Bélisle, X. Gong, J. D. Yuen, B. B. Y. Hsu, A. J. Heeger, and K. W. Plaxco, Colorimetric detection of DNA, small molecules, proteins, and ions using unmodified gold nanoparticles and conjugated polyelectrolytes, *Proceedings of the National Academy of Sciences of the United State of America*, Vol. 107, No. 24, 2010, pp. 10837–10841.
- [24]. M. E. Ali, U. Hashim, S. Mustafa, Y. B. Che Man, and Kh. N. Islam, Gold Nanoparticle Sensor for the Visual Detection of Pork Adulteration in Meatball Formulation, *Journal of Nanomaterials*, 2012, pp. 1–7.
- [25]. B. Kuswandi, K. A. Cendekiawan, N. Kristiningrum and M. Ahmad, Pork adulteration in commercial meatballs determined by chemometric analysis of NIR Spectra, *Food Measurements & Characterizations*, Vol. 9, No. 3, 2015, pp. 313–323.
- [26]. A. Muangchuen, P. Chaumpluk, A. Suriyasomboon and Sanong Ekgasit, Colorimetric detection of *Ehrlichia Canis* via nucleic acid Hybridization in gold nano-colloids, *Sensors*, Vol. 14, No. 8, 2014, pp. 14472–14487.
- [27]. G. Frens, Particle size and sol stability in metal colloids, *Colloidal Polymeric Sciences*, Vol. 250, No. 1, 1972, pp 736–741.
- [28]. N. R. Jana, L. Gearheart and C. J. Murphy, Seeding growth for size control of 5–40 nm diameter gold nanoparticles, *Langmuir*, Vol. 17, No. 22, 2001, pp. 6782–6786.
- [29]. A. A. Lazarides and G. C. Schatz, DNA-Linked Metal Nanosphere Materials: Structural Basis for the Optical Properties, *Journal Physical Chemistry B*, Vol. 104, No. 3, 2000, 460–467.



Surface Stress Effects on the Electrostatic Pull-in Instability of Nanomechanical Systems

Hamed Sadeghian

Department of Optomechatronics, Netherlands Organization for Applied Scientific Research, TNO, Stieltjesweg 1, 2628 CK, Delft, The Netherlands

Tel.: +31 (0)88 866 43 55,

E-mail: hamed.sadeghianmarnani@tno.nl

Received: 8 November 2016 /Accepted: 30 December 2016 /Published: 31 January 2017

Abstract: The electrostatic pull-in instability (EPI), within the framework of the nanoelectromechanical systems (NEMS) has been shown as a robust and versatile method for characterizing mechanical properties of nanocantilevers. This paper aims to investigate the surface effects, specifically residual surface stress and surface elasticity, on the EPI of micro and nano-scale cantilevers as well as double clamped beams. Since the cantilever has one end free, it has no residual stress, thus the strain-independent component of the surface stress or intrinsic surface stress has no influence on the EPI, as long as it has small deformation. The strain-dependent component of the surface stress or surface elasticity changes the bending stiffness of the cantilever and, consequently, induces shifts in the EPI. For double clamped beams, the effective residual surface stress comes into play and modifies the effective residual stress of the beam. The nonlinear electromechanical coupled equations, which take into account the surface effects are solved numerically. The theoretical results presented in this paper indicate that the EPI is very sensitive to the surface effects, especially when a double clamped beam is employed. The results show that the influence of surface effects on the EPI of cantilevers become more profound when the thickness is below 50 nm, while the influence on double clamped beams is significant even at sub-micron scale. The present study can provide helpful insights for the design and characterization of NEMS switches. Moreover, the results can be used to provide the proof of concepts of a new surface stress sensing method using EPI in nanomechanical sensor systems.

Keywords: Surface stress, Surface elasticity, Electrostatic pull-in instability, Cantilever, Double clamped beam.

1. Introduction

Surface stress has a great impact on a wide range of surface-related phenomena, such as surface reconstruction [1], phase transformation [2-4], epitaxial growth [5], and self-assembled domain patterns [6, 7]. Due to the very high surface-to-volume ratio in micro and nanomechanical structures such as cantilevers, double clamped beams, nanowires and nanotubes, the role of surface stress effects on the mechanical properties are very significant and thereby

have been extensively studied by several researchers using experimental measurements [6, 8-13] and theoretical investigations (through both atomistic simulations [2, 14-17] and modifications to continuum theory [16, 18-20,] as explanations for the observed size effects at ultra-small scales. One of the most commonly used experimental approach to measure the surface stress effects is bending of a micro/nanocantilever arising from the changes in the surface stress, which was first proposed by Stoney [8]. Later, this method has been shown as the most

appropriate method for work in liquid environment [21-23]. The other technique is to monitor changes in the resonance frequency of cantilevers or double clamped beams, and has been shown as the best suited for use in gaseous or vacuum environment [24]. This was first reported by Lagowski *et al.* [25], who studied the resonance frequency of GaAs cantilevers as a function of surface preparation and ambient atmosphere. They proposed a one-dimensional model in which the surface stress was replaced by a compressive axial force. Later on, Gurtin *et al.* [26] showed that this model is incorrect and when is corrected, yields a resonance frequency that is independent of surface stress. In order to explain the experimental results, carried out by Lagowski, the effects of surface elasticity or strain-dependent surface stress on the stiffness, and, consequently on the resonance frequency of cantilevers have been examined by many researchers [20, 26-30]. However, they concluded that the effect on the resonance frequency of micro/sub-micron cantilevers is negligible. As an example, Lu *et al.* [27] theoretically showed that on a clean silicon cantilever of 1 μm thickness, one finds shift in the resonance frequency of about 10 ppm. In practical purposes, the mass loading effects are the same order of magnitude or larger than the surface stress effects and, therefore, it is almost impossible to distinguish between shift in the resonance frequency due to surface effects and that of the loading mass, thus sensing the changes in surface parameters with the use of shifts in the resonance frequency is extremely difficult, if not impossible. Therefore, the lack of a sensitive, accurate and reliable sensing method for measuring the surface stress parameters exists. Since the surface effects influence the stiffness of nanomechanical structures, a sensing method, which is solely based on the changes in the stiffness can be very useful in studying the surface effects.

Recently, Sadeghian *et al.* [30] experimentally demonstrated the use of electrostatic pull-in instability (EPI), within the framework of the nanoelectromechanical systems (NEMS), for the characterization of micro/nano suspended structures such as cantilevers. If a voltage is applied between the cantilever and a fixed electrode, which is separated from the cantilever by a dielectric medium, the beam deflects toward the fixed electrode. Once the voltage exceeds a critical value, an increase in the electrostatic force becomes greater than the mechanical restoring force, resulting in an instable behavior (collapsing of the beam to the fixed electrode) known as the electrostatic pull-in instability phenomenon. The uniqueness of the pull-in method lies in its well-known sharp instability and the possibility of applying a force distributed along the length of the beam. The measurement is independent of mass-loading effects and the method-induced error is the lowest among all characterizing methods in NEMS [30]. More recently, the application of EPI on sensing adsorbate stiffness in nanomechanical resonators has been presented [31, 32]. Because the method is very sensitive to the

changes in the elastic behavior, while being independent of mass loading effects, it can be used for studying the surface effects.

The EPI phenomenon is also very important in Microelectromechanical systems based on the electrostatic actuation such as microwave variable capacitors [33], MEMS switches [34, 35], Digital micromirrors [36, 37] and microvalves for fluidics applications [38], where the size of the system is in the range of hundreds of micrometer. At this scale the surface effects can be reasonably neglected. However, recent experimental demonstrations reported the development of NEMS switches with thicknesses and gaps smaller than 50 nm [39, 40]. They offer very low pull-in voltages and also simultaneously offer very short switching times in the sub-microsecond range. Like MEMS switches, in NEMS switches determination of the EPI is critical in the design process. Since the characteristic sizes of these devices shrink to nanometers, thus exhibiting inherently large surface to volume ratio, surface effects may play a crucial role in their behavior and specifically on their EPI phenomena.

Up until now, extensive studies have been carried out on the investigation of the EPI, but the investigation of the surface effects on the EPI is rare. Using the generalized Young-Laplace equation and implementing it in Euler-Bernoulli beam model, Bryan Ma *et al.* [41] investigated the surface effects on a cantilever that is electrostatically actuated. Fu *et al.* studied the size effects on the electrostatic pull-in instability of nanobeams at the presence of surface energies. In this paper, the surface effects on the EPI of both cantilevers and double clamped beams are investigated. The effects of various geometrical and physical parameters such as thickness, length and residual stress at the presence of the surface effects are investigated. Due to the nonlinearity of the elastic-electrostatic interaction, exact analytical solutions are generally not available. For this, the generalized differential quadrature (GDQ) algorithm is employed to solve the nonlinear differential equation [42]. The results demonstrates the application of EPI on the study of surface effects. In the first part of the paper, the electromechanical coupled models of the cantilever and the double clamped beam subjected to an applied voltage are presented, in which, the effects of surface stress and surface elasticity are taken into account. The second part of the paper, is the results and discussion.

2. Surface Elastic Properties: an Overview

Atoms at or near the surfaces experience different environment and lack some of the atomic neighbors present in the bulk state. Consequently, the energy of these atoms are different from that of the atoms in the bulk. This excess energy associated with the surface atoms is called surface energy [43]. The Lagrangian description of the surface energy is given by [44]:

$$\gamma = \frac{1}{A_0} \sum_{n=1}^{\infty} (U^{(n)} - U^{(0)}), \quad (1)$$

where $U^{(n)}$ is the total energy of the atom n under the area A_0 and $U^{(0)}$ is the total energy of an atom in a perfect lattice far away from the free surface. In contrast to the surface energy, surface stress is defined as the forces which oppose an elastic deformation of the surface and changes the interatomic distance at a constant number of atoms [45, 46]. The surface stress tensor can be determined from the change in the surface energy due the deformation of the area, thus, the change in the surface energy is equal to the work done by the surface stress in deformation of the area through an infinitesimal elastic strain $d\epsilon_{\alpha\beta}$

$$d(\gamma A_0) = A_0 \sigma_{\alpha\beta}^s d\epsilon_{\alpha\beta}, \quad (2)$$

where $\sigma_{\alpha\beta}^s$ is the surface stress tensor and is defined as

$$\sigma_{\alpha\beta}^s = \frac{d\gamma}{d\epsilon_{\alpha\beta}} = (\tau_0)_{\alpha\beta} + S_{\alpha\beta\lambda\kappa}, \quad (3)$$

where τ_0 is the residual surface stress or intrinsic surface stress, and sometimes is called "strain-independent" τ_0 of the surface stress [26, 27]. The surface elasticity tensor, S , can be defined as

$$S_{\alpha\beta\lambda\kappa} = \frac{d^2\gamma}{d\epsilon_{\alpha\beta} d\epsilon_{\lambda\kappa}} \quad (4)$$

The surface elastic properties can be determined from atomistic calculations [47, 48].

3. Nonlinear Distributed Electromechanical Coupled Model Incorporating Surface Effects

When a driving voltage is applied between the electrodes (cantilever or double clamped beam as movable electrodes and the substrate as a fixed electrode), the electrostatic pressure deflects the movable electrode. The mechanical bending strain energy U_b of the bulk is given by

$$U_b = \int_0^L \int_A \frac{1}{2} \sigma_{xx} \epsilon_{xx} dA dx, \quad (5)$$

where A is the cross-sectional area of the uniform beam, L is the length of the beam, σ_{xx} is the axial stress, and ϵ_{xx} is the normal strain, respectively. Using the linear strain-displacement relation

$$\epsilon_{xx} = \frac{\partial u}{\partial x} = -z \frac{d^2 w}{dx^2} \quad (6)$$

we obtain

$$U_b = \int_0^L \int_A \frac{E}{2} \left(-z \frac{d^2 w}{dx^2} \right)^2 dA dx = \int_0^L \frac{EI}{2} \left(\frac{d^2 w}{dx^2} \right)^2 dx, \quad (7)$$

where u and w are in-plane and transverse displacement components of the midplane, E is the Young's modulus, and I is the effective moment of inertia of the cross section, respectively. The transverse coordinate is z and the midplane coincides with $z = 0$. The total surface energy U_s , at the entire beam surface is

$$U_s = 2 \int_s (\gamma(\epsilon) - \gamma(0)) ds = 2 \int_s \frac{1}{2} S \epsilon^2 ds = \int_s S b t^2 \left(\frac{d^2 w}{dx^2} \right)^2 dx, \quad (8)$$

where S is the surface elasticity, b is the width of the cantilever, s is the surface area of the beam and t is the thickness of the cantilever, respectively. Residual stress, due to the inconsistency of both the thermal expansion coefficient and the crystal lattice period between the substrate and thin film, is unavoidable and the residual force can be expressed as [49]:

$$T_r = \sigma_r (1 - \nu) b t, \quad (9)$$

where σ_r is the biaxial residual stress (equal to zero for the cantilever beams), and ν is the Poisson's ratio. In double clamped beams, the intrinsic residual stress, or the strain-independent surface stress τ_0 modifies the residual stress, therefore, the energy stored in the beam due to the residual stress and strain-independent surface stress is.

$$U_r = \int_0^L T_r \left(\frac{dw}{dx} \right)^2 dx + \int_0^L 2b\tau_0 \left(\frac{dw}{dx} \right)^2 dx = \int_0^L (1 - \nu) b \left(t\sigma_r + \frac{2\tau_0}{(1 - \nu)} \right) \left(\frac{dw}{dx} \right)^2 dx. \quad (10)$$

When a beam is in tension, the actual beam length \tilde{L} is longer than the original length L . In double clamped beams, although there is no displacement in the x -direction at the beam ends, the bending of the beam generates an axial force, i.e.

$$T_a = \frac{EA}{L} (\tilde{L} - L) \approx \frac{Ebt}{2L} \int_0^L \left(\frac{dw}{dx} \right)^2 dx \quad (11)$$

The surface elasticity, or strain-dependent surface stress modifies the axial force in the double clamped beam, consequently, the effective axial force is written as

$$\tilde{T}_a \approx \left(\frac{Ebt}{2L} + \frac{2Sb}{L} \right) \int_0^L \left(\frac{dw}{dx} \right)^2 dx \quad (12)$$

and the energy stored in the beam due to axial force is expressed as

$$U_a \approx \int_0^L \left(\frac{Ebt}{2L} \left(4 \frac{S}{Et} + 1 \right) \int_0^L \left(\frac{dw}{dx} \right)^2 dx \right) \left(\frac{dw}{dx} \right)^2 dx \quad (13)$$

The electrical co-energy U_e^* , which is the sum of the electrostatic energy stored between the upper and lower electrode of the beam and the electrostatic energy of the voltage source is given by:

$$U_e^* = \frac{1}{2} \int_0^L \frac{\epsilon_r \epsilon_0 b V^2}{(g - w(x))} dx \quad (14)$$

The total potential energy U of the system is

$$U = U_b + U_s - U_r - U_a + U_e. \quad (15)$$

The variation of total energy is zero at the equilibrium position, i.e.

$$\delta U = \delta U_b + \delta U_s - \delta U_r - \delta U_a + \delta U_e = 0 \quad (16)$$

Therefore, the nonlinear integro-differential equation of a double clamped beam subjected to an applied voltage with surface effects can be written as

$$\begin{aligned} EI(24\lambda + 1) \frac{d^4 w}{dx^4} & - \left(bt\sigma_r(1 - \nu)(1 + 2\beta) \right. \\ & + \frac{Ebt}{2L} (4\lambda + 1) \int_0^L \left(\frac{dw}{dx} \right)^2 dx \left. \right) \frac{d^2 w}{dx^2} \\ & = \frac{\epsilon_r \epsilon_0 b V^2}{2(g - w(x))^2} (1 + f_f) \end{aligned} \quad (17)$$

where non-dimensional parameters λ and β are defined as

$$\lambda = \frac{S}{Et} \text{ and } \beta = \frac{\tau_0}{(1 - \nu)\sigma_r t} \quad (18)$$

and

$$f_f = 0.65 \left(\frac{g - w(x)}{b} \right) \quad (19)$$

is the first-order fringing field correction. Cantilevers have no residual and axial stress, thus, the nonlinear differential equation is written as

$$EI(24\lambda + 1) \frac{d^4 w}{dx^4} = \frac{\epsilon_r \epsilon_0 b V^2}{2(g - w(x))^2} (1 + f_f) \quad (20)$$

In cantilevers, only surface elasticity changes the bending stiffness, but in double clamped beams, both surface elasticity and surface stress come into play. One can get the traditional electromechanical coupled equation of cantilevers and double clamped beams [42], without surface effects if $\lambda = \beta = 0$.

4. Results and Discussion

The numerical examples of a cantilever and a double clamped beam made of single crystal silicon subjected to a voltage are now presented. The generalized differential quadrature method (GDQM) [42] is used to transform the aforementioned nonlinear integro-differential equations into the corresponding discrete forms and the NewtonRaphson method is implemented for solving the set of nonlinear algebraic equations that result from the application of GDQM. The material properties are given as follows [50]: Young's modulus E is 169 GPa, Poissons ratio is 0.06, and the permittivity of air is 8.85 pF/m. The width is kept constant and is 4 μm .

Fig. 1 shows $\frac{|\Delta V|}{V}(\%)$ as a function of surface elasticity S and thickness, where ΔV is the shift in the EPI due to the surface effects and V is the EPI without the surface effects. It can be seen that reducing the thickness of cantilever results in a bigger change in the EPI for a constant S . For cantilevers thinner than 50 nm, the EPI is sufficiently sensitive to the surface elasticity and, therefore, in practice, it is possible to track the changes in the surface elasticity due to either molecular adsorption [51, 20] or surface reconstruction [52, 20, 16]. The bending of the cantilever subjected to a voltage is also influenced by the surface elasticity. According to equation 8, negative/positive surface elasticity reduces/increases the bending stiffness of the cantilever, and that changes the bending behavior. This is shown in Fig. 2. The inset shows the non-dimensional difference of the end tip of the cantilever versus non-dimensional parameter λ . The cantilever modeled in Fig. 2 is 10 nm thick and 10 μm long.

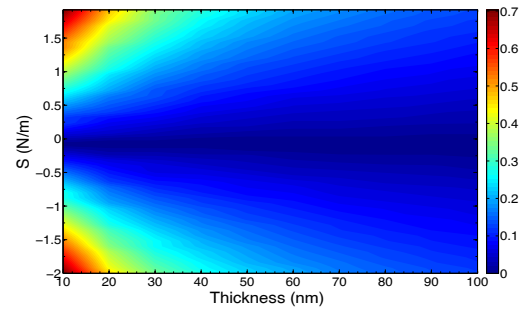


Fig. 1. Non-dimensional changes in pull-in voltage, $\frac{|\Delta V|}{V}(\%)$, of cantilever due to surface elasticity for various thicknesses.

Fig. 3. (a)-(f) shows the results for double clamped beams. Fig. 3. (a) shows the $\frac{|\Delta V|}{V}(\%)$ for various lengths and thicknesses. τ_0 and S are kept as 1 N/m [27]. The initial gap g is 1 μm and the residual stress σ_r is assumed zero. One can learn from the figure that increasing the surface to volume ratio (reducing the thickness), while keeping the lateral dimensions constant, results in a higher shifts in the EPI.

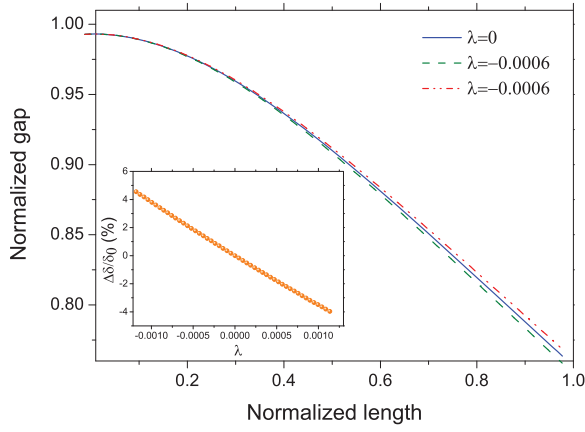


Fig. 2. Normalized deflection of a 10 nm thick silicon cantilever for different. The inset shows relative difference between the end tip of the cantilever incorporating surface elasticity and the end tip of the cantilever with no surface elasticity.

Increasing the length would cause increase in the EPI as well. Moreover, it can be seen that even for thicker double clamped beams, i.e. 1 μm , the shift in the EPI is significant. This is due to the fact that unlike cantilevers, in double clamped beams the residual surface stress τ_0 modifies the residual stress in the beam, because the beam is clamped in both sides and therefore it cannot release the stress. It has been shown that the residual stress is the most dominant effects on the EPI [42], and, consequently, the residual surface stress has a great impact on the EPI of double clamped beams.

Fig. 3. (b) shows the effects of τ_0 , while varying the thickness. τ_0 is varying from negative (compressive surface stress) to positive values (tensile surface stress). As it is expected, reducing the thickness would increase the sensitivity of the EPI to τ_0 . Longer double clamped beams also show the same, see Fig. 3. (c).

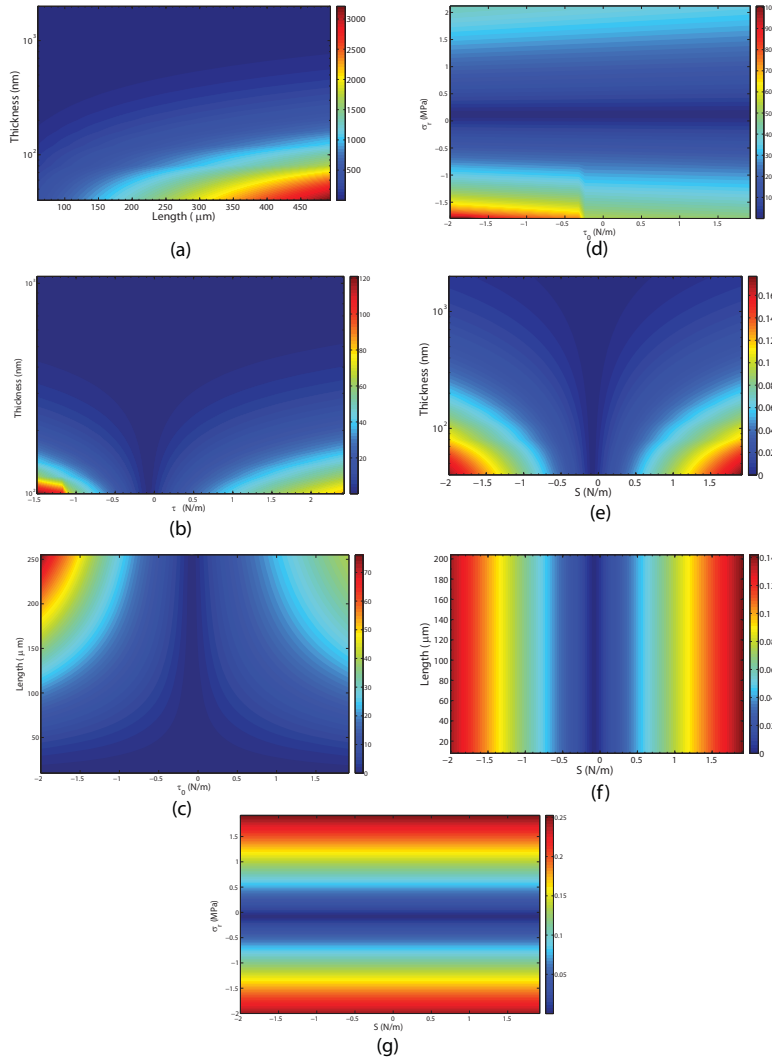


Fig. 3. Non-dimensional changes in pull-in voltage, $\frac{|\Delta V|}{V}(\%)$, of double clamped beam due to surface effects. (a) Effects of the thickness and the length on $\frac{|\Delta V|}{V}$, (b), (c), and (d) Effects of τ_0 in different thicknesses, lengths and residual stress on $\frac{|\Delta V|}{V}$, (e) and (f) Effects of surface elasticity S on $\frac{|\Delta V|}{V}$ for various thicknesses and lengths. (g) Effects of surface elasticity as well as residual stress.

The results are demonstrated for a 100 nm thick beam and σ_r is zero. As discussed above, the residual stress, which is exhibited due to fabrication, plays a substantial role for the EPI [42, 53]. The residual stress, σ_r can be either compressive (negative) or tensile (positive). The compressive one causes buckling of the beam, reducing the gap between the beam and the substrate, and consequently, decreasing the pull-in voltage. Negative τ_0 induces the same. This is shown in Fig. 3. (d). As it is shown in equations 8 and 13, the surface elasticity S modifies the bending stiffness as well as the axial force. The negative S causes softening of the beam and the positive one induces a stiffening effect. Figs. 3 (e) and 3 (f) show the effect of S on the pull-in voltage, while changing the thickness and the length of the double clamped beam. Increasing the surface to volume ratio (Figs. 3. (e)) increases the sensitivity of $\frac{|\Delta V|}{V}(\%)$ to S . For a fix thickness, scaling the lateral dimension, i.e., changing the length does not influence the $\frac{|\Delta V|}{V}(\%)$, see Fig. 3 (f). The bending properties of the double clamped beam, due to applied voltage also depend on the surface effects.

Under the same voltage, when the surface effects are considered the bending is significantly different from the case of no surface effects. This is shown in Fig. 4. Unlike cantilevers, not only the surface elasticity S influences the bending, but also the residual surface stress τ_0 .

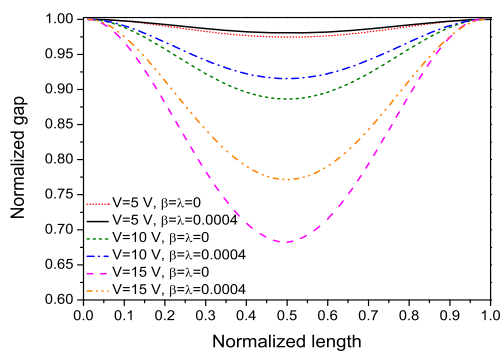


Fig. 4. Deflection of a 500 nm thick, 100 μm long double clamped beam subjected to applied voltage. The surface effects induce changes in the bending properties.

5. Conclusions

In this paper, the effects of surface stress and surface elasticity on the electrostatic pull-in instability (EPI) of micro/nano cantilevers and double clamped beams were studied. The nonlinear electromechanical coupled model of cantilevers and double clamped beams incorporating the surface effects were developed. The model showed in detail the contribution of residual surface stress and surface

elasticity on the bending stiffness, effective residual stress, and the axial stress. A major conclusion is that unlike the resonance frequency method, the EPI is free from mass loading effects, and thus it can be used for quantitative measurements of surface stress and surface elasticity. Compared to resonance frequency measurements, with EPI a relatively thicker structures can be used for surface stress sensing. Moreover, the theoretical results reveal that a high quality factor cantilever or double clamped beam, which is still required and this appears to rule out the use of the resonance frequency method for bio-molecular sensing, is not an issue for the EPI.

Acknowledgments

This research was financially supported by Early Research Program (ERP) 3D Nanomanufacturing at Netherlands Organization for Applied Scientific Research (TNO).

References

- [1]. R. J. Needs, M. J. Godfrey, M. Mansfield, Theory of surface stress and surface reconstruction, *Surface Science*, 242, 1-3, 1991, pp. 215-221.
- [2]. J. Diao, K. Gall, M. L. Dunn, Surface-stress-induced phase transformation in metal nanowires, *Nat Mater*, 2, 10, 2003, pp. 656-660.
- [3]. F. D. Fischer, T. Waitz, D. Vollath, N. K. Simha, On the role of surface energy and surface stress in phase-transforming nanoparticles, *Progress in Materials Science*, 53, 3, 2008, pp. 481-527.
- [4]. J. Lao, D. Moldovan, Surface stress induced structural transformations and pseudoelastic effects in palladium nanowires, *Applied Physics Letters*, 93, 9, 2008, p. 093108.
- [5]. H. Ibach, The role of surface stress in reconstruction, epitaxial growth and stabilization of mesoscopic structures, *Surface Science Reports*, 29, 5-6, 1997, pp. 195-263.
- [6]. R. Berger, E. Delamarche, H. P. Lang, C. Gerber, J. K. Gimzewski, E. Meyer, H.-J. Guntherodt, Surface Stress in the Self-Assembly of Alkanethiols on Gold, *Science*, 276, 5321, 1997, pp. 2021-2024.
- [7]. D. Sander, Surface stress: implications and measurements, *Current Opinion in Solid State and Materials Science*, 7, 1, 2003, pp. 51-57.
- [8]. G. G. Stoney, The tension of metallic films deposited by electrolysis, *Proceedings of the Royal Society of London. Series A*, 82, 1909, pp. 172-175.
- [9]. E. Carlen, M. Weinberg, A. Zapata, J. Borenstein, A micromachined surface stress sensor with electronic readout, *Review of Scientific Instruments*, 79, 1, 2008, p. 015106.
- [10]. S. Kim, K. D. Kihm, Effect of adsorption-induced surface stress change on the stiffness of a microcantilever used as a salinity detection sensor, *Applied Physics Letters*, 93, 8, 2008, pp. 081911.
- [11]. J. Tamayo, V. Pini, P. Kosaka, N. F. Martinez, O. Ahumada, M. Calleja, Imaging the surface stress and vibration modes of a microcantilever by laser beam deflection microscopy, *Nanotechnology*, 23, 31, 2012, pp. 315501.

- [12]. J. Tamayo, J. J. Ruz, V. Pini, P. Kosaka, M. Calleja, Quantification of the surface stress in microcantilever biosensors: revisiting stoneys equation, *Nanotechnology*, 23, 47, 2012, pp. 475702.
- [13]. R. B. Karabalin, L. G. Villanueva, M. H. Matheny, J. E. Sader, M. L. Roukes, Stress-induced variations in the stiffness of micro- and nanocantilever beams, *Phys. Rev. Lett.*, 108, 2012, pp. 236101.
- [14]. R. J. Needs, Calculations of the surface stress tensor at aluminum, 111, pp. and, 110, pp. surfaces, *Phys. Rev. Lett.*, 58, 1, 1987, pp. 53–56.
- [15]. R. Dingreville, J. Qu, A semi-analytical method to compute surface elastic properties, *Acta Materialia*, 55, 1, 2007, pp. 141–147.
- [16]. Effects of size and surface on the elasticity of silicon nanoplates: Molecular dynamics and semicontinuum approaches, *Thin Solid Films*, 520, 1, 2011, pp. 391–399.
- [17]. H. Sadeghian, H. Goosen, A. Bossche, B. Thijssse, F. van Keulen, On the size-dependent elasticity of silicon nanocantilevers: impact of defects, *Journal of Physics D: Applied Physics*, 44, 7, 2011, pp. 072001.
- [18]. F. H. Streitz, R. C. Cammarata, K. Sieradzki, Surface-stress effects on elastic properties. i. thin metal films, *Phys. Rev. B*, 49, 15, 1994, pp. 10699–10706.
- [19]. R. Dingreville, J. Qu, Interfacial excess energy, excess stress and excess strain elastic solids: Planar interfaces, *Journal of the Mechanics and Physics of Solids*, 56, 5, 2008, pp. 1944–1954.
- [20]. H. Sadeghian, J. F. L. Goosen, A. Bossche, F. van Keulen, Surface stress-induced change in overall elastic behavior and self-bending of ultrathin cantilever plates, *Applied Physics Letters*, 94, 23, 2009, pp. 231908.
- [21]. H.-J. Butt, A sensitive method to measure changes in the surface stress of solids, *Journal of Colloid and Interface Science*, 180, 1, 1996, pp. 251–260.
- [22]. S. J. O'Shea, M. E. Welland, T. A. Brunt, A. R. Ramadan, T. Rayment, Atomic force microscopy stress sensors for studies in liquids, *Journal of Vacuum Science and Technology B: Microelectronics and Nanometer Structure*, 14, 1996, pp. 1383–1385.
- [23]. R. McKendry, J. Zhang, Y. Arntz, T. Strunz, M. Hegner, H. P. Lang, M. K. Baller, U. Certa, E. Meyer, H.-J. Gntherodt, C. Gerber, Multiple label-free biodetection and quantitative DNA binding assays on a nanomechanical cantilever array, *Proceedings of the National Academy of Sciences of the United States of America*, 99, 15, 2002, pp. 9783–9788.
- [24]. Y. T. Yang, C. Callegari, X. L. Feng, K. L. Ekinci, M. L. Roukes, Zeptogram-scale nanomechanical mass sensing, *Nano Letters*, 6, 4, 2006, pp. 583–586.
- [25]. J. Lagowski, H. C. Gatos, J. E. S. Sproles, Surface stress and the normal mode of vibration of thin crystals :gaas, *Applied Physics Letters*, 26, 9, 1975, pp. 493–495.
- [26]. M. E. Gurtin, X. Markenscoff, R. N. Thurston, Effect of surface stress on the natural frequency of thin crystals, *Applied Physics Letters*, 29, 9, 1976, pp. 529–530.
- [27]. P. Lu, H. P. Lee, C. Lu, S. J. O'She, Surface stress effects on the resonance properties of cantilever sensors, *Physical Review B*, 72, 8, 2005, pp. 085405.
- [28]. R. E. Miller, V. B. Shenoy, Size-dependent elastic properties of nanosized structural elements, *Nanotechnology*, 11, 3, 2000, pp. 139–147.
- [29]. G.-F. Wang, X.-Q. Feng, Effects of surface elasticity and residual surface tension on the natural frequency of microbeams, *Applied Physics Letters*, 90, 23, 2007, p. 231904.
- [30]. H. Sadeghian, C. K. Yang, J. F. L. Goosen, E. van der Drift, A. Bossche, P. J. French, F. van Keulen, Characterizing size-dependent effective elastic modulus of silicon nanocantilevers using electrostatic pull-in instability, *Applied Physics Letters*, 94, 22, 2009, p. 221903.
- [31]. H. Sadeghian, J. F. L. Goosen, F. Van Keulen, C.-K. Yang, A. Bossche, P. French, Quantitative analysis and decoupling of mass and stiffness effects in cantilever mass sensors, in *Proceedings of the IEEE Sensors*, 2010, pp. 631–634.
- [32]. H. Sadeghian, H. Goosen, A. Bossche, F. van Keulen, Application of electrostatic pull-in instability on sensing adsorbate stiffness in nanomechanical resonators, *Thin Solid Films*, 518, 17, 2010, pp. 5018–5021.
- [33]. D. Klymyshyn, D. Haluzan, M. Borner, S. Achenbach, J. Mohr, T. Mappes, High aspect ratio vertical cantilever RF-MEMS variable capacitor, *IEEE Microwave and Wireless Components Letters*, 17, 2, 2007, pp. 127–129.
- [34]. C. Goldsmith, J. Randall, S. Eshelman, T. Lin, D. Denniston, S. Chen, B. Norvell, Characteristics of micromachined switches at microwave frequencies, in: *IEEE MTT-S International Microwave Symposium Digest*, 1996, pp. 1141–1144.
- [35]. H. Sadeghian, G. Rezazadeh, Comparison of generalized differential quadrature and Galerkin methods for the analysis of micro-electro-mechanical coupled systems, *Communications in Nonlinear Science and Numerical Simulation*, 14, 6, 2009, pp. 2807–2816.
- [36]. V. Aksyuk, F. Pardo, D. Carr, D. Greywall, H. Chan, M. Simon, A. Gasparyan, H. Shea, V. Lifton, C. Bolle, S. Arney, R. Frahm, M. Paczkowski, M. Haueis, R. Ryf, D. Neilson, J. Kim, C. Giles, D. Bishop, Beam-steering micromirrors for large optical cross-connects, *Journal of Lightwave Technology*, 21, 3, 2003, pp. 634–642.
- [37]. B. Mi, D. Smith, H. Kahn, F. Merat, A. Heuer, S. Phillips, Static and electrically actuated shaped MEMS mirrors, *Journal of Microelectromechanical Systems*, 14, 1, 2005, pp. 29–36.
- [38]. M. Huff, M. Mettner, T. Lober, M. Schmidt, A pressure-balanced electrostatically-actuated microvalve, in *Proceedings of the IEEE Solid-State Sensor and Actuator Workshop, 4th Technical Digest*, 1990, pp. 123–127.
- [39]. W. W. Jang, J.-B. Yoon, M.-S. Kim, J.-M. Lee, S.-M. Kim, E.-J. Yoon, K. H. Cho, S.-Y. Lee, I.-H. Choi, D.-W. Kim, D. Park, NEMS switch with 30nm-thick beam and 20nm-thick air-gap for high density non-volatile memory applications, *Solid-State Electronics*, 52, 10, 2008, pp. 1578–1583.
- [40]. X. L. Feng, M. H. Matheny, C. A. Zorman, M. Mehregany, M. L. Roukes, Low voltage nanoelectromechanical switches based on silicon carbide nanowires, *Nano Letters*, 10, 8, 2010, pp. 2891–2896.
- [41]. J. B. Ma, L. Jiang, S. F. Asokanathan, Influence of surface effects on the pull-in instability of NEMS electrostatic switches, *Nanotechnology*, 21, 50, 2010, pp. 505708.
- [42]. H. Sadeghian, G. Rezazadeh, P. M. Osterberg, Application of the generalized differential quadrature method to the study of pull-in phenomena of MEMS switches, *IEEE/ASME Journal of*

- Microelectromechanical Systems*, 16, 6, 2007, pp. 1334–1340.
- [43]. J. W. Gibbs, H. A. Bumstead, W. R. Longley, R. G. V. Name, *The Collected Works of J. Willard Gibbs*, Longmans, Green and Co, 1928.
- [44]. R. Dingreville, J. Qu, M. Cherkaoui, Surface free energy and its effect on the elastic behavior of nano-sized particles, wires and films, *Journal of the Mechanics and Physics of Solids*, 53, 8, 2005, pp. 1827 – 1854.
- [45]. R. Shuttleworth, The surface tension of solids, *Proceedings of the Physical Society. Section A*, 63, 5, 1950, pp. 444–457.
- [46]. D. Kramer, J. Weissmüller, A note on surface stress and surface tension and their interrelation via Shuttleworth's equation and the Lippmann equation, *Surface Science*, 601, 14, 2007, pp. 3042–3051.
- [47]. P. Miller, A. Sal, Elastic effects on surface physics, *Surface Science Reports*, 54, 5-8, 2004, pp. 157–258.
- [48]. J. C. Hamilton, W. G. Wolfer, Theories of surface elasticity for nanoscale objects, *Surface Science*, 603, 9, 2009, pp. 1284–1291.
- [49]. R. K. Gupta, Electrostatic pull-in test structure design for in-situ mechanical property measurements of microelectromechanical systems MEMS), PhD Thesis, Massachusetts Institute of Technology. Dept. of Electrical Engineering and Computer Science, 1997.
- [50]. P. Osterberg, S. Senturia, M-test: A test chip for MEMS material property measurement using electrostatically actuated test structures, *Journal of Microelectro-mechanical Systems*, 6, 1997, pp. 107–118.
- [51]. J. Zang, F. Liu, Theory of bending of Si nanocantilevers induced by molecular adsorption: a modified stoney formula for the calibration of nanomechanical sensors, *Nanotechnology*, 18, 40, 2007, p. 405501, (4 pp).
- [52]. J. Zang, M. Huang, F. Liu, Mechanism for nanotube formation from self-bending nanofilms driven by atomic-scale surface-stress imbalance, *Physical Review Letters*, 98, 14, 2007, pp. 146102.
- [53]. H. Sadeghian, G. Rezazadeh, E. Abbaspour, A. Tahmasebi, I. Hosainzadeh, The effect of residual stress on pull-in voltage of fixed-fixed end type mem switches with variative electrostatic area, in *Proceedings of the 1st IEEE International Conference on Nano/Micro Engineered and Molecular Systems, (NEMS '06)*, 2006, pp. 1117–1120.



Published by International Frequency Sensor Association (IFSA) Publishing, S. L., 2017.
(<http://www.sensorsportal.com>).

NANOSENSORS: Materials and Technologies

Nada F. Atta, Ed.



Nanosensors: Materials and Technologies aims to provide the readers with some of the most recent development of new and advanced materials such as carbon nanotubes, graphene, sol-gel films, self-assembly layers in presence of surface active agents, nano-particles, and conducting polymers in the surface structuring for sensing applications. The emphasis of the presentations is devoted to the difference in properties and its relation to the mechanism of detection and specificity. Miniaturization on the other hand, is of unique importance for sensors applications. The chapters of this book present the usage of robust, small, sensitive and reliable sensors that take advantage of the growing interest in nano-structures. Different chemical species are taken as good example of the determination of different chemical substances industrially, medically and environmentally. A separate chapter in this book will be devoted to molecular recognition using surface templating.

The present book will find a large audience of specialists and scientists or engineers working in the area of sensors and its technological applications. The *Nanosensors: Materials and Technologies* will also be useful for researchers working in the field of electrochemical and biosensors since it presents a collection of achievements in different areas of sensors applications.

Order: http://www.sensorsportal.com/HTML/BOOKSTORE/Nanosensors_IFSA.htm

Trajectory Tracking Optimal Control for Nonholonomic Mobile Robot

Jianwei MA, Jiayu SHI and Haitao ZHANG

Henan University of Science & Technology, Luoyang, 471023, China

Tel.: 15236265350

E-mail: 137034342@qq.com

Received: 19 October 2016 /Accepted: 30 December 2016 /Published: 31 January 2017

Abstract: This paper discussed the problem of trajectory tracking control for the nonholonomic mobile robot's kinematic model with the angular speed of two actuated wheels as its control input. Based on the backstepping control algorithm, a sliding-mode variable structure switching function is designed, in order to improve the quality of motion control, fuzzy logic is used to adjust sliding-mode reaching law parameters. An adaptive control algorithm is proposed to compensate the unknown parameters, on the other hand. The stability of system is easily proven via the Lyapunov function. The simulation results are provided to illustrate the effectiveness of the controller.

Keywords: Mobile robot, Backstepping, Adaptive sliding mode control, Trajectory tracking.

1. Introduction

Motion control of mobile robots has been researchers' concern over the past few years. Many studies have proposed various trajectory tracking control methods considering the nonholonomic constraints of mobile robots. Kanayama, *et al.* [1] design a trajectory tracking control law only for linear systems. Walsh, *et al.* [2] designed a controller through linearizing nearby desired trajectory. Walsh, *et al.* [2] and Anesh [3] use the linearization idea of small disturbance of the model error to design controller, but the controllers do not achieve global stability control. Aneesh [3] designs a global tracking controller based on back-stepping nonlinear state feedback controller. Dong, *et al.* [4] use the backstepping method to determine nonlinear control law for the robot kinematics model and made sure the global asymptotic stability. Cheng [5] designs an asymptotic tracking controller based on global feedback control law. These methods regard the linear

velocity of mass center and the steering angular speed as control input, and then design global tracking controllers. These approaches may have some errors, because the angular velocity of the two rear wheels is used as a control input in most cases. Hoang, *et al.* [6] and Wang, *et al.* [7] design trajectory tracking global asymptotically stable controllers and regard the two rear wheels as the control input for the kinematics model. But these controllers did not consider the influence of unknown parameters for trajectory tracking, they have limitations. Huang, *et al.* [8] consider the influence of unknown parameters, and adaptive control algorithm is used to achieve the robust controlling in that environment.

But in practice, the sliding mode control rate parameters will directly influence the control effect. The process of selecting parameters is a troublesome business, and it is not easy to find the best parameters. In this paper we adjust sliding mode reaching law parameters through fuzzy logic to realize the aim of improving the sliding mode motion quality.

Accordingly, this paper concentrates on the tracking control problem of mobile robots with unknown parameters. Based on the backstepping control algorithm, a switch function for variable structure is designed and an adaptive control method is presented to compensate the parameter uncertainties. Moreover, in order to improve the quality of motion control, fuzzy logic is used to adjust sliding mode reaching law parameters. And based on Lyapunov direct method, it's proved that the proposed controller can make globally asymptotically stable.

The paper is organized as follows: Kinematics model of mobile robot is given in Section 2. The trajectory tracking controller is proposed in Section 3, at the same time, the robustness and global stability of the proposed controller is proven by Lyapunov stability theory. Simulation results are shown in Section 4. Section 5 is devoted to concluding remarks.

2. Mobile Robot Kinematics Model

The mobile robot configuration is shown in Fig. 1. It has two differentially driven wheels and a front free wheel.

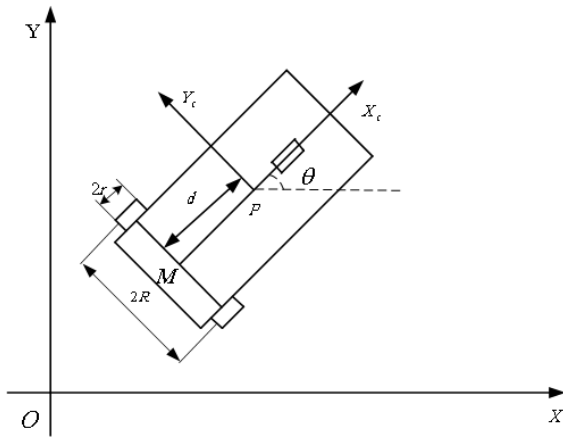


Fig. 1. Mobile robot coordinate system.

Where both wheels have the same radius denoted by r . The two driven wheels are separated by $2R$. M is located in the middle of two driven wheels. d is the distance between P and the axis of the driving wheels. The mobile robot can be described with pose vector: $q = [x \ y \ \theta]^T$, where (x, y) is the centre of mobile robot in Cartesian coordinate system, and θ is the angle between the forward direction and the x-axis. The mobile robot satisfies the conditions of pure rolling and no slipping in wheels [9], and we can get:

$$\dot{x} \sin \theta - \dot{y} \cos \theta - d \dot{\theta} = 0 \quad (1)$$

The kinematics model of nonholonomic mobile robot is described by the following differential equation.

$$\begin{bmatrix} \dot{x} \\ \dot{y} \\ \dot{\theta} \end{bmatrix} = \begin{bmatrix} \frac{r}{2} \cos \theta + \frac{r}{2R} d \sin \theta & \frac{r}{2} \cos \theta - \frac{r}{2R} d \sin \theta \\ \frac{r}{2} \sin \theta - \frac{r}{2R} d \cos \theta & \frac{r}{2} \sin \theta + \frac{r}{2R} d \cos \theta \\ \frac{r}{2R} & -\frac{r}{2R} \end{bmatrix} \begin{bmatrix} \omega_1 \\ \omega_2 \end{bmatrix}, \quad (2)$$

where ω_1 and ω_2 is the angular velocities of right and left wheels.

The relationship between linear and angular velocities is shown as

$$\begin{bmatrix} \omega_1 \\ \omega_2 \end{bmatrix} = \begin{bmatrix} 1/r & R/r \\ 1/r & -R/r \end{bmatrix} \begin{bmatrix} v \\ \omega \end{bmatrix}, \quad (3)$$

where v is the heading linear velocity, ω is the heading angular velocity.

Substituting (3) into (2)

$$\begin{bmatrix} \dot{x} \\ \dot{y} \\ \dot{\theta} \end{bmatrix} = \begin{bmatrix} \cos \theta & d \sin \theta \\ \sin \theta & -d \sin \theta \\ 0 & 1 \end{bmatrix} \begin{bmatrix} v \\ \omega \end{bmatrix} \quad (4)$$

In the mobile robot coordinate system, the position and orientation error can be defined as $p_e = (x_e \ y_e \ \theta_e)^T$

$$p_e = \begin{pmatrix} x_e \\ y_e \\ \theta_e \end{pmatrix} = \begin{pmatrix} \cos \theta & \sin \theta & 0 \\ -\sin \theta & \cos \theta & 0 \\ 0 & 0 & 1 \end{pmatrix} \begin{pmatrix} x_r - x \\ y_r - y \\ \theta_r - \theta \end{pmatrix} \quad (5)$$

Take the derivative \dot{P}_e of P_e and mobile robot tracking error differential equation can be obtained as

$$\begin{bmatrix} \dot{x}_e \\ \dot{y}_e \\ \dot{\theta}_e \end{bmatrix} = v \begin{bmatrix} -1 \\ 0 \\ 0 \end{bmatrix} + \omega \begin{bmatrix} y_e \\ -x_e + d \\ -1 \end{bmatrix} + \begin{bmatrix} v_r \cos \theta_e + d \omega_r \sin \theta_e \\ v_r \sin \theta_e - d \omega_r \cos \theta_e \\ \omega_r \end{bmatrix} \quad (6)$$

If ω_1 and ω_2 is used to denote it, mobile robot tracking error differential equation can also be obtained as

$$\begin{bmatrix} \dot{x}_e \\ \dot{y}_e \\ \dot{\theta}_e \end{bmatrix} = \omega_1 \begin{bmatrix} -\frac{r}{2} + \frac{r}{2R} y_e \\ -\frac{r}{2R} x_e + \frac{r}{2R} \\ -\frac{r}{2R} \end{bmatrix} + \omega_2 \begin{bmatrix} -\frac{r}{2} - \frac{r}{2R} y_e \\ \frac{r}{2R} x_e - \frac{r}{2R} \\ \frac{r}{2R} \end{bmatrix} + \begin{bmatrix} v_r \cos \theta + d \omega_r \sin \theta_e \\ v_r \sin \theta - d \omega_r \cos \theta \\ \omega_r \end{bmatrix}, \quad (7)$$

where V_r and ω_r denote the reference time-varying linear and angular velocity.

The trajectory tracking control problem is how to design proper angular velocities ω_1 and ω_2 respectively to make $p_e = (x_e \ y_e \ \theta_e)^T$ globally asymptotically stable and satisfy $\lim_{t \rightarrow \infty} \|(x_e \ y_e \ \theta_e)^T\| = 0$.

Mobile robot kinematics model is a complex multi-input nonlinear system, and the switching functions can be designed based on back-stepping control algorithm.

3. Tracking Controller

3.1. Switching Functions

When $x_e = 0$, given model part Lyapunov function $V_y = \frac{1}{2} y_e^2$.

Suppose $\theta_e = -\arctan(v_r y_e)$, so

$$\dot{V}_y = y_e \dot{y}_e = -y_e x_e \omega - v_r y_e \sin(\arctan(v_r y_e)) \quad (8)$$

if and only if $v_r y_e = 0, \dot{V}_y \leq 0$.

When $\theta_e = -\arctan(v_r y_e)$, y_e converges. Thus, if x_e and y_e can converge to zero and θ_e converges $-\arctan(v_r y_e)$ to, the state of the system is convergent.

According to this conclusion, the switching function can be designed as

$$s = \begin{bmatrix} s_1 \\ s_2 \end{bmatrix} = \begin{bmatrix} x_e \\ \theta_e + \arctan(v_r y_e) \end{bmatrix} \quad (9)$$

So if we can make sure $s_1 \rightarrow 0, s_2 \rightarrow 0$, x_e can converge to zero, θ_e converge to zero, and we can achieve $y_e \rightarrow 0$ and $\theta_e \rightarrow 0$.

3.2. Sliding-Mode Controller

The method combining power reaching law with exponent reaching law can improve approaching quality, sliding mode reaching law can be designed as

$$\dot{s} = -k_1 |s|^\alpha \text{sgn}(s) - k_2 s, \quad (10)$$

where $k_1 > 0, k_2 > 0, 0 < \alpha < 1$.

In order to reduce the chattering, the continuous function can be used to replace sign function

$$\dot{s}_i = -k_{i1} |s_i|^{\alpha_i} \frac{s_i}{|s_i| + \delta_i} - k_{i2} s_i, i = 1, 2, \quad (11)$$

where δ_i is a positive value.

Substituting Equation (6) into (9), we can get

$$\begin{aligned} \dot{s} &= \begin{bmatrix} \dot{s}_1 \\ \dot{s}_2 \end{bmatrix} \\ &= \begin{bmatrix} y_e \omega - v_r + v_r \cos \theta_e + d \omega_r \sin \theta_e \\ \omega_r - \omega + \frac{\partial \xi}{\partial v_r} \dot{v}_r + \frac{\partial \xi}{\partial y_e} \\ (-x_e \omega + v_r \sin \theta_e - d \omega_r \cos \theta_e + d \omega) \end{bmatrix}, \quad (12) \end{aligned}$$

where $\xi = \arctan(v_r y_e)$.

Then we can get control law

$$q = \begin{bmatrix} v \\ \omega \end{bmatrix} = \begin{bmatrix} y_e \omega + v_r \cos \theta_e + d \omega_r \sin \theta_e \\ +k_{11} |s_1|^{\alpha_1} \frac{s_1}{|s_1| + \delta_1} + k_{12} s_1 \\ [\omega_r + \frac{\partial \xi}{\partial v_r} \dot{v}_r + \frac{\partial \xi}{\partial y_e} (v_r \sin \theta_e - d \omega_r \cos \theta_e) \\ +k_{21} |s_2|^{\alpha_2} \frac{s_2}{|s_2| + \delta_2} + k_{22} s_2] \\ (1 + \frac{\partial \xi}{\partial y_e} x_e - \frac{\partial \xi}{\partial y_e} d) \end{bmatrix}, \quad (13)$$

where $\frac{\partial \xi}{\partial v_r} = \frac{y_e}{1 + (v_r y_e)^2}, \frac{\partial \xi}{\partial y_e} = \frac{v_r}{1 + (v_r y_e)^2}$.

k_{i1} and k_{i2} can be given directly, but this method does not take into account the approaching time and

chattering. The process of selecting parameters is a troublesome business, and it is not easy to find the best parameters. In order to improve the quality of the motion, we introduce fuzzy logic to solve this problem [10].

3.3. Fuzzy Controller

Considering approaching law $\dot{s} = -k_1 |s|^\alpha \text{sgn}(s) - k_2 s$ (k_1 and k_2 represent the approaching velocity), through real-time adjustment of two parameters, we can achieve fast and stable tracking control system.

We can select $|s_1|$ as the input variable of fuzzy controller, and k_{11} and k_{12} as the fuzzy controller's output variables. Fuzzy sets are defined as: VS (Very small), S (small), M (Medium), B (Big), VB (Very big). The size of input ($|s_1|$) and output (k_{11} and k_{12}) are selected as [0,4] and [0,100]. According to the relevant control experience, fuzzy control rules are designed as: when $|s_1|$ is VS, in fuzzy role, k_{11} and k_{12} should be VS. The fuzzy logic control rule is designed as Table 1:

Table 1. Fuzzy logical control rules.

$ s_1 $	VS	S	M	B	VB
k_{11}	VS	S	M	B	VB
k_{12}	VS	S	M	B	VB

Another fuzzy logic control rule can be designed for another input variable $|s_2|$, and output variables k_{21} and k_{22} can be selected in the same way.

But the angular velocities ω_1 and ω_2 can't still be obtained due to the unknown parameters r and b .

3.4. Adaptive Controller

The adaptive algorithm can be used to estimate two unknown parameters. The control input ω_1 and ω_2 are designed as

$$\begin{aligned} \begin{bmatrix} \omega_1 \\ \omega_2 \end{bmatrix} &= \begin{bmatrix} \hat{\beta}_1 & \hat{\beta}_2 \\ \hat{\beta}_1 & -\hat{\beta}_2 \end{bmatrix} \begin{bmatrix} v \\ \omega \end{bmatrix} \\ &= \begin{bmatrix} \beta_1 + \hat{\beta}_1 & \beta_2 + \hat{\beta}_2 \\ \beta_1 + \hat{\beta}_1 & -\beta_2 - \hat{\beta}_2 \end{bmatrix} \begin{bmatrix} v \\ \omega \end{bmatrix}, \end{aligned} \quad (14)$$

where $\beta_1 = 1/r$, $\beta_2 = R/r$, $\hat{\beta}_1$ and $\hat{\beta}_2$ are their estimated value, $\beta_1 = \hat{\beta}_1 - \tilde{\beta}_1$, $\beta_2 = \hat{\beta}_2 - \tilde{\beta}_2$.

Substituting (14) into (7), we can get

$$\begin{aligned} \begin{bmatrix} \dot{x}_e \\ \dot{y}_e \\ \dot{\theta}_e \end{bmatrix} &= \begin{pmatrix} 1 + \frac{\tilde{\beta}_1}{\beta_1} \end{pmatrix} v \begin{bmatrix} -1 \\ 0 \\ 0 \end{bmatrix} + \begin{pmatrix} 1 + \frac{\tilde{\beta}_2}{\beta_2} \end{pmatrix} \omega \begin{bmatrix} y_e \\ -x_e + d \\ -1 \end{bmatrix} \\ &+ \begin{bmatrix} v_r \cos \theta_e + d \omega_r \sin \theta_e \\ v_r \sin \theta_e - d \omega_r \cos \theta_e \\ \omega_r \end{bmatrix} \end{aligned} \quad (15)$$

The Lyapunov functional candidate is defined as

$$V = \frac{1}{2} s_1^2 + \frac{1}{2} s_2^2 + \frac{1}{2\gamma_1 \beta_1} \tilde{\beta}_1^2 + \frac{1}{2\gamma_2 \beta_2} \tilde{\beta}_2^2 \quad (16)$$

Clearly $V \geq 0$, differentiating (16), we can obtain that

$$\begin{aligned} \dot{V} &= s_1 \dot{s}_1 + s_2 \dot{s}_2 + \frac{\tilde{\beta}_1}{2\gamma_1 \beta_1} \dot{\tilde{\beta}_1} + \frac{\tilde{\beta}_2}{2\gamma_2 \beta_2} \dot{\tilde{\beta}_2} \\ &= -k_{11} |s_1|^{\alpha_1} \frac{s_1^2}{|s_1| + \delta_1} - k_{12} s_1^2 - k_{21} |s_2|^{\alpha_2} \frac{s_2^2}{|s_2| + \delta_2} - k_{22} s_2^2 + \frac{\tilde{\beta}_1}{\gamma_1 \alpha_1} \left(\dot{\tilde{\beta}_1} - \gamma_1 s_1 v \right) + \frac{\dot{\tilde{\beta}_2}}{\gamma_2 \beta_2} \\ &\quad \left[\dot{\tilde{\beta}_2} + \gamma_2 s_2 y_e \omega - \gamma_2 \omega s_2 \left(1 + \frac{\partial \xi}{\partial y_e} (x_e - d) \right) \right] \end{aligned} \quad (17)$$

In order to make sure $\dot{V} \leq 0$, the parameter adaptive law can be designed as

$$\begin{aligned} \dot{\hat{\beta}_1} &= \gamma_1 s_1 v \\ \dot{\hat{\beta}_2} &= -\gamma_2 s_2 y_e \omega + \gamma_2 \omega s_2 \left(1 + \frac{\partial \xi}{\partial y_e} (x_e - d) \right) \\ &+ f(\hat{\beta}_2), \end{aligned} \quad (18)$$

$$\text{where } f(\hat{\beta}_2) = \begin{cases} 0 & \hat{\beta}_2 > \lambda \\ (\lambda - \hat{\beta}_2)(f_0 - \lambda)^2 & \hat{\beta}_2 \leq \lambda \end{cases},$$

$$f_0 = -\gamma_2 s_2 y_e \omega + \gamma_2 \omega s_2 \left(1 + \frac{\partial \xi}{\partial y_e} (x_e - d) \right),$$

$$0 < \lambda \leq \beta_2.$$

Substituting (18) into (17), we can get

$$\begin{aligned}
\dot{V} = & -k_{11}|s_1|^{\alpha_1} \frac{s_1^2}{|s_1| + \delta_1} - k_{12}s_1^2 \\
& -k_{21}|s_2|^{\alpha_2} \frac{s_2^2}{|s_2| + \delta_2} - k_{22}s_2^2 + \frac{\tilde{\beta}_2 - \beta_2}{\gamma_2\beta_2} f(\hat{\beta}_2) \quad (19) \\
\leq & -k_{12}s_1^2 - k_{22}s_2^2 + \frac{\tilde{\beta}_2 - \beta_2}{\gamma_2\beta_2} f(\hat{\beta}_2)
\end{aligned}$$

When $\hat{\beta}_2 > \lambda$, $\dot{V} \leq 0$, when $\hat{\beta}_2 \leq \lambda$, $f(\hat{\beta}_2) \geq 0$ and $\hat{\beta}_2 - \beta_2 \leq \lambda - \beta_2 \leq 0$, thus $\dot{V} \leq 0$.

Therefore, when s_1 and s_2 can converge to zero, $\lim_{t \rightarrow \infty} y_e = 0$. When $v_r \neq 0$, $\lim_{t \rightarrow \infty} \theta_e = 0$ and it satisfies $\lim_{t \rightarrow \infty} \|(x_e \ y_e \ \theta_e)^T\| = 0$. The adaptive trajectory tracking controller is established, and its conclusion is given as follows:

Theorem 1. Assume $\forall t \in [0, +\infty)$, v_r , \dot{v}_r , ω_r and $\dot{\omega}_r$ are bounded. The nonholonomic robot tracking error system (7) is globally asymptotically stable under the control law (14) and parameter adaptive law (18), which satisfies $\lim_{t \rightarrow \infty} \|(x_e \ y_e \ \theta_e)^T\| = 0$.

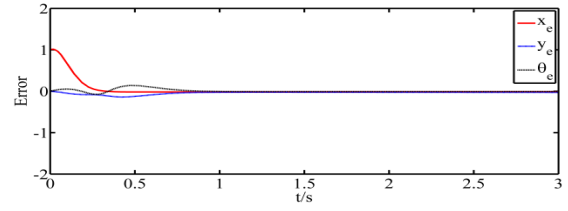
4. Simulation Research

In this section, a simulation is used to prove the effectiveness of the proposed controller which is designed in the previous section. The parameters of mobile robot are chosen as: $R = 0.75m$, $r = 0.15m$, $d = 0.3m$, where R and r are unknown. The desired trajectory are selected as $\omega_r = 1.0 \text{ rad/s}$, $v_r = 2.0 \text{ m/s}$, $x_r = r \cos(\omega_r t) = 2.0 \cos t$, $y_r = r \sin(\omega_r t) = 2.0 \sin t$, and $\theta_r = \omega_r t = t$. The parameters of controller are designed as: $\delta_1 = \delta_2 = 0.05$, $\alpha_1 = \alpha_2 = 0.5$, $\gamma_1 = \gamma_2 = 6$, the initial position and orientation error $P_e(0) = [1 \ 0 \ 0]^T$. The initial conditions are $\hat{\beta}_1(0) = \hat{\beta}_2(0) = 0$, when conventional controller is used, $k_{11} = k_{12} = k_{21} = k_{22} = 5$.

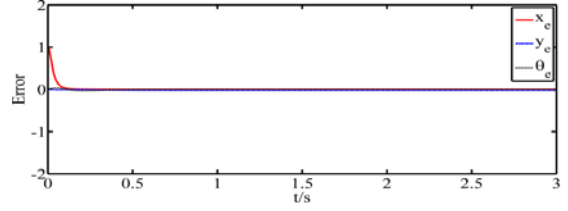
The simulation is carried out in MATLAB in 5 seconds. The comparison effect of the conventional sliding mode control and fuzzy sliding mode control after optimization are shown in Fig. 2 - Fig. 5.

Fig. 2 show that system position tracking error can converge to zero within 0.2 seconds under optimize control law, convergence speed is faster.

Fig. 3 show that actual velocities are almost confused with the desired velocities. The control law after optimization is better.

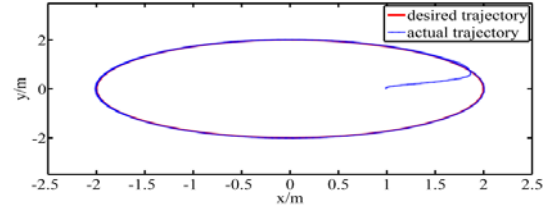


(a) Before optimization

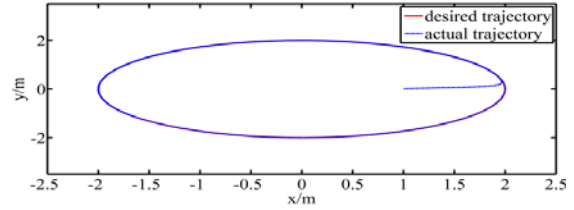


(b) After optimization

Fig. 2. The comparison of error.

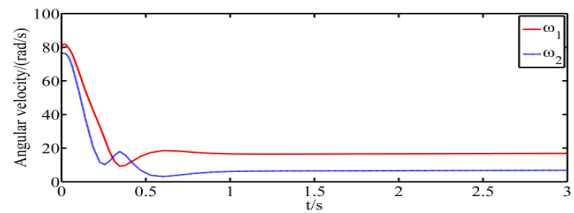


(a) Before optimization

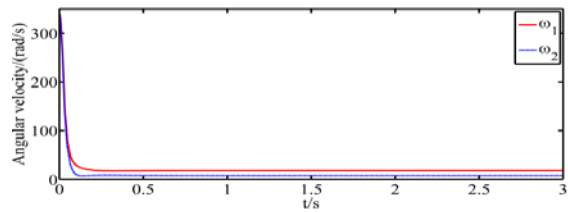


(b) After optimization

Fig. 3. The comparison of circular track position tracking.



(a) Before optimization



(b) After optimization

Fig. 4. The comparison of angular velocities control.

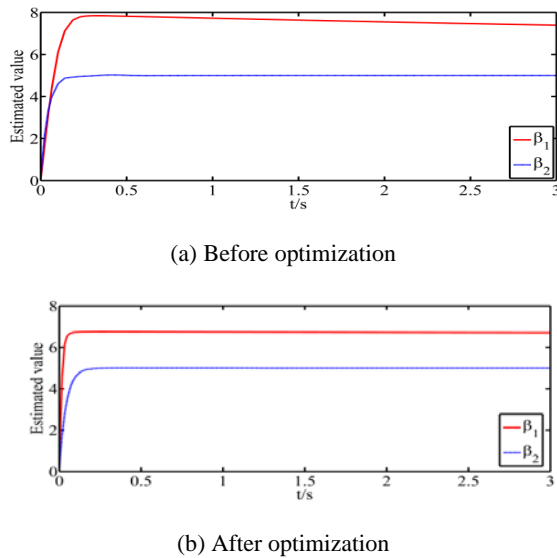


Fig. 5. The comparison of parameter estimation.

Fig. 4 show that control input torque can converge to a global bound state faster under optimize control law.

Fig. 5 show that the estimated parameters can converge to a global bound state faster under optimize control law.

5. Conclusions

The mobile robot trajectory tracking control problem is considered in this paper. The sliding mode control method is first designed based on back-stepping. Then fuzzy logic is proposed so as to improve the quality of the motion. Furthermore, an adaptive sliding mode control strategy is proposed to compensate the parametric uncertainties, and the globally asymptotic stability of the proposed controller is proved by Lyapunov theory. Finally the simulation results demonstrate that the optimal controller has a better control effect, this scheme is effective.

References

- [1]. Kanayama Y., Kimura Y., *et al.*, A stable tracking control method for an autonomous mobile robot, in *Proceeding of the IEEE Conference on Robotics and Automation*, 1990, pp. 184-189.
- [2]. Walsh G., Tilbury D., Sastry S., *et al.*, Stabilization of trajectories for systems with nonholonomic constraints, *IEEE Trans on Automatic Control*, Vol. 39, No. 1, 1994, pp. 216-222.
- [3]. Divya Aneesh, Tracking controller of mobile robot, in *Proceeding of IEEE Conference on Computing, Electronics and Electronics Technologies (ICCEET)*, 2012, pp. 343-349.
- [4]. F. Dong, W. Hinemann, R. Kasper, Nonlinear control design for row guidance system of an automated asparagus harvesting robot, in *Proceeding of the IEEE International Conference on Advanced Intelligent Macaronis*, 2011, pp. 1087-1092.
- [5]. L. Cheng, Trajectory tracking control of nonholonomic mobile robots by back-stepping, in *Proceeding of the International Conference on Modeling Identification and Control*, 2011, pp. 134-139.
- [6]. T. T. Hoang, D. T. Hiep, P. M. Duong, *et al.*, Proposal of algorithms for navigation and obstacles avoidance of autonomous mobile robot, in *Proceeding of the IEEE 8th Conference on Industrial Electronics and Applications*, 2013, pp. 1308-1313.
- [7]. J. H. Wang, Z. G. Lu, W. H. Chen, *et al.*, An adaptive trajectory tracking control of wheeled mobile robots, in *Proceeding of the 6th IEEE Conference on Industrial Electronics and Applications*, 2011, pp. 1156-1160.
- [8]. Dawei Huang, Junyong Zhai, Trajectory tracking control of wheeled mobile robots based on disturbance observer, in *Proceeding of the Chinese Automation Congress (CAC)*, 2015, pp. 1761-1765.
- [9]. J. Barraquand, J. C. Latombe, Nonholonomic multibody mobile robots controllability and motion planning in the presence of obstacle, in *Proceeding of the IEEE International Conference on Robotics and Automation*, 1991, pp. 2328-2335.
- [10]. R. Fierro, F. L. Lewis, Control of a nonholonomic mobile robot: backstepping kinematics into dynamic, *Journal of Robotic Systems*, Vol. 14, No. 3, 1997, pp. 149-163.



Photoplethysmography Based Mental Stress Analysis Algorithm and System for Human Wellbeing Life

Jong-Ha Lee

Keimyung University, School of Medicine, Department of Biomedical Engineering, South Korea

Tel.: (82)-53-580-3736, fax: (82)-53-580-3746

E-mail: segeberg@kmu.ac.kr

Received: 13 December 2016 /Accepted: 30 December 2016 /Published: 31 January 2017

Abstract: HRV, physiological indicators, using the PPG data was found to be changed by mental stress. Our results indicate that PPG measurement may be one of the easiest ways to assess the mental stress quantitatively. In a subsequent experiment, it is necessary to find out the relationship between the physiological indicators and various types of psychological stress.

Keywords: PPG, Mobile sensor, Wellness, Mental stress, Big data, u-healthcare.

1. Introduction

In recent modern society, the incidences of depression and other stress-related diseases are increasing. Mental stress acts as a risk factor affecting a variety of other diseases. A high degree of mental stress contributes to coronary heart disease and cardiovascular diseases such as myocardial ischemia. Identification of individual stress level is the basic step for the prevention of stress-related diseases. A number of studies measuring the mental stress by using a biomarker like salivary cortisol and alpha-amylase have been conducted, but these studies are expensive and require specialized knowledge. Thus, obtaining fast results in mental stress quantitative evaluation at a low cost and using a non-invasive method was considered to be an important goal.

PPG is the equipment which measures the amount of peripheral blood flow, depending on the absorption and reflectivity of the blood vessel using infrared rays. Peripheral blood flow changes in accordance with the autonomic nervous system activity which is known as

an indicator of mental stress. Indicators of autonomic nervous system activity are mostly calculated by using the Heart Rate Variability (HRV). In several recent reports, it is reported that HRV in peripheral blood flow and near the heart are the same in physiological function. In HRV measurements, the electrodes typically need to be attached to the chest or abdomen area. On the other hand, PPG minimizes the pressure on the users putting a finger in the device, and it accurately measures the changes in peripheral blood flow. Therefore PPG measurement is non-invasive and the simplest method to measure stress. In addition, it has been suggested that PPG waveform reflects the health condition as indicated by simple and weak signals which is a result of disease or aging. Severe mental stress leads to peripheral vasoconstriction caused by activation of the sympathetic nervous system. As a result, chronic stress may result in the peripheral blood diseases and ischemic cardiovascular diseases. Therefore, the measurement of the stress using PPG may be an important means to predict the state of health of an individual.

2. Body

2.1. Research Plan

We planned a method of measuring the stress level by comparing the before and after results of the experiment. First, we assessed the moods of participants using the Profile of Mood States (POMS) survey prior to the experiment. POMS survey showed five different scales, including unworthiness, anger, anxiety, depression, and vitality. PPG was measured for 3 minutes and 30 seconds while the participants was filling out questionnaires. Right after CWT, PPG was measured by assessing the mood of participants with POMS. The experimental procedure was shown in Fig. 1.

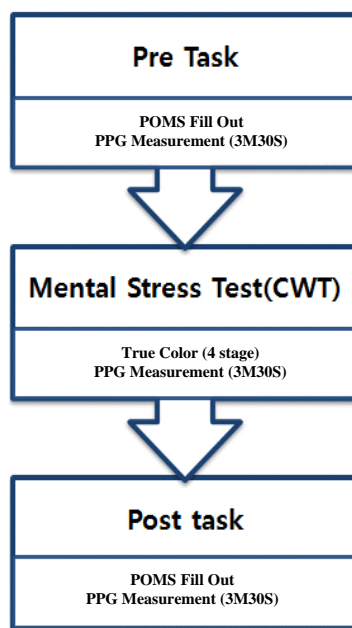


Fig. 1. Experimental Procedure.

2.2. Profile of Mood States (POMS) Survey

We evaluated the subjective mood of the test subject using the Profile of Mood States (POMS) questionnaire to assess the mood of the test subjects. The survey consisted of a total of 45 questions and each question represents the five mood states, such as unworthiness, anger, anxiety, depression, vitality (vigor). The degree of feeling was divided into five levels according to each question.

One of the difficulties in testing the correct correlation between the subjective POMS survey data and objective PPG survey data was the difference between the measured timing. The POMS questionnaire was filled in before and after receiving stress, but the PPG data were measured during the stress test. We could not measure the two types of data at the same time, but it should be measured at the same time in order to overcome these problems.

2.3. Stress Test

Stroop Color-Word Test (CWT) is known to apply stress using the Stroop effect. Stroop effect is a phenomenon that shows a difference in the speed of reading the letters when reading the letters only, and then when the font color doesn't match with the letter. Using this phenomenon, stress was given by an application called 'True color' created by Aurélien Hubert. True color is composed of 4 step game. The first step is to select the word that matches the color and the word expressing that color. The time limit for a question is 5 seconds and the correct answer should be entered within the time. The more correct answers that are entered, the time limit shortens. The score is calculated by the number of correct answers, and the game ends immediately when the answer is wrong. The second step is to test how many correct answers were entered to the given questions within the time limit. The time limit is 30 seconds, and the game method is the same as the first step. However, the game doesn't end even if the answer is wrong, but 1 score will be deducted from the score with every wrong answer. In the game of the third step, the color and the word that describes the given color is different, and the participant needs to find the color that matches with a word from the given examples. In this game, eight kinds of colors are given and the correct answer should be entered within five seconds. Like the first step, the more correct answers that are entered, the time limit decreases, and the game ends immediately with the wrong answer. Finally, four examples of the color and the word describing the given color will be shown in the fourth step. Here, the participant needs to find the one that matches. The time limit is 3 seconds, and the game ends immediately when the answer is wrong.

3. Experiment

3.1. Test Subject

We recruited test subjects prior to experiment. Target subjects were men and women who were in good health (average age 23 years old \pm 2), with no cardiovascular disease, no color blindness, never took medication, not pregnant, and had no experience of CWT. In addition, the experiment was conducted when the test subjects had plenty of rest, consumed no alcohol within the 12 hours' time frame of the experiment, and were not in a state of extreme physical fatigue.

3.2. The Data Measurement

We use the PPG sensor used in Arduino to measure PPG. A schematic diagram of the equipment is shown in Fig. 2(a). The PPG sensor has a photo sensor that receives the light source and the light. The second

segment of the non-dominant hand's index finger is laced over the sensor and wrapped with a strap. A schematic diagram of this wearing method is shown in Fig. 2(b). Data collection was conducted by using the serial communication between Arduino UNO and Desktop Computer, and Matlab was used in this procedure.

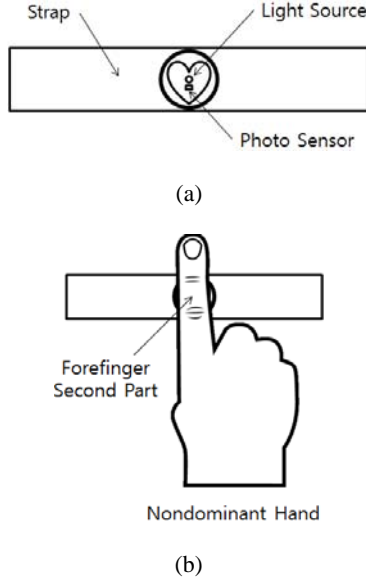


Fig. 2. (a) PPG Sensor equipment schematic diagram, (b) PPG Sensor wearing schematic diagram.

3.3. Data Analysis

PPG data of the test subjects measured by each step were analyzed using the Matlab. After reducing the high frequency noise using a Hamming Window, the Fast Fourier transform (FFT) was conducted. Hamming Window is shown in Equation (1).

$$\text{Haming Window} = 0.54 - 0.46\cos\frac{2\pi n}{N} \quad (1)$$

for $n = 0, 1, 2, \dots, N - 1$

The obtained frequency band is divided into a low frequency band (LF: 0.04 ~ 0.15 Hz) and high frequency band (HF: 0.15 ~ 0.4 Hz). According to several reports, LF is a low-frequency region and reflects the activity of the sympathetic nervous system, and HF is a high frequency region and reflects the activity of the respiratory system and the parasympathetic nervous system. The Heart Rate Variability (HRV) is a measurement the activity of the autonomic nervous system by using the ratio of these two values. HRV is shown in Equation (2).

$$\text{HRV} = \frac{\text{LF}}{\text{HF}} \quad (2)$$

In our data, HRV was reduced when the experimenters conducted the test at the pre-task conditions. And HRV was restored in the post-task

conditions after the stress tests had been completed. Table 1 displays the average of the experimenter frequency data, and the HRV data of each test subject is shown in Fig. 3. The psychological state of the experimenter was changed to positive overall when compared before and after the stress test. The data of the negative items fell sharply. Average psychological state data of the experimenters is shown in Table 2.

In addition, we could observe the changes in heart rate (HR). The HR of all experimenters was increased during the stress test. This was seen as a result of the tension and excitement for the game. HR data for each experimenter is presented in Fig. 4.

Table 1. The average frequency data of the experiment.

	Average	
Unworthiness	16.75	14.41667
Anger	15.5	15.08333
Anxiety	22.08333	17.16667
Depression	21.5	17.08333
Vitality	30.75	29.25

Table 2. Average psychological state data of the experimenters.

	Average		
	LF	HF	HRV
Pre-task	320685.7	268035.1	1.217443
CWT	306024.1	337286.9	1.00752
Post-task	347666.2	360008.7	1.070755

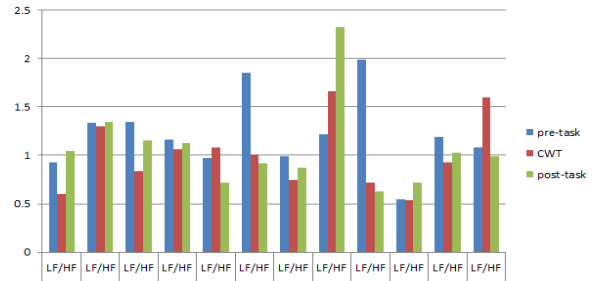


Fig. 3. LF/HF (HRV) data graph by steps of test subjects.

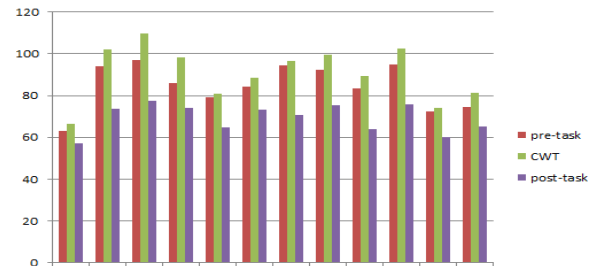


Fig. 4. Graph of heart rate data in steps of each test subjects.

In general, positive emotions (e.g. appreciation) increases both the high-frequency component (HF) and the low frequency components (LF), so there is no changes in LF / HF ratio. On the other hand, negative

emotions (eg. anger, frustration, and sadness) are known to cause no change in the high-frequency component (HF), but clearly increases the low-frequency component (LF). Our test results shows that average HRV of the experimenters decreased while conducting the stress test. It also showed a positive change in the mood state data with the POMS survey. Therefore, we could find the correlation between the autonomic nervous system activity index and the mental stress.

4. Conclusion and Future Research Directions

HRV, physiological indicators, using the PPG data was found to be changed by mental stress. Our results indicate that PPG measurement may be one of the easiest ways to assess the mental stress quantitatively. In a subsequent experiment, it is necessary to find out the relationship between the physiological indicators and various types of psychological stress.

Acknowledgements

The research was supported by the Ministry of Trade, Industry & Energy (MOTIE, Korea) under Industrial Technology Innovation Program, No. 10063553, (Self-directed portable safety kits and application based living environment service system and this work (Grants No. C0395986) was supported by Business for Cooperative R&D between Industry, Academy, and Research Institute funded Korea Small and Medium Business Administration in 2017.

References

- [1]. Sangeeta Bagha, Laxmi Shaw, A Real Time Analysis of PPG Signal for Measurement of SpO₂ and Pulse Rate, *International Journal of Computer Applications* (0975 – 8887), Vol. 36, No. 11, December 2011, pp. 45-50.
- [2]. Mathew Gregoski, Alexey Vertegel, Frank Treiber, Photoplethysmograph (PPG) derived heart rate (HR) acquisition using an Android smart phone, in *Proceedings of the 2nd Conference on Wireless Health (WH '11)*, Article No. 23, 2011.
- [3]. Minakuchi E., *et al.*, Evaluation of mental stress by physiological indices derived from finger plethysmography, *Journal of Physiological Anthropology*, Vol. 32, No. 17, 2013, pp. 1-11.
- [4]. Jason J. Radley, Stress risk factors and stress-related pathology: neuroplasticity, epigenetics and endophenotypes, *Stress (Amsterdam, Netherlands)*, Vol. 14, No. 5, 2011, pp. 481-497.
- [5]. Stansfeld S. A., Shipley M. J., Head J., Fuhrer R., Repeated job strain and the risk of depression: longitudinal analyses from the Whitehall II study, *American Journal of Public Health*, Vol. 102, No. 12, 2012, pp. 2360-2366.
- [6]. Imanishi A., Oyama-Higa M., On the largest Lyapunov exponents of finger plethysmogram and heart rate under anxiety, fear, and relief states, in *Proceedings of the IEEE International Conference on Systems, Man and Cybernetics*, 2007, pp. 3119-3123.
- [7]. Arai S., Ohira K., Tetsutani N., Tobe Y., Oyama-Higa M., Ohta Y., A design of software adaptive to estimated user's mental state using pulse wave analysis, in *Proceedings of the IEEE Ninth International Conference on Networked Sensing Systems (INSS)*, 2012, pp. 1-4.



Published by International Frequency Sensor Association (IFSA) Publishing, S. L., 2017 (<http://www.sensorsportal.com>).



Universal Frequency-to-Digital Converter (UFDC-1)

- 16 measuring modes: frequency, period, its difference and ratio, duty-cycle, duty-off factor, time interval, pulse width and space, phase shift, events counting, rotation speed
- 2 channels
- Programmable accuracy up to 0.001 %
- Wide frequency range: 0.05 Hz ... 7.5 MHz (120 MHz with prescaling)
- Non-redundant conversion time
- RS-232, SPI and I²C interfaces
- Operating temperature range -40 °C ... +85 °C

www.sensorsportal.com
info@sensorsportal.com
SWP, Inc., Canada

Fuzzy System of Diagnosing in Oncology Telemedicine

¹ Oleh BEREZSKY, ¹ Serhiy VERBOVYY, ¹ Lesia DUBCHAK
and ^{2,*} Tamara DATSKO

¹Ternopil National Economic University, Lvivska str., 11, Ternopil, 46020, Ukraine

²I. Ya. Horbachevsky Ternopil State Medical University, Ruska str., 12, Ternopil, 46008, Ukraine

¹ Tel.: +380352475051, fax: +380352475051

² Tel.: +380352524492, fax: +380352524183

E-mail: ob@tneu.edu.ua, datskotv@gmail.com

Received: 20 September 2016 / Accepted: 30 December 2016 / Published: 31 January 2017

Abstract: Breast cancer is the most common cancer among women. Cytological images are used to diagnose the breast cancer. In this thesis the fuzzy system of diagnosing of precancerous and cancerous conditions of the breast is proposed. This system is based on the expert evaluation of cytological images and can be used in modern oncology telemedicine.

Keywords: Telemedicine, Oncology, Diagnose, Breast cancer cytological images, Fuzzy knowledge base, Fuzzy system.

1. Introduction

Telemedicine is a modern branch of IT-based development in the field of medicine that involves using of modern information and telecommunication technologies for remote diagnosis and treatment, in emergency situations as well as for health workers training [1, 3].

According to the National Cancer Registry in 2014 in Ukraine there were 14 908 cases. Moreover, almost 25% of tumors are diagnosed at a late stage, and 40% of women over 40 have never been properly examined [1].

Cytological examination of breasts plays an important role in the diagnosis of breast diseases. It is based on the method of fine needle aspiration biopsy. Fine needle aspiration biopsy, followed by cytology is an integral component of diagnosis of breast diseases in most European countries [2].

The diagnosis based on cytology is subjective because in most cases a doctor carries it out alone.

Thus we need to create an objective evaluation system in order to examine malignancies based on of several experts knowledge in this field. The problem can be solved using fuzzy logic and its future program implementation.

Today fuzzy systems are becoming increasingly popular as a tool of modern information technology, decision support, pattern recognition and medical diagnostics. They are also the basis of fuzzy controllers that can implement software which can be applied in practice.

Fuzzy logic is used in various areas of industrial process control systems or securities trading. Fuzzy logic mechanisms also can be used in medical diagnostic systems modeling [4-5]. Their basis is the expert assessment of input variables and outputs depending on them. Typically, these evaluations are qualitative, not quantitative, which complicates their implementation by standard mathematical methods.

Currently, there are many fuzzy logic conclusion mechanisms, in particular Mamdani and Sugeno mechanisms are the most popular among them.

The development of information technology has left its mark on the development of medicine. Has the opportunity to hold consultations of leading specialists regardless of their location, to monitor the healing process of the patient, to administer surgical operations, to provide psychological help, etc.

2. Experts' Knowledge Basis of Biomedical Image Analysis

Cytological examinations of epithelial cells and structures allow researchers to form suggestions about degrees of epithelial proliferation. The systematization of cytological images with mastitis and fibroadenoma shows the possibility of cytological methods to make a diagnosis [9].

Cytology helps differentiate malignant processes in the following cases: if we find in punctate:

- Ductal cells with nuclear enlargement and prominent nucleoli but they are in large sheets with no single cells;
- Only a few malignant cells are present;
- Malignant cells intermixed with bare bipolar nuclei;
- Comment on presence or absence of ductal-foam cells;
- Atypical ductal epithelial cells: (Paget's disease, invasive carcinoma) [10].

Cytology defines the characteristics of normal cells:

- Often scant cellularity (depends on age, hormonal status);
- Small groups of ductal cells;
- Lobular structures may be seen;
- Myoepithelial cells in cell groups (as elongated nuclei) and in the background (ovoid nuclei stripped of the cytoplasm);
- Adipose tissue and stroma.

Normal cells: a few small cohesive groups of ductal cells at the most; different from adequacy criteria for FNA (Fig.1).

Breast Cyst is shown on Fig. 2.

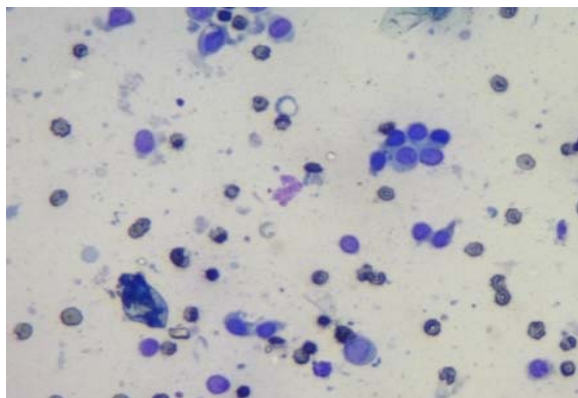


Fig. 1. Normal apocrine cells with abundant granular cytoplasm and prominent central nucleoli.

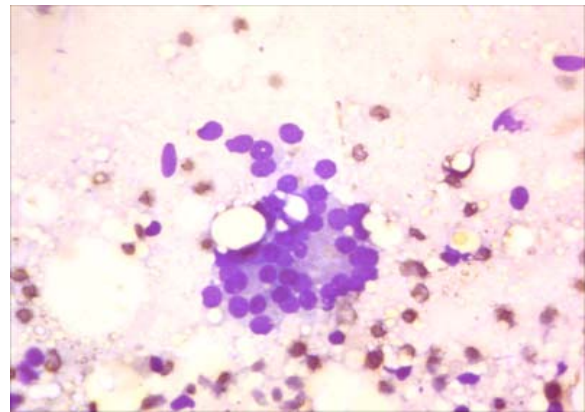


Fig. 2. Breast Cyst.

Cytological structure of the Breast Cyst:

- Background of amorphous material;
- Degenerate cells and debris;
- Foamy macrophages;
- Ductal epithelial cells, often apocrine and balling-up;
- Myoepithelial cells may not be seen (do not overcall aspirate as malignant).

Cytological structure of Fibrocystic change:

- Variable numbers of apocrine cells and foam cells;
- Variable fat and stroma;
- Low to moderate cellularity;
- Proteinaceous background;
- Cohesive sheets of ductal cells in a honeycomb pattern;
- Bare bipolar nuclei dispersed in the background and within or attached to sheets of epithelial cells.

Cytology defines the characteristics of Fibroadenoma is shown on Fig. 3.

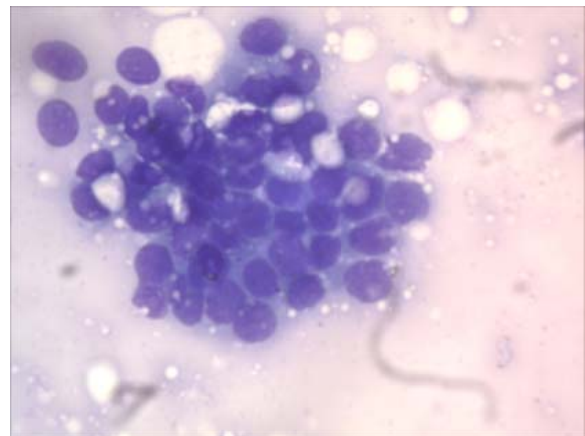


Fig. 3. Fibroadenoma.

Basic structural elements of Fibroadenoma:

- Moderate to high cellularity;
- Tightly cohesive branching antler-horn or finger-like projections of epithelial cells;

- Stromal fragments (metachromatic fibrillary matrix material);
- Both ductal and stromal components need to be diagnostic;
- Numerous bare bipolar nuclei, bordering and within epithelial clusters;
- May see few foam cells or apocrine cells;
- Often mild nuclear atypia with prominent nucleoli, particularly in younger patients.

Invasive ductal carcinoma is shown on Fig. 4.

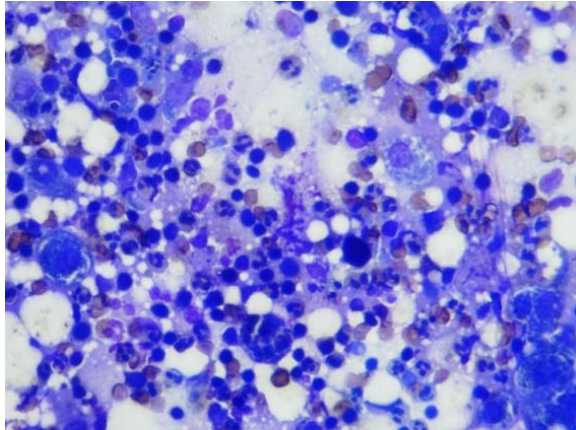


Fig. 4. Invasive ductal carcinoma.

Basic structural elements of invasive ductal carcinoma, of no special type:

- Usually very cellular;
- Disorganised, loosely cohesive groups;
- Single, polygonal, plasmacytoid epithelial cells (which can look deceptively bland);
- Absence of bare bipolar nuclei;
- Cellular and nuclear pleomorphism (2-4x RBC);
- Nuclear border irregularity;
- Hyperchromasia;
- Nucleoli;
- There may be mucin vacuole / targetoid inclusion within the cytoplasm;
- Mitoses.

On the basis of experimental studies we have provided quantitative microscopic signs of breast tissue [11]. For example there is a comparison of mastitis and cystic papillary cancer.

3. Modern Telemedicine

According to the order of the Ministry of Health of Ukraine №681 the main goal of telemedicine is to improve health of the population by ensuring equal access to high quality health service.

The main objectives of telemedicine are as follows [3]:

- To ensure medical care of a patient, when the distance is a critical factor of maintaining;
- To protect medical confidentiality and privacy, integrity, medical information about the patient's health status;

- To create unified medical space;
- To promote quality care and optimize the processes of the organization and administration of health;
- To develop systematic approaches to implementation and development of telemedicine in the health system.

The network is closely connected with the concept of telemedicine, that is, it's the organization form of medical aid for the population with the help of telemedicine.

The telemedicine network includes the following tasks:

- To organize and systematize the process of medical care providing with telemedicine;
- To ensure the compatibility of information and data for medical care with telemedicine;
- To ensure the use of health information standards in the process of medical care providing with telemedicine;
- To supervise the quality of medical care with telemedicine.

In this work we also discuss telemetry considering it as the combination of all the technologies created for remote measurement, collection and transmission of information about performance (e.g., physiological parameters of the patient's body [3]).

Telemedicine may also facilitate closer communication between doctors and patients, as it provides the opportunity to study specific cases, the results of which can finally be used to treat future patients.

Teleconsultations are particularly important in diagnosing difficult diseases. A necessary condition of teleconsultation is to provide a full-fledged source of information for decision-making on the diagnosis. In particular, telemedicine can speed up, increase the likelihood of correct diagnosis and choose the right treatment of cancer. It is very important currently, because the cancer is growing steadily every year.

According to studies conducted in [3], the growth rate of the telemedicine market is growing by 18-30 % per year.

The total annual income of the United States in 2013 amounted to \$ 9.6 billion and projected to increase to \$ 38.5 billion in revenue by 2018.

37 % of employers in the world have already offered telemedicine service for their employees.

According to the survey conducted by Intel, 72 % of consumers noted that they were ready to visit doctors and use telemedicine for urgent conditions. Three well-known alliances members (Connected Care, Anthem, Teladoc and MD Live) have reported satisfaction with the telemedicine patients more than 95 % [3].

Consumers of health service demand and need convenient care and telemedicine can offer it.

Let's discuss the history of telemedicine. It was founded during the second half of the 19th century, and one of the first published references were at the beginning of the 20th century, when electrocardiogram data were transmitted over telephone cables. The

beginning of telemedicine in its modern form was initiated in 1960-ies of the last century, mostly due to the development of military and space technology and the efforts of several specialists who used available equipment on the market.

The beginning of the development of telemedicine in Ukraine is associated with the 1940s, namely the studies that were conducted in the framework of space projects. Thereafter, the development was carried out mainly by ECG transmission via different communication channels and deathculture.

In 1994 the negotiations were held with international experts about telemedicine implementation in Ukraine and then the first telemedicine consultation was presented. Since the late 1990-ies a national network of tele-ECG has been developed. In 2000 a telemedicine centre (Donetsk Research Institute of Traumatology and Orthopedics) was the first created in Ukraine). Later, the telemedicine began to be implemented in clinical work in several areas of the country (teledramaturgia and alertpedia, teledermatology, teleradiology).

Regional telemedical networks have been functioning since 2002. In 2006 the national public organization (the Association of development of Ukrainian telemedicine and e-health) was founded [3].

Currently there is a rapid development and rapid implementation of telemedicine in all countries of the world.

The telemedicine network includes the following tasks:

- To organize and systematize the process of medical care with the help of telemedicine;
- To ensure the compatibility of information and data in medical care using telemedicine;
- To ensure the use of health information standards in the process of medical care with the help of telemedicine;
- To supervise the quality of the medical care.

In the process of telemedicine the consultation involves:

- Patient,
- His/her doctor,
- Medical personnel (doctors) who provide advice (hereinafter - the consultant),
- The telemedicine staff.

Despite the considerable spread of telemedicine in the world and its development in Ukraine, it can be identified by the following main challenges during the implementation. Primarily important thing is also if telemedicine is legal according to the laws. However, nowadays there are some doubts about its legal regulation in different countries of the world. In Ukraine, the introduction of telemedicine should follow the order of the MOH of Ukraine №681 and DSTU of Ukraine concerning protection of information.

The next problem concerns the hardware and software of telemedicine. In particular, it is necessary to consider their value, that is, they must be economically beneficial not only for commercial but also for state medical institutions.

In addition, software and hardware must have a simple interface for users, in particular for doctors and patients. It should be noted that hardware and software is chosen depending on the task which can be solved with telemedicine (e.g., the need for imaging in Oncology or video calling when online transactions are conducted, etc.). These characteristics must be considered in case of developing of both new and existing hardware and software.

Many scientific works are devoted to information protection of telemedicine. In particular, in order to protect personal data of a patient it is necessary to apply different cryptographic algorithms and to confirm the diagnosis or transmitted information. The physician is requested to apply an electronic digital signature. Some scientists use watermarks to protect images. However, it should be noted that security policy must be developed in each case of telemedicine introduction [4-6].

One of the last studied problems is the choice of experts for consultation. In some papers it is noted that the medical consultant should be highly skilled and experienced in the field of medicine. However, expert opinion is always subjective and sometimes the diagnosis can be false.

This problem can be solved with the help of fuzzy logic, taking into account the entire knowledge base of an expert. Such fuzzy system can perform diagnosis in real time, eliminating all disadvantages of the classical method of diagnosis.

Finally, in order to implement telemedicine the following tasks should be solved:

1. Determining the course of medical consultations in telemedicine applications;
2. The choice of legal base;
3. Development of its security policies with the definition of telemedicine participants, distribution of their rights and of appropriate cryptographic protection of information;
4. The choice or the development of new hardware and software taking into account the above defined characteristics;
5. Development of the system of selection of experts;
6. Development of a fuzzy diagnosis system;
7. Testing and verification of the established telemedicine.

Furthermore, to develop telemedicine one should consider all the above-mentioned problems and to choose the optimal ways of their solution.

4. Structure of the Fuzzy System

The main objective of creating a fuzzy system is the definition of fuzzy sets and fuzzy rules that require deep expertise in a particular subject area. The aim of this research is to develop a fuzzy system for the diagnosis of dysplastic processes in the breast based on the morphometric parameters of cytological images.

In order to develop the fuzzy system it is better to choose the Mamdani fuzzy conclusion algorithm, which is based on the “if-then” rules.

The Mamdani mechanism is based on “min-max” composition. The first phase of the fuzzy conclusion algorithm determines the functions of each variable and builds a rule set. The next one is the relevant functions “cut-off” of each rule by a “minimum” operation. On the third phase of the Mamdani algorithm the “uniting” of all “cut off” functions is used with the help of “maximum” operation. The defuzzification, that brings the fuzzy output to clarity is usually implemented by finding the gravity center of the final received figures.

Let’s see the examples of the rules of the proposed fuzzy knowledge’s base:

If a small number of hypochromic monomorphic cells and narrow rim intensely colored cytoplasm and rounded hyperchromic nuclei, then we talk about a fibrous nonproliferative breast disease (70 %).

If papillary structures are formed, and we notice intense expression of the nucleus, and narrow rim intensely colored cytoplasm, and rounded hyperchromatic nuclei then we talk about a fibroadenoma (80 %) [5]. The proposed fuzzy system of diagnosing breast cancers includes nine inputs and one output (Fig. 5).

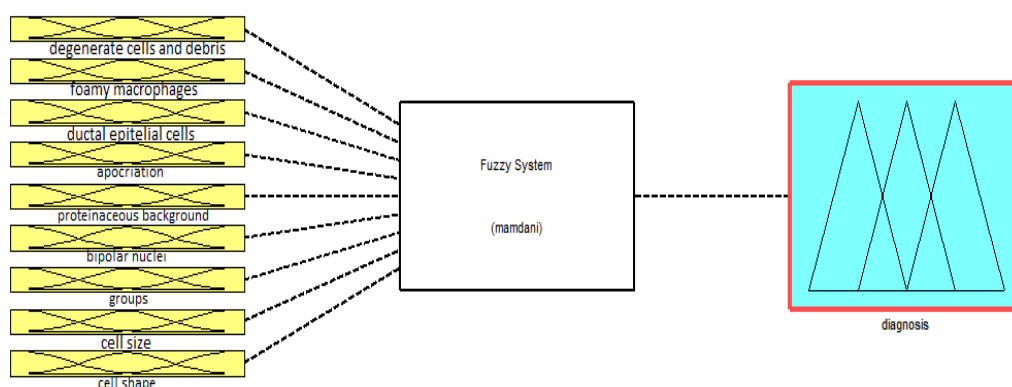


Fig. 5. The fuzzy system of diagnosing breast cancers.

Due to the information of part I of this article, the inputs of proposed fuzzy system are:

- Degenerate cells and debris;
- Foamy macrophages;
- Ductal epithelial cells;
- Apocriation;
- Proteinaceous background;
- Bipolar nuclei;
- Groups;
- Cell size;
- Cell shape.

The output “diagnosis” of fuzzy system describes the malignant process in breast:

- Breast cyst;
- Fibrocystic change;
- Fibroadenoma;
- Invasive ductal carcinoma.

Most of these inputs are described by quality descriptions. For example, the first input — “degenerate cells and debris” is described by “low”, “medium” and “high” fuzzy variables, that show these cells presence in the cytology images. Analogically, the inputs of “foamy macrophages”, “ductal epithelial cells”, “apocriation”, “proteinaceous background” and “bipolar nuclei” can be described by the same variables. The member functions of these inputs can be described by bell function as shown in Fig. 6.

However, the input “groups” can be described by the variables “clibriform”, “tubular”, “finger-like” and “cup-shaped”. The member functions of this input are shown in Fig. 7.

The “cell size” and “cell shape” are described by quantitative descriptions, which are shown in Table 1. The member functions of those inputs are shown in Fig. 8 and Fig. 9.

Table 1. Comparative characteristics of papillary cancer and cystic mastitis.

	Papillary cancer	Cystic disease
Nuclear area	13610.87392	5581.726
Cytoplasm area	28833.08333	114426.8
Nuclear-cytoplasmic ratio	0.472057524	0.048779884

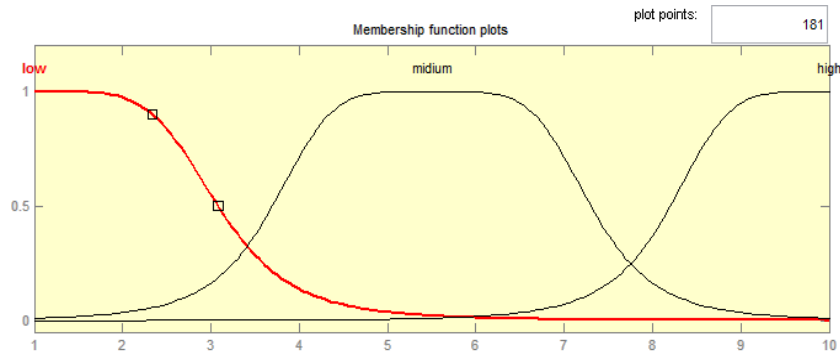


Fig. 6. The member functions of input “degenerate cells and debris”.

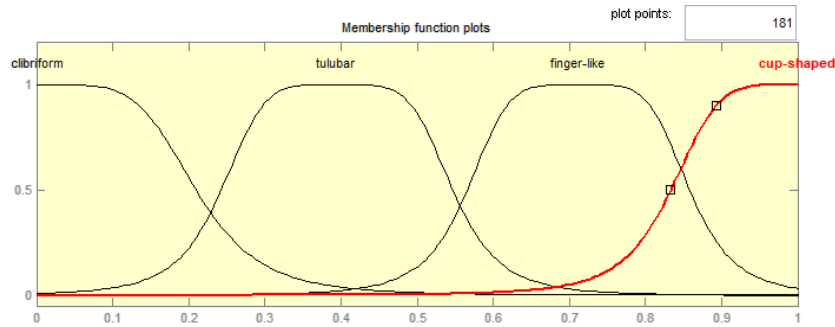


Fig. 7. The member functions of input “groups”.

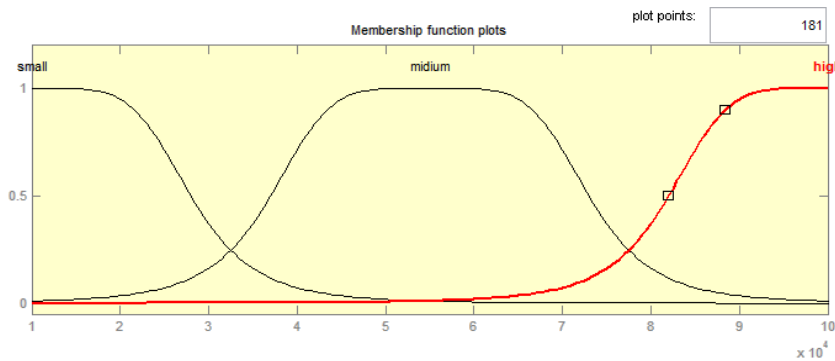


Fig. 8. The member functions of input “cell size”.

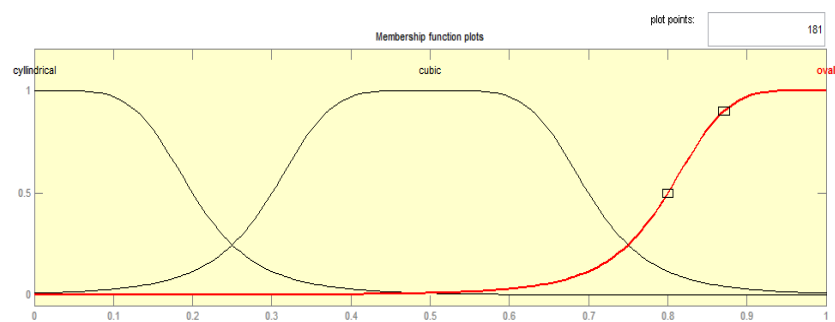


Fig. 9. The member functions of input “cell shape”.

5. Conclusions

The proposed fuzzy system can be realized using such tools as Fuzzy Logic Toolbox of Matlab [8] with the further construction of fuzzy controller in the

Simulink environment. This fuzzy controller can be used in medical practice for diagnosing of precancerous and cancerous processes of breasts obtaining exact results [12].

Acknowledgements


This proposed research was developed during the work on the state budget project “Hybrid intelligent information technology diagnosing precancerous breast cancer based on image analysis” (state registration number 1016U002500).

References

- [1]. 14.908 cases of breast cancer [electronic resource] – Access mode: http://galinfo.com.ua/articles/torik_v_ukraini_zareiestrovano_14_908_vypadkiv_zahvoryuvannya_na_rak_molochnoi_zalozy_197568.html (in Ukrainian).
- [2]. Cytological research of the breast [electronic resource] Access mode: <http://diagnoz.net.ua/xvorobu/18012-citologichne-doslidzhennya-molochnih-zaloz.html> (in Ukrainian).
- [3]. Telemedicine: opportunities and developments in Member States: report on the second global survey on eHealth 2009 [electronic resource], http://apps.who.int/iris/bitstream/10665/44497/4/9789244564141_rus.pdf (in Russian).
- [4]. A. K. Shaikhanova, *et al.*, Fuzzy system of access distribution within a computer network, *Journal of Theoretical and Applied Information Technology*, Vol.80, No.1, 2015, pp. 105-113.
- [5]. L. Dubchak, *et al.*, Fuzzy data processing method, in *Proceedings of the IEEE 7th International Conference on Intelligent Data Acquisition and Advanced Computing Systems (IDAACS' 13)*, Berlin, Germany, Vol.01,12-14 September 2013, pp. 373-375.
- [6]. M. Aleksander, *et al.*, Implementation Technology Software-defined networking in Wireless Sensor Networks, in *Proceedings of the IEEE 8th International Conference on Intelligent Data Acquisition and Advanced Computing Systems (IDAACS' 15)*, Warsaw, Poland, 24-26 September 2015, pp. 448-453.
- [7]. Dubchak L.O., Fuzzy system of information security in the telemedicine, *Information Processing Systems*, Vol. 8, No. 133, 2015, pp. 97-101.
- [8]. Ross T. J., Fuzzy Logic with Engineering Applications, *McGraw-Hill Inc.*, (USA), 1995.
- [9]. Oleh Berezsky, Grygory Melnyk, Tamara Datsko, Sergiy Verbovy, An intelligent system for cytological and histological image analysis, in *Proceedings of the XIIIth International Conference on the Experience of Designing and Application of CAD Systems in Microelectronics (CADSM'15)*, Polyana-Svalyava (Zakarpattia), Ukraine, 24-27 February 2015, pp. 28-31.
- [10]. Hunt C. M., Ellis I. O., Elston C. W., Locker A., Pearson D., Blamey R. W., Cytological grading of breast carcinoma — A feasible proposition? *Cytopathology*, Vol. 1, 1990, pp. 287-295.
- [11]. Berezsky O. M., *et al.*, Automated system of biomedical image analysis, in *Proceedings of the Xth International Conference Modern Problems of Radio Engineering, Telecommunication and Computer science (TCSET'10)*, Slavske, Ukraine, 23-27 February 2010, pp. 143-143.
- [12]. Oleh Berezsky, Serhiy Verbovy, Tamara Datsko, The intelligent system for diagnosing breast cancers based on image analysis, in *Proceedings of the Information Technologies in Innovation Business (ITIB)*, Kharkiv, Ukraine, 7-9 October, 2015, pp. 27-30.



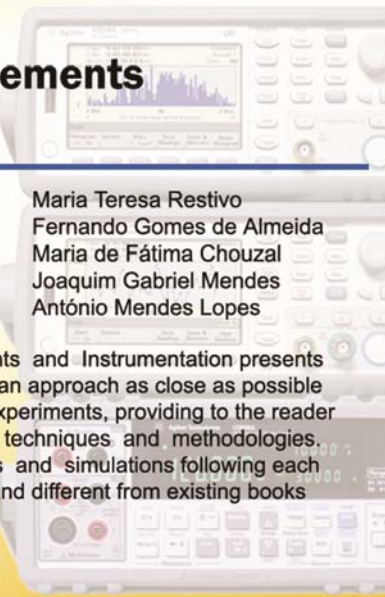
Published by International Frequency Sensor Association (IFSA) Publishing, S. L., 2017 (<http://www.sensorsportal.com>).




Handbook of Laboratory Measurements and Instrumentation

Maria Teresa Restivo
Fernando Gomes de Almeida
Maria de Fátima Chouzal
Joaquim Gabriel Mendes
António Mendes Lopes

The Handbook of Laboratory Measurements and Instrumentation presents experimental and laboratory activities with an approach as close as possible to reality, even offering remote access to experiments, providing to the reader an excellent tool for learning laboratory techniques and methodologies. Book includes dozens videos, animations and simulations following each of chapters. It makes the title very valued and different from existing books on measurements and instrumentation.





International Frequency Sensor Association Publishing

Order online:
http://www.sensorsportal.com/HTML/BOOKSTORE/Handbook_of_Measurements.htm

Non-rigid Point Matching using Topology Preserving Constraints for Medical Computer Vision

Jong-Ha Lee

Keimyung University, School of Medicine, South Korea
Tel.: (82)-53-580-3736, fax: (82)-53-580-3746
E-mail: segeberg@kmu.ac.kr

Received: 22 November 2016 /Accepted: 30 December 2016 /Published: 31 January 2017

Abstract: This work presents a novel algorithm of finding correspondence using a relaxation labeling. For the variance experiments, the variance of all algorithms except the proposed algorithm is large. The largest variance of the proposed algorithm is +0.01 in the 0.08 deformation test of a character. Overall, the proposed algorithm outperforms compared to the rest of algorithms. Except the proposed algorithm, matching with neighborhood algorithm shows the best performance except an outlier to data ratio in a character test. The proposed algorithm shows the best performance as well as an outlier to data ratio in a character test.

Keywords: Non-rigid point matching, Image registration, Correspondence problem.

1. Introduction

The point matching is widely used in computer vision and pattern recognition since point representations are generally easy to extract. Point matching can be categorized as rigid and non-rigid based on the deformation of captured images [1-2]. Rigid point matching is relatively easy with a small number of transformation parameters. Non-rigid point matching is more complicated than rigid matching. There are two unknown parameters: correspondence and transformation. Most approaches to non-rigid point matching use an iterated estimation framework [3]. Iterated Closest Point (ICP) algorithm is the most well-known heuristic approach algorithm. It utilizes the relationship to assign the correspondence with binary values 0 and 1. However this assumption is no longer valid in the case of non-rigid transformations especially when the deformation is large. Thin Plate Spline Robust Point Matching (TPS-RPM) algorithm is EM-like algorithm to jointly solve for the feature correspondences as well as the geometric transformations [4]. The cost function that is being

minimized is the sum of Euclidean distances between points [5-6]. The soft-assign and the deterministic annealing technique are used to search for an optimal solution. The algorithm is robust compare to the ICP in the non-rigid point matching problem, but the joint estimation of correspondences and transformation leads to a high complexity and calculation time. The searching time is approximately 3 minutes for 100 points. In addition, the distances make sense only when there is at least rough alignment of shape. Under large deformation or rotation, the algorithm is easily diverged. Recently, Shape Context algorithm is proposed. It is an object recognizer based on shape. For each point, the distribution of the length and the orientation for all lines is estimated through histogram [7]. This distribution is used as the shape context for the points. The correspondences can be decided by comparing each point's attributes in one set with the attributes in the other. Since attributes are compared, the search for correspondence can be conducted much more easily compared to ICP and TPS-RPM. The searching time is under 0.01 s for 100 points. However, original shape context is not rotation-invariant and the

algorithm's ability to handle complex patterns and large deformation is not higher than TPS-RPM [8]. In addition, one point can be matched to two points which is far apart each other. Robust Point Matching by Preserving Local Neighborhood Structures algorithm introduces the notion of a neighborhood structure for the general point matching problem. Although the absolute distance between two points may change significantly under non-rigid deformation, the neighborhood structure of a point is generally well preserved due to physical constraints [9]. The author formulates an optimization problem to preserve local neighborhood structures. The perforation of an algorithm is higher than ICP, TPS-RPM, and shape context under various deformation and noise level. But under high occlusion and outlier rate, error is even higher than TPS-RPM. The searching time is under 0.01 s for 100 points.

This work presents a novel algorithm of finding correspondence using a relaxation labeling. This is done by means of a weighed graph matching algorithm. We observed that neighbors defined in the previous work keeps the structure more firmly if the distance between a point and a neighborhood becomes closer. This strength of relaxation becomes loose if a point and a neighborhood are far apart. We call these neighbors as adjacent points. To find the amount of strength between a point and an adjacent point, we propose a distance descriptor. Consider the set of vectors originating from a point to all adjacent points. For a point, we compute distance using bins that are uniform in log space making the descriptor more sensitive to positions of nearby adjacent points than to those of points far apart. The relaxation labeling combined with a strength coefficient is proposed to search the optimized correspondence. The searching time is under 0.01 s for 100 points. A new class of matching algorithm is proved to be stable and robust under all deformation, noise, and occlusion.

2. Problem Formulation

Let $S = \{s_1, s_2, \dots, s_M, nil\}$ be a set of control points in a model image and $T = \{t_1, t_2, \dots, t_K, nil\}$ be a set of control points in a target image. A model image S is composed of M points and a target image T is composed of K points. The dummy point nil is introduced for the outliers. Due to occlusion, number of M is not necessarily equal to K . For a given point $m \in S$, one can select an adjacent point set A^m , $A^m = \{a_1^m, a_2^m, \dots, a_l^m\}$. Similarly, for a point $k \in T$, an adjacent point set is A^k , $A^k = \{a_1^k, a_2^k, \dots, a_j^k\}$. The adjacent relationship is symmetric and it means if $i \in A^m$, then $m \in A^i$. A match between S and T is $f: S \Leftrightarrow T$

and common points match one to one and several points can be matched with the dummy point nil . Given two points $m \in S$ and $k \in T$ from two images, the optimal match f is

$$f = \arg \max C(S, T, f), \quad (1)$$

where

$$C(S, T, f) = \sum_{m=1}^M \sum_{i=1}^I \delta(f(m), f(i)) + \sum_{k=1}^K \sum_{j=1}^J \delta(f^{-1}(n), f^{-1}(j)) \quad (2)$$

$$\delta(i, j) = \begin{cases} 1 & j \in A^i \\ 0 & j \notin A^i \end{cases} \quad (3)$$

The optimal solution maximizes the number of matched edges of two graphs. If m in a model image is matched to point k in a target image, then the matching probability $P_{mk} = 1$, otherwise, $P_{mk} = 0$. Matrix P satisfies the following normalization conditions.

$$\sum_{k=1}^{K+1} P_{mk} = 1 \text{ for } m = 1, 2, \dots, M, \quad (4)$$

$$\sum_{m=1}^{M+1} P_{mk} = 1 \text{ for } k = 1, 2, \dots, K \quad (5)$$

with $P_{mk} \in [0, 1]$.

Using matrix P , the object function (2) can be written as below.

$$C(S, T, P) = 2 \sum_{m=1}^M \sum_{i=1}^I \sum_{k=1}^K \sum_{j=1}^J P_{mk} P_{ij} \quad (6)$$

3. Point Correspondence Using Relaxation Labeling

We use relaxation labeling process to solve the optimization problem. In this section, we show how the relaxation labeling theory is applied to the point matching problem. It is widely known that the relaxation labeling process is greatly affected by the choice of the compatibility coefficient. Thus, compatibility coefficient for preserving physical constrains is also investigated.

3.1. Initialization

Generally, a relaxation labeling process finds a local maximum and the convergence can not always be guaranteed. Therefore, good initialization is very

important for best matching result. We, therefore use shape context distance to initialize the matching probability matrix P . The shape context is a histogram which describes the relative position of the remaining points. Consider a point s in a model image. A point is selected as centers of K log-polar bin and counting points in each bin, providing a description of the entire shape relative to the center. The shape context of a point m is $h_m(d)$, $d=1, \dots, D$. Let $C_{mk} = (m, k)$ denote the cost of matching two points m and k . As shape contexts are distributions represented as histograms, it is natural to use the χ^2 test statistic as follows,

$$C_{mk} \equiv C(m, k) = \frac{1}{2} \sum_{d=1}^D \frac{[h_m(d) - h_k(d)]^2}{h_m(d) + h_k(d)} \quad (7)$$

Taking cost C_{mk} as the energy of the state that points m and k are matched, Gibbs distribution is used to relate the energy of a state to its probability as follows,

$$P_{mk} \propto e^{-C_{mk}/T_{init}} \quad (8)$$

3.2. Relaxation Labeling

After the initial probability assignment, the relaxation labeling process updates the probability of each label iteratively. In a traditional relaxation labeling process, object refers to an entity whose characteristics are under investigation in the process and a label is the description of a characteristic that belongs to an object. In our problem, an object is a control point set S and T and a label is a possible matching probability P . Initially in the algorithm, each object is assigned with a set of labels based on the shape context distance. The purpose of the subsequent process is to assign one label to each object that maximize $C(S, T, P)$ under the relaxed condition as $P_{mk} \in [0, 1]$. It is supposed that labels do not occur independently on each other. The ambiguity reduction process is accomplished iteratively by requiring the relationship adjacent objects' labels to the contextual constraints. To update P , the compatibility coefficient is necessary. In this original work, the compatibility coefficient is defined as the $\{0, 1\}$ binary value. As a key contribution, we propose a novel compatibility coefficient to relax this binary value into $[0, 1]$ continuous value. The compatibility coefficient quantifies the degree of agreement between the hypothesis that m matches k and i among A^m matches j among A^k . We measure the consistency between (m, i) and (k, j) by means of the compatibility coefficient. High values correspond to

compatibility and low values correspond to incompatibility. From the knowledge of the deformation dynamics, we know the points and its adjacent points' distance before non-rigid deformation cannot be very different the distance after non-rigid deformation. This occurs stronger if the original distance between points is closer. Conversely, this strength of relationship becomes less if the points are originally far apart. It means the shorter the edge of m and i , the higher the probability to match with the edge of k and j . This is because the points tend to preserve the rough structure of the shape.

To make the strength between points, we use five bins that are uniform in log space making more sensitive to distances of nearby points than to those of points farther away. This structure based distance is defined as 0 in the origin and incremented by 1 toward outer bins. The set of vectors from originating from a point m to its A^m adjacent points are defined as the a distance set $D(m) = \{d_1(m), d_2(m), \dots, d_L(m)\}$. This choice corresponds to a linearly increasing positional uncertainty with distance from the origin. This idea is illustrated in Fig. 1.

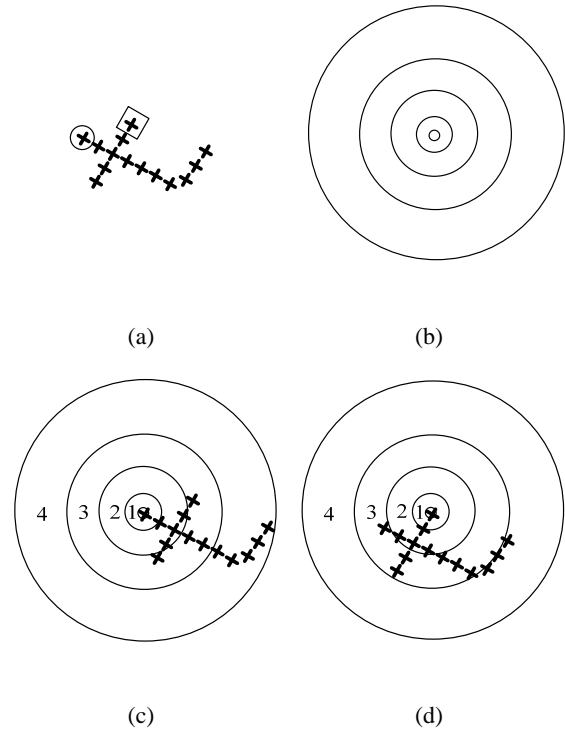


Fig. 1. Structure based distance computation. (a) Sample control points from the shape “t”; (b) Diagram of log bins used in computing the distance. We use five bins, meaning the distance 1 to 4 from the origin. (c) and (d): Example structure based distance marked by O and Y.

Referring to Fig. 2, the compatibility coefficient relating the adjacent distance is

$$\alpha(m, i; k, j) = (1 - \frac{d_i(m)}{\max(d_i(m))}) \quad (9)$$

Clearly, $\alpha(m, i; k, j)$ range from 0 to 1. The support for label p_{mk} in the n th iteration is given by

$$\begin{aligned} q_{mk}^n &= \sum_{i=1}^I \sum_{j=1}^J \alpha(m, i; k, j) p_{ij}^n \\ &= \sum_{i=1}^I \sum_{j=1}^J (1 - \frac{d_i(m)}{\max(d_i(m))}) p_{ij}^n \end{aligned} \quad (10)$$

Note that we use p_{ij}^n to weight $\alpha(m, i; k, j)$ because the support also depends on the likelihood of neighboring matching probability. Finally, p_{mk}^n is updated according to

$$p_{mk}^{n+1} = \frac{p_{mk}^n q_{mk}^n}{\sum_{j=1}^J p_{mj}^n q_{mj}^n} \quad (11)$$

The iterative process can be summarized as follows. If a label, matching probability between points m and k , has relatively more support from adjacent points, its chance of being matched is increasing, i.e., its matching probability is increased. The probability is decreasing if the label is relatively less support. After predefined iteration, the estimated of probability is assigned to a point unless 0 and the probability less than 0.95 are labeled as an outlier. Finally, given a set of correspondences between points on model image and target image, the transformation is estimated using thin plate spline (TPS).

3.3. Adjacent Point Definition

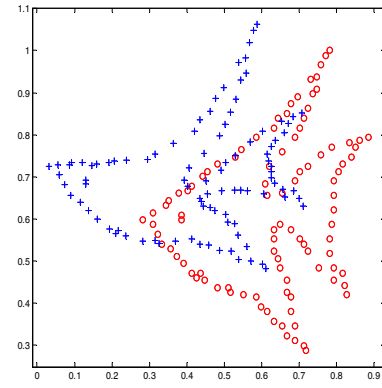
Defining adjacent point properly is very important to maximize the matching performance and reduce the time complexity. In this paper, we define an adjacent point searching boundary. Consider totally M points of a graph are fully connected. The length of an edge is d_e and the number of edges is $M(M-1)/2$. The searching boundary of adjacent point is the circle with a radius as an average length of total edges:

$$\frac{\sum_{e=1}^{M(M-1)/2} d_e}{M(M-1)/2} \quad (12)$$

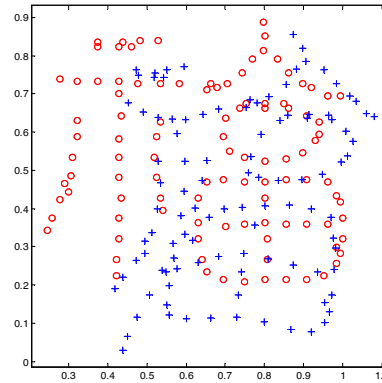
If a point i is reside within the circle with the center of a point m , it is considered as an adjacent point of m . From this definition, we can assign more edges to the crowded point's area and fewer edges to the sparse point's area.

4. Experiments Result

We have tested out algorithm on the same synthesized data as in [10]. There are three sets of data designed to measure the robustness of an algorithm under deformation, noise, and outliers. Two shapes, a fish and a character are generated, and 100 samples are generated for each degradation level. We then run our algorithm to find the correspondence between these two sets of points. The performance is compared with RPM, shape context, and the matching with neighborhood algorithm. Fig. 2 shows one example of template point sets and deformed target sets of a fish and a character.



(a)



(b)

Fig. 2. The model point sets (O) and the target point sets (+) of a fish and a character.

For the variance experiments, the variance of all algorithms except the proposed algorithm is large. The largest variance of the proposed algorithm is +0.01 in the 0.08 deformation test of a character. Overall, the proposed algorithm outperforms compared to the rest of algorithms. Except the proposed algorithm, matching with neighborhood algorithm shows the best performance except an outlier to data ratio in a character test. The proposed algorithm shows the best performance as well as an outlier to data ratio in a character test.

Acknowledgements

The research was supported by the Ministry of Trade, Industry & Energy (MOTIE, Korea) under Industrial Technology Innovation Program, No. 10063553, (Self-directed portable safety kits and application based living environment service system and this work (Grants No. C0395986) was supported by Business for Cooperative R&D between Industry, Academy, and Research Institute funded Korea Small and Medium Business Administration in 2017.

References

- [1]. Q. X. Wu, D. Pairman, A Relaxation Labeling Technique for Computing Sea Surface Velocities from Sea Surface Temperature, *IEEE Transactions Geoscience and Remote Sensing*, Vol. 33, Issue 1, January 1995, pp. 216-220.
- [2]. Y. Zheng, D. Doermann, Robust Point Matching for Nonrigid Shapes by Preserving Local Neighborhood Structures, *IEEE Transactions Pattern Analysis and Machine Intelligence*, Vol. 28, Issue 4, April 2006, pp. 643-649.
- [3]. H. Chui, A. Rangarajan, A New Point Matching Algorithm for Non-Rigid Registration, *Computer Vision and Image Understanding*, Vol. 89, Issue 23, 2003, pp. 114-141.
- [4]. S. Belongie, J. Malik, J. Puzicha, Shape Matching and Object Recognition Using Shape Contexts, *IEEE Transactions Pattern Analysis and Machine Intelligence*, Vol. 24, Issue 4, April 2002, pp. 509-522.
- [5]. A. Rosenfeld, R. A. Hummel, S. W. Zucker, Scene Labeling by Relaxation Operations, *IEEE Transactions System, Man, and Cybernetics*, Vol. SMC-6, Issue 6, 1976, pp. 420-433.
- [6]. M. Pelillo, The Dynamics of Nonlinear Relaxation Labeling Processes, *J. Mathematical Imaging and Vision*, Vol. 7, Issue 4, 1997, pp. 309-323.
- [7]. R. A. Hummel, S. W. Zucker, On the Foundations of Relaxation Labeling Processes, *IEEE Transactions Pattern Analysis and Machine Intelligence*, Vol. PAMI-5, Issue 3, 1983, pp. 267-287.
- [8]. W. J. Christmas, J. Kittler, M. Petrou, Structural Matching in Computer Vision Using Probabilistic Relaxation, *IEEE Transactions Pattern Analysis and Machine Intelligence*, Vol. 17, Issue 8, August 1995, pp. 749-764.
- [9]. S. Peleg, A. Rosenfeld, Determining Compatibility Coefficients for Curve Enhancement Relaxation Processes, *IEEE Transactions System, Man, and Cybernetics*, Vol. 8, Issue 7, 1978, pp. 548-555.
- [10]. M. Pelillo, M. Refice, Learning Compatibility Coefficients for Relaxation Labeling Processes, *IEEE Transactions Pattern Analysis and Machine Intelligence*, Vol. 16, Issue 9, September 1994, pp. 933-945.



Published by International Frequency Sensor Association (IFSA) Publishing, S. L., 2017
(<http://www.sensorsportal.com>).

International Frequency Sensor Association (IFSA) Publishing

Formats: printable pdf (Acrobat) and print (hardcover), 208 pages

ISBN: 978-84-608-2320-9,
e-ISBN: 978-84-608-2319-3

Sensors & Signals

Sergey Y. Yurish, Amin Daneshmand Malayeri, *Editors*

Sensors & Signals is the first book from the Book Series of the same name published by IFSA Publishing. The book contains eight chapters written by authors from universities and research centers from 12 countries: Cuba, Czech Republic, Egypt, Malaysia, Morocco, Portugal, Serbia, South Korea, Spain and Turkey. The coverage includes most recent developments in:

- Virtual instrumentation for analysis of ultrasonic signals;
- Humidity sensors (materials and sensor preparation and characteristics);
- Fault tolerance and fault management issues in Wireless Sensor Networks;
- Localization of target nodes in a 3-D Wireless Sensor Network;
- Opto-elastography imaging technique for tumor localization and characterization;
- Nuclear and geophysical sensors for landmines detection;
- Optimal color space for human skin detection at image recognition;
- Design of narrowband substrate integrated waveguide bandpass filters.

Each chapter of the book includes a state-of-the-art review in appropriate topic and well selected appropriate references at the end.

With its distinguished editors and international team of contributors *Sensors & Signals* is suitable for academic and industrial research scientists, engineers as well as PhD students working in the area of sensors and its application.

http://www.sensorsportal.com/HTML/BOOKSTORE/Sensors_and_Signals.htm

Regions Matching Algorithms Analysis to Quantify the Image Segmentation Results

Oleh BEREZSKY, Grygory MELNYK, Yuriy BATKO and Oleh PITSUN

Ternopil National Economic University, Lvivska str., 11, Ternopil, 46020, Ukraine

Tel.: +380352475051, fax: +380352475051

E-mail: ob@tneu.edu.ua, mgm@tneu.edu.ua, bum@tneu.edu.ua, o.pitsun@tneu.edu.ua

Received: 20 September 2016 /Accepted: 30 December 2016 /Published: 31 January 2017

Abstract: In the article the matching algorithms of region images are analyzed. The work also presents their advantages and disadvantages. The comparing images algorithm of regions is developed on the basis of the measured chords. The comparison regions algorithms are used to evaluate segmentation algorithms in the Gromov–Hausdorff metric. The algorithm of metric evaluation is developed as an example of biomedical images segmentation.

Keywords: Image, Segmentation quality, Matching, Segmentation, Gromov-Hausdorff metric.

1. Introduction

Image segmentation is one of the fundamental processes in many software applications with image or video processing and computer vision systems. It is often used to divide the image into separate areas that correspond to different real objects. This is an important step in the content analysis stage or in the process of images "understanding". Modern scientists have developed many approaches to solve problems of images dividing into separate areas, but most of the proposed algorithms can solve the problem of segmentation only with a specific type of image [1]. Therefore, the automatic selection of effective segmentation algorithms is a complex task, since the comparison of different algorithms must consider both the type of the algorithm, and the parameters of its work. The main advantages of using segmentation analysis results are: a) objective selection of the best partitioning of the image; b) the possibility of quality control during the segmentation processes of images and correcting the work of the algorithms in real time; c) the ability to attract the most efficient algorithms for

segmentation in the work program of image processing [2].

As a result of segmentation, the following two types of errors occur: the segmented image point is marked in such way as it belongs to a homogeneous region, and it doesn't belong to the field in the model image; in the segmented image the point is not marked as it belongs to homogeneous area, but it is such in the model image [3]. Therefore, two criteria are often used to quantify the quality of segmentations: the level of regions similarity, the level of regions difference [4].

Among the segmentation results test we distinguish the following algorithms: the algorithm based on the Rand index that calculates the plurality of pixels pairs that are marked as tags of the same type and as both the segmentation algorithm and the model splitting [5]. The global consistency error measures the degree if the segmentation can be seen as another refinement of the segmentation and the error is 0, if two segments overlap completely and a certain value is nonzero otherwise. The boundary points error is determined by the algorithm that measures the average deviation of one contour point from the nearest

contour point on the reference segmentation. The accuracy of segmentation is defined as the percentage of correctly segmented points to the number of pixels in an image [6]. The average absolute error characterizes the average difference between the model and actual results obtained for all tests [7].

In addition to the quantitative estimation there is another qualitative (subjective) one. The subjective criteria are the criteria of visual perception, valued during the examination by some groups of observers (experts). One of the approaches to quantify the quality of the segmentation approach is based on metrics usage [8-9].

2. Problem Statement

Let Im be an image. Let's segment this image using a particular algorithm or a set of algorithms for the segmentation, i.e. $S = \{A_1, A_2, \dots, A_k\}$, where A_i is the segmentation algorithm. The result is $S_1(Im) = Im_1$. An expert manually segments the original image. Then we get the image Im_e . Let's present the image data in the forms of (1) and (2).

$$Im_e = \bigcup_{i=1}^{m_e} C_{ei} \cup O_{ei}, \quad (1)$$

where C_{ei} , O_{ei} is the shape and the region marked by the expert.

$$Im_1 = \bigcup_{i=1}^{m_1} C_{1i} \cup O_{1i}, \quad (2)$$

where C_{1i} , O_{1i} is the shape and the region marked by the algorithm.

We use the Hausdorff metric (3) to evaluate the proximity between regions O_1 and O_2 .

$$d_H^X(O_1, O_2) := \max \left\{ \max_{x \in O_1} \min_{y \in O_2} d(x, y), \max_{y \in O_2} \min_{x \in O_1} d(x, y) \right\}, \quad (3)$$

where d_H^X is the Hausdorff distance in the metric space (X, d) .

We evaluate the shortest distance between the regions O_1 and O_2 using the Gromov - Hausdorff metrics (4):

$$d_{GH}(O_1, O_2) := \inf_{X, f, g} d_H^X(f(O_1), g(O_2)), \quad (4)$$

where $f: O_1 \rightarrow X$, $g: O_2 \rightarrow X$ are the isometric embedding of metric space (X, d) .

Thus, to determine the minimum distance between the regions O_1 and O_2 we must perform isometric

transformation in order to find the maximum matching (section), that $S = O_1 \cap O_2 \rightarrow \max$.

3. Solution

After segmenting we obtain two homogeneous areas (Fig. 1), which are generally nonconvex polygons.

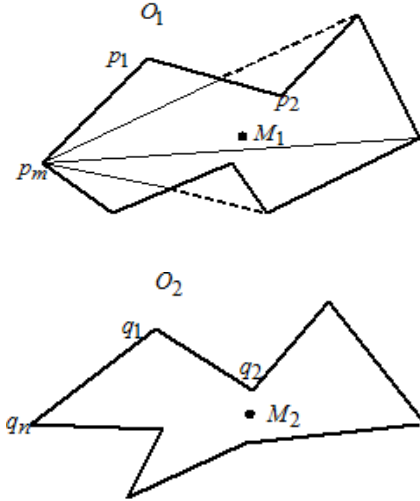


Fig. 1. The homogeneous region obtained after segmentation.

Thus, the problem of the maximum two-section polygons is reduced for the isometric transformation, translation and rotation. There are a number of heuristic algorithms for isometric transformations, such as the use of mass centers, ranges of their subsequent imposition, limiting use of a rectangle and extreme peaks [10].

The isometric transformation calculation requires the development of a number of heuristic algorithms.

The longest chord algorithm is to find two of the longest chords on the polygons. After that we define maximum chord angles slope to the horizontal axis OX . In case of mapping one polygon rotates relative to the other with the corners (5) and (6). The computational complexity of the algorithm is directly proportional to the number of vertices of the polygon n .

$$\beta_1 = |\alpha_1 - \alpha_2|, \beta_2 = 180 + |\alpha_1 - \alpha_2|, \quad (5)$$

where α_1 and α_2 are chord angles to the horizontal axis OX .

The previous algorithm can be modified by calculating the coordinate of the third point. The algorithm of the three points [11] on the contour polygon determines its two most distant points. For this we conduct the segment maximum length $AB = L_{\max}$, which includes the contour. The third point is defined as one that belongs to a median

perpendicular and most distant $CO > C'O$ from the middle of the segment AB (point O). The example of the three points is shown in Fig. 2(a). The matching algorithm performs overlapping centers of polygons and bends in such way that the third point lies on one and the same half-plane. The computational complexity of the algorithm of the three points is also linear and proportional to the number of vertices of the polygon.

The example of a combinatorial algorithm of the three points on the circuit is the section lines algorithm [12]. The algorithm of section lines is the direct construction of lines, crossing the path of some of the starting point A (the farthest point from the center of the polygon mass) through a specified angle α (Fig. 2(b)). At the intersection of a contour n with lines we get n points of the intersection. Then we choose three points for the polygons mapping from the resulting set of points of the intersection. The computational complexity of this algorithm is proportional to n^3 .

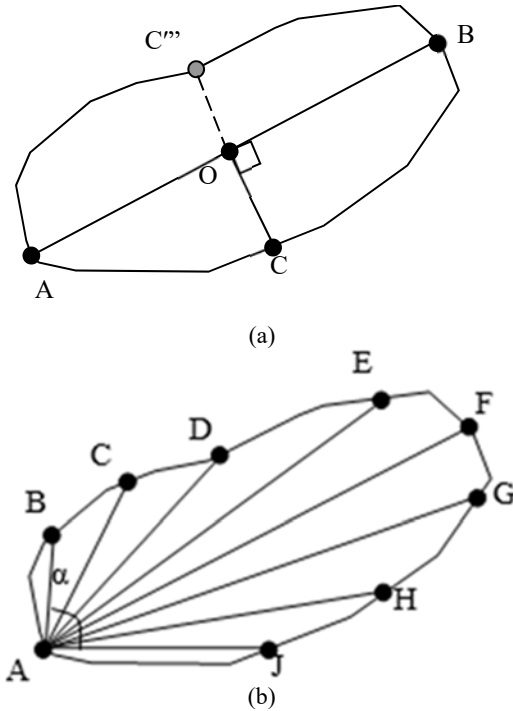


Fig. 2. (a) Algorithm based on three points;
(b) secant lines algorithm.

4. Algorithm of Matching Polygons Based on Measured Chords

For the polygons $O_1 = (p_1, p_2, \dots, p_m)$ and $O_2 = (q_1, q_2, \dots, q_n)$, given that vertices conduct chord. For the polygon O_1 given by m vertices, we get a set of chords $\{h_1, h_2, \dots, h_k\}$, where $k = \frac{m(m-3)}{2}$. For the polygon O_2 , which is given by

n vertices we get a set of chords $\{l_1, l_2, \dots, l_p\}$, where $p = \frac{n(n-3)}{2}$. Thus, in the case of full search, we obtain the following computational complexity $O(n^2 \cdot m^2)$.

In order to reduce computational complexity let's sort the chords by both measuring and using the following coefficients:

a) The ratio of the relative chord length is (6)

$$\delta l_i = \frac{l_i}{l_{\max}}, \quad (6)$$

where l_i is the length of i^{th} chord in the polygon, l_{\max} is the maximum chord length in the polygon;

b) The overlapping polygon chord coefficient (7)

$$\delta_{O_i} = \frac{l_{O_i}}{l_i}, \quad (7)$$

where l_{O_i} is the length of i -th chord in the polygon, belonging to the inner region of the polygon, l_i is the length of i -th chord in the polygon.

Based on the given coefficients δl_i and δ_{O_i} , the coefficients are obtained according to (8)

$$W_i = \alpha \delta l_i + \beta \delta_{O_i}, \quad (8)$$

where α and β are the measure coefficients chosen from the set of the values $[0..1]$ and $\alpha + \beta = 1$.

Then the array of the suspended chords for the polygon O_1 equals to $\{h_{W_1}, h_{W_2}, \dots, h_{W_k}\}$, and for $O_2 - \{l_{W_1}, l_{W_2}, \dots, l_{W_p}\}$.

Then the algorithm to find the Gromov - Hausdorff distance is:

1. We obtain the expert regions O_1 and O_2 using both the algorithm segmentation and the segmentation.

2. For the regions O_1 and O_2 we conduct piecewise linear approximation image edges (9):

$$O_i = \bigcup_{j=1}^l \{(x, a_j x + b_j) | x \in [c_j; d_j]\}, \quad (9)$$

where $a_j, b_j, c_j, d_j \in R, i = \overline{1, 2}$ and we obtain the polygons.

3. On the basis of the Formulas (6), (7), (8) we form the arrays of the measured chords for the polygon $O_1 - \{h_{W_1}, h_{W_2}, \dots, h_{W_k}\}$, and for $O_2 - \{l_{W_1}, l_{W_2}, \dots, l_{W_p}\}$.

4. We give the threshold Δ and sort arrays of the chords for the regions O_1 and O_2 according to the conditions $W_i \leq \Delta$.

5. We calculate the centers of the masses $M_1(x_{C_1}, y_{C_1})$ and $M_2(x_{C_2}, y_{C_2})$ for the regions O_1 and O_2 .

6. We perform parallel translation P of the region O_2 to O_1 so that the masses M_1 and M_2 centers match.

7. We perform rotation of R with the difference of rotations θ_1 and θ_2 , found on the base of the sorted chords.

8. Then, we find the Hausdorff distance using the following Formula (10):

$$d_H^x(O_1, O_2) := \max \left\{ \max_{x \in O_1} \min_{y \in O_2} d(x, y), \max_{y \in O_2} \min_{x \in O_1} d(x, y) \right\} \quad (10)$$

5. Experimental Results

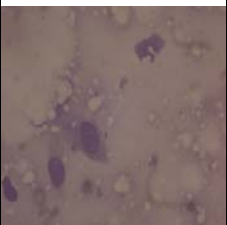
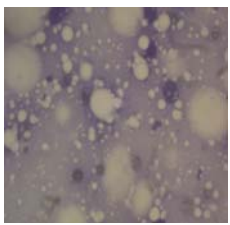
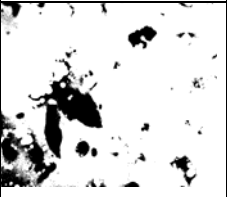
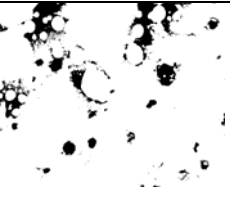



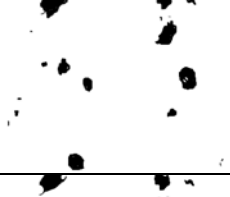




The database of histological and cytological images of precancerous and cancerous conditions of the mammary gland was used for the experiments and it was also developed by the authors [13]. Generally, cytological and histological images are characterized by high complexity processing. The main disadvantages are the presence of different kinds of noise and high definition. The image preprocessing module is based on the library OPENCV [14] as well as it is designed to be adapted to different types of images and to improve their quality. Its work includes the following stages:

1. Image loading;
2. Determining the level of brightness, the average value of red, green and blue channels of RGB image input;
3. Options selection in order to improve the picture quality depending on the input parameters obtained in step 2. In this case, there are the following operations: brightness adjusting, contrast, morphological operations (dilate, erode);
4. Filtering by averaging filter, window size 7×7 . This allows the image filter part;
5. Determining the peak signal to noise ratio. We have then the input data as the original and filtered image;
6. Image filtering algorithms (median, Gaussian, bilateral and other adaptive filters); selecting the type of filter and its parameters depends on the peak signal to noise ratio;
7. Image segmentation with k-means algorithm. As a result of the experiments for cytological image, k-means algorithm has shown the best results;
8. Threshold segmentation. Threshold segmentation is used to obtain images of the "object - background".

Table 1 compares the results of image segmentation algorithms with and without preprocessing. Image

preprocessing is principle in order to improve the segmentation quality, including the adjustment of brightness and contrast. Noise reduction improves the segmentation quality significantly. To assess the quality of segmentation we use the Hausdorff metric, the Gromov - Hausdorff metric and the Gromov - Freshe metric.

Table 1. Results of cytological image segmentation with and without preprocessing.

Images Type of processing		
Thresholding without preprocessing		
K-means without preprocessing		
Thresholding with preprocessing		
K-means with preprocessing		
Expert		

The experiments were conducted on a test sample of 100 images. Table 2 presents the mean values of distances in the investigated metrics for different segmentation algorithms with and without preprocessing of images.

For experimental studies of the algorithm we have created the arbitrary set of test images of nonconvex areas. The images examples are shown in Fig. 3.

We have performed a pairwise matching images of nonconvex regions with each other and in each case the Gromov-Hausdorff distance is calculated. Fig. 4 shows the difference (deviation) found within each experiment, the distance found full-force, which is accepted as the reference. Each line of the graph represents a different algorithm. The algorithms are marked as: the longest chord, the algorithm of three points calculation – 3 points, the secant method, the developed algorithm – the list of chords. As we see, the developed algorithm determines the distance between the regions with precision.

Table 2. Evaluation of segmentation.

Metrics Type of processing	Hausdorff	Gromov-Hausdorff	Frechet	Gromov-Frechet
Thresholding without preprocessing	304.53	304.53	307.56	305.7
K-means without preprocessing	89.4	89.23	89.4	89.23
Thresholding with preprocessing	13.45	12.36	13.45	12.36
K-means with preprocessing	10.21	10.02	10.21	10.02



Fig. 3. Example of test images.

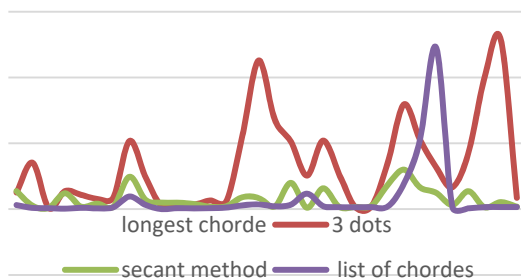


Fig. 4. Deviations of the Gromov-Hausdorff distance for some experiments on the outcome of full search.

Fig. 5 shows the evaluation of the execution time of each algorithm. If we match the accuracy at the level of the exhaustive algorithm search the developed algorithm shows the time at other algorithms based on contour features.

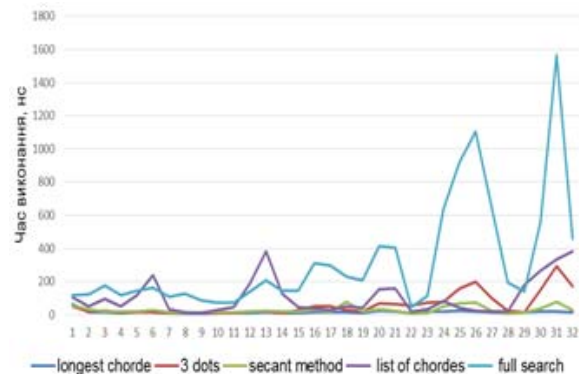


Fig. 5. Execution time for each algorithm.

We have worked out the algorithm to find the smallest distance between regions using the coefficient of relative chord length and the chord coefficient of an overlapping polygon. To assess the region in which the coefficients make the least difference, we have built the graph of the distance from the coefficients (Fig. 6). In the figure the relative chord length coefficient is pointed as Chorde distCoef, and the coefficient of the polygon chord overlapping is pointed as Chorde overlapCoef.

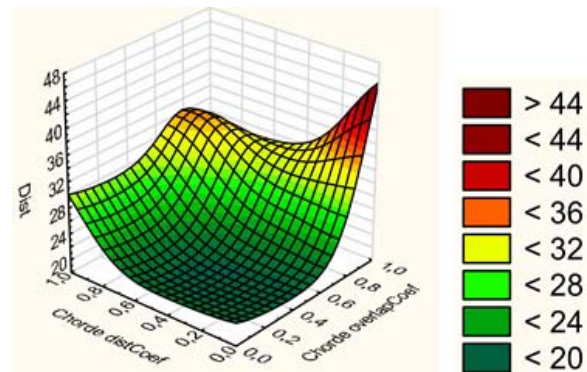


Fig. 6. Dependence of the Gromov-Hausdorff distance on the chord length coefficients and the overlap region.

5. Conclusions

Thus, the previous image processing significantly affects the quality of image segmentation cytology. The distances in metrics of previously processed images are much smaller than the images without preprocessing. Moreover, the k-means segmentation algorithm has shown better results in all metrics than the threshold segmentation.

Finally, we have worked out the algorithms, which are the most accurate as for time and commensurate

expenses. They are compared for nonconvex regions in case of the Gromov-Hausdorff distance calculation among the following algorithms: the longest chord of three points, the secant, the measured chords algorithm.

Acknowledgements

The proposed research has been developed within the state budget project "Hybrid Intelligent Information Technology Diagnosing of Precancerous Breast Cancer Based on Image Analysis" (state registration number 1016U002500).

References

- [1]. Zhang Y. J., An Overview of Image and Video Segmentation in the Last 40 Years, in *Advances in Image and Video Segmentation*, *IRM Press*, 2006, pp. 1-15.
- [2]. Sharma M., Chouhan V., Objective Evaluation Parameters of Image Segmentation Algorithms, *International Journal of Engineering and Advanced Technology (IJEAT)*, Vol. 2, Issue 2, December 2012, pp. 84-87.
- [3]. Christensen H. I., Phillips P. J. (editors), Empirical evaluation methods in computer vision, *World Scientific Publishing Company*, July 2002.
- [4]. Philipp-Foliguet S., Guigues L., Multi-scale criteria for the evaluation of image segmentation algorithms, *Journal of Multimedia*, Vol. 3, No. 5, December 2008, pp. 42-56.
- [5]. Chinnadurai V., Chandrashekhara G., Improved levelset method for segmentation and grading of brain tumors in dynamic contrast susceptibility and apparent diffusion coefficient magnetic resonance images, *International Journal of Engineering Science and Technology*, Vol. 2, No. 5, 2010, pp. 1461-1472.
- [6]. Zhang Y. J., Image segmentation evaluation in this century, in *Encyclopedia of Information Science and Technology*, ed. M. Khosrow-Pour, 2nd ed., *IGI Global*, 2009, pp. 1812-1817.
- [7]. Padamavati S., Subashini P., Sumi A., Empirical Evaluation of suitable segmentation algorithm for IR Images, *IJCSI*, Vol. 7, Issue 4, No. 2, July 2010, pp. 22-29.
- [8]. Berezsky O. N., Berezskaya E. N., Quantitative evaluation of the quality of the segmentation of images based on metrics, *Upravlyayushchie Sistemy i Mashiny*, Vol. 6, 2015, pp. 59-65.
- [9]. Berezsky O., Batko Yu., Melnyk G., Verbovyi S., Haida L., Segmentation of Cytological and Histological Images of Breast Cancer Cells, in *Proceedings of the 8th IEEE International Conference on Intelligent Data Acquisition and Advanced Computing Systems: Technology and Applications (IDAACS)*, 24-26 September 2015, pp. 287-292.
- [10]. Skiena S. S., *The Algorithm Design Manual*, *Springer*, 2008, 730 p.
- [11]. Berezsky O. N., The algorithm of analysis and synthesis of biomedical images, *Journal of Automation and Information Sciences*, Vol. 39, Issue 4, 2007, pp. 69-80.
- [12]. Melnyk G., Algorithm of matching of microobjects with different shapes, in *Proceedings of the Information Technologies in Innovation Business Conference (ITIB)*, 2015, pp. 31-34.
- [13]. Berezsky O., An Intelligent System for Cytological and Histological Image Analysis, in *Proceedings of the 13th International Conference 'The Experience of Designing and Application of CAD Systems in Microelectronics' (CADSM'15)*, Polyana-Svalyava (Zakarpattia), Ukraine, 24-27 February 2015, pp. 28-31.
- [14]. Berezsky O., Automated Processing of Cytological and Histological Images, in *Proceedings of the XIIth International Conference «Perspective Technologies and Methods in MEMS Design» (MEMSTECH'16)*, Lviv-Polyana, 20-24 April 2016, pp. 51-53.



Published by International Frequency Sensor Association (IFSA) Publishing, S. L., 2017 (<http://www.sensorsportal.com>).

SENSORS & TRANSDUCERS

The Global Impact Factor of the journal is **0.987**

Open access, peer reviewed, established, international journal devoted to research, development and applications of sensors, transducers and sensor systems.

Published monthly by International Frequency Sensor Association (IFSA Publishing, S.L.) in print and electronic versions (ISSN 2306-8515, e-ISSN 1726-5479)

Submit your article at:
<http://www.sensorsportal.com/HTML/DIGEST/Submission.htm>

Evaluating Image Precision of Acoustical Imaging Diffraction by Focused Ultrasound Beam

^{1a} Jinwen DING, ² Dewen ZHENG, ³ Han DING, ⁴ Kang LI, ^{1b} Qichen MA,
^{1c} Guochao HE, ^{1a} Jingjing LIU and ^{1a} Junhua CHEN

^{1a} CAS Key Laboratory of Materials for Energy Conversion; Department of Materials Science and Engineering; ^{1b} School of the Gifted Young; ^{1c} School of Computer Science and Technology, University of Science and Technology of China, 96 Jinzhai Road, Hefei, 230026, China

² Research Institute of Petroleum Exploration and Development, Donghuan Road, Langfang, 065006, China

³ School of Mechanical and Electrical Engineering, Shaanxi University of Science and Technology, 6 Xuefu Middle Road, Xi'an, 710021, China

⁴ Anhui Academy of Coal Science, 81 Xuancheng Road, Hefei, 230001, China
E-mail: cjh@ustc.edu.cn, zdw69@petrochina.com.cn, jwding@ustc.edu.cn

Received: 30 December 2016 / Accepted: 24 January 2017 / Published: 31 January 2017

Abstract: The paper concisely reveals an acoustic behavior - acoustic diffraction (scattering) phenomena, which arises between a spherical cavity of acoustic lens and the microstructure of an object in immersion. As the result, this phenomena cause some negative influence on acoustical imaging precision. As a certain condition is satisfied, the outline of microstructure in acoustic images become blurred, the image precision is somewhat corroded. The paper introduces a brief evaluation approach to this acoustic interaction, and provides some typical characteristics of this acoustic interaction in two-dimensional (2D) and three-dimensional (3D) acoustical images. The paper suggests the researcher should take into account this interaction behavior - diffraction, to avoid any misrepresentation as investigating microstructures and imaging characterization, promoting the accuracy for materials characterization through the acoustical images by scanning acoustic microscopy technology (SAM), in the application field of non-destructive Testing / Evaluation (NDT/E).

Keywords: Transducer, Acoustic lens, Scattering and diffraction, Time-of-flight (TOF), Signal aberration, Acoustical imaging, Scanning acoustic microscopy, Non-destructive testing / evaluation (NDT/E).

1. Introduction

The technology of Scanning Acoustic Microscopy (SAM) is widely used in materials sciences. It was originally proposed by Quate and Lemons in 1974 [1]. In many modern high-tech industrial fields, the micro-sized internal defects inside a solid bulk material hide extreme risk in some applications. The microscopic inspection of internal defects for

material characterization is prerequisite for some vital applications. SAM just provides the technology to detect this kind of internal defects in a non-destructed way in NDT/E field [2, 3]. In materials science SAM also provide powerful means to investigate the micro-sized internal structure and its characterization for bulk materials.

The mature two-dimensional (2D) imaging techniques, including A-(O-), B- and C-scan image

by SAM, is used for evaluating the internal structures of non-transparent solid bulk specimen powerfully. Besides these 2D acoustical imaging techniques, based on isosurface technique a new approach to realize the three-dimensional (3D) acoustical imaging is proposed by Ding and He et al in 2013 [7, 8]. 3D scanning acoustic microscopy (3D SAM) will become a more attractive technology for the visualization of internal micro-sized structures in nondestructive testing/evaluation field [10].

Both two-dimensional acoustical imaging and three-dimensional acoustical imaging technology of SAM system, work based on a common platform, including same scanning system, electrical blocks, data conversion block, and database of computer. In any way, these two methods are both performed with the same kernel unit – acoustic lens. Acoustic lens is the key execute technology in the system [5].

The principle and process to produce acoustical image by acoustic lens are essentially based on the application of ultrasound wave behavior. Ultrasound wave is very sensitive to the varieties inside a local region - focal spot. The secondary acoustic response - waves arise from a serial of consecutive focal region on/inside the specimen. As the results, all acoustic interacted behavior - waves are collected from these regions, bringing all information of internal microstructures of the specimen. Variations of acoustic signal coming from diverse points of bulk material are displayed in the screen as a pixel of acoustical image. According to its own mechanism of acoustical contrast, all internal structures information is represented in acoustic images as each different pixel in a various degree of contrast.

In the application of scanning acoustic microscopy, various types of acoustic waves present their own appearance in acoustical image. The phenomena of scattering and diffraction as an adjunct acoustic behavior obviously contribute its influence on the final results of acoustic imaging [4, 6].

2. Evaluation

Acoustic lens is the ultrasound focusing system, which plays two roles in SAM - an actuator and a receiver. As an actuator, its native characteristics determine the basic resolution in acoustical imaging substantially. As a receiver, all ultrasound interaction and its various responses between the actuator and observation in immersion, including additional and even negative interaction which is inevitably collected, converted and involved into imaging process.

2.1. The Physical Structure of Acoustic Lens

Acoustic lens is an actuator, which consists of a disc-shaped plane piezoelectric transducer on the top of the waveguide, and a spherical cavity on the end side of the waveguide. See Fig. 1.

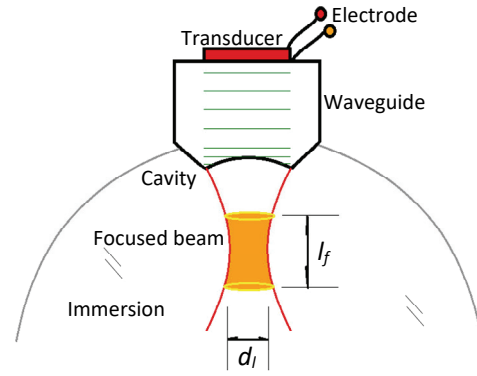


Fig. 1. A plane transducer and a spherical cavity located on two ends of the waveguide of an acoustic lens.

Based on the piezoelectric effect, the electrical generator excites a fast electric shock to the disc-shaped transducer, producing an acoustic ultra-short wave (pulse) at the boundary between the transducer and the waveguide of acoustic lens. This ultra-short wave propagates in a type of plane wave inside the waveguide of acoustic lens, towards the cavity on the other side of waveguide [9]. As this plane wave arrives at the spherical interface between the cavity in waveguide and the immersion (water), in term of Snell law - the spherical cavity of acoustic lens produces a convergent ultrasound probe beam into the immersion.

This convergent probe beam forms a caustic zone in water immersion. The structure and its parameters of this focused beam are determined by two factors - the frequency of transducer and the physical characteristics of the spherical cavity embedded in the end side of waveguide.

The variant l_f and d_l is the length and diameter of this focused beam produced by acoustic lens. See Equation (1) and (2). These two characters are determined by two parameters - λ and θ_m .

$$l_f = \frac{2\lambda}{1 - \cos \theta_m} \approx \frac{4\lambda}{\theta_m^2} \quad (1)$$

and

$$d_l = \frac{0.61\lambda}{\sin \theta_m} \approx \frac{0.6\lambda}{\theta_m} \quad (2)$$

The parameter λ is the wavelength of this plane wave, θ_m is the maximal half angle of the cavity drilled inside the end side of waveguide of acoustic lens. These two parameters exhibit the native essential character of an acoustic lens, which are the key factor for an scanning acoustic microscope intrinsically, to contribute the basic resolution in acoustical imaging.

In the application of acoustic lens for SAM, the higher frequency value f of the transducer provides the more less value of l_f and d_l - the smaller sizes of the focal zone (spot) inside immersion and specimen.

Practically in the field of SAM, for a high resolution acoustical imaging, usually a high working frequency of the transducer is employed, usually fabricated from 20 MHz up to 3000 MHz to obtain a small caustic-shaped focused probe beam in immersion, with the diameter of this focal spot being in tens of micrometers.

For the same purpose, the bigger value θ_m of the cavity of acoustic lens provides the smaller value of l_f and d_f , which also means the smaller sizes of this focal zone (spot) and higher resolution are realized for the acoustic lens and SAM system.

On the contrary, in most application of SAM, acoustic lens is also being a receiver while the system only employs a unique acoustic lens in a SAM. The cavity of acoustic lens has the capability to collect the echo ultrasound waves from the specimen in immersion; also, in term of Snell law the spherical cavity of acoustic lens transfer all these collected ultrasound responses through the bulk of waveguide to the transducer on the top of waveguide. According to converse piezoelectric effect, the transducer receives and transforms all various ultrasound waves into a serial of electric ultrasound signals in an echo signal pattern. In this process, some natural, additional, and faint hidden acoustic behavior is also carried among these signal sequences in echo signal patterns.

2.2. Acoustic Scattering Behavior

In the procedure of acoustical imaging, the native character and parameters of acoustic lens in a SAM determine the basic resolution of images. At the same time, all ultrasound interactions received by acoustic lens also contribute their comprehensive influences on the precision of acoustical images.

All acoustic responses received by acoustic lens are a sensitive way to exhibit in acoustic images, including all kinds of faint interactions from the micro interface on/inside the observation object. Scattering phenomena is such a usual acoustic interaction in nature, while an acoustic wave meets with a spatial spot in a wave field.

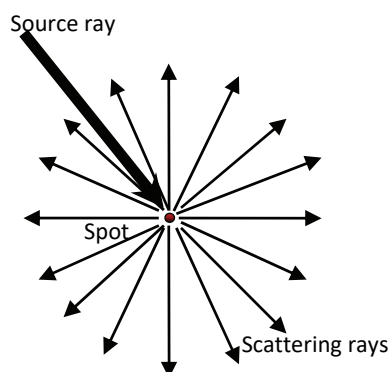


Fig. 2. An acoustic source ray meets with a particle and produces a plenty of scattering rays around this particle.

Fig. 2 shows a pattern about the acoustic scattering phenomena. The figure demonstrates an acoustic scattering behavior takes place around an individual particle (spot) in a field.

As a main acoustic wave (source ray) propagates to a spatial central spot – a particle, the source ray meets with this particle and interact each other, then the acoustic wave scatters out around this particle. Some of scattering is reflected in an opposite direction along the original route, but most of scattering are reflected in any arbitrary angle to any other directions. Generally, the scattering rays transmit outside from the central spot, spreading out in a disperse direction. This transmitting behavior is not only limited inside a two-dimensional plane, but in a kind of three-dimensional full directions around the central spot. In this case, for a receiver or a sensor located at any arbitrary position from any arbitrary direction, it is only small amount of these scattering rays can be collected and contribute their influence.

2.3. Acoustic Edge Diffraction

Once a serial of individual particles (spots) are placed next to each other in a spatial, and extend along one dimensional direction as an edge (line), where a wave resource radiate and excite, all scattering behavior from every particles in the edge present a comprehensive diffraction formation around this edge.

Edge diffraction takes place around the angular elements, such as corner, edge, wedge, etc. [4] See Fig. 3. The figure shows and interprets a typical behavior of edge diffraction.

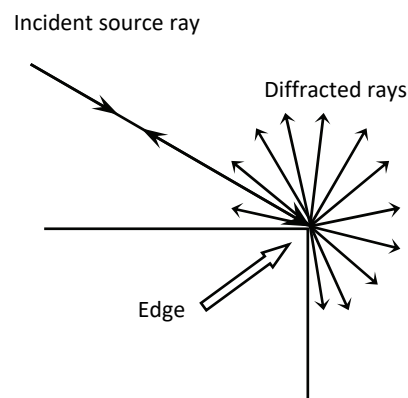


Fig. 3. Schematic of edge diffraction - acoustic interaction between an incident ray and an edge.

As the incident rays interact with the edge, there are two kinds of interaction possibilities:

1) As an incident ray excites the edge in a normal plane, which is perpendicular to the edge, the diffracted rays arise from the incidental spot, and the diffraction spread out limited inside the same perpendicular normal plane.

2) Once the incident ray excites this edge along an arbitrary direction with an angle, all diffracted rays disperse out with the same angle but in an opposite side from the incidental spot, forming a crossed pyramidal tract.

In these cases, once an observation object in a shape of particle (spot) or outline (sharp edge), which is placed under an ultrasound wave field, scattering and its integral behavior - edge diffraction will release its acoustic response.

3. Experimental

Based on Raster principle, driven by a mechanical scanning system, acoustic lens moves along the scanning route in x , y , z coordinately - point by point, and line by line over a specimen in immersion. According to the spatial positions of acoustic lens, and the relevant digital ultrasound signals in echo signal pattern at each position, which is depicted by the intensity for every pixel in a two-dimensional image (B-, C-Scan). In this experiment a small aperture acoustic lens is employed with $\theta_m \approx 6^\circ$ and focus time delay is $27.5 \mu\text{s}$.

3.1. Edge Diffraction in Acoustical Imaging

For this evaluation, a thin plate specimen is used whose outline is with a sharp edge. As the acoustic lens is driven by the mechanical scanning system in a unidirectional (x or y), a transversal topography inside specimen - B-Scan image is obtained; in a cross-direction (x and y) a lateral topography (cross-section) - C-Scan image showing at different level inside specimen is realized. Under this imaging technology, the formation of edge diffraction is introduced by Ding and Levin et al in 2011 [6]. See Fig. 4.

As the focus of convergent ultrasound probe beam by acoustic lens is located below the surface of a plate specimen, while the acoustic lens moves in unidirectional x , a transversal 2D image - B-scan

image is obtained in picture a) of Fig. 4. A parabolic line opens upward from the point on the edge of this plate specimen, almost in a symmetrical shape occurs around at this point of the edge in B-scan image.

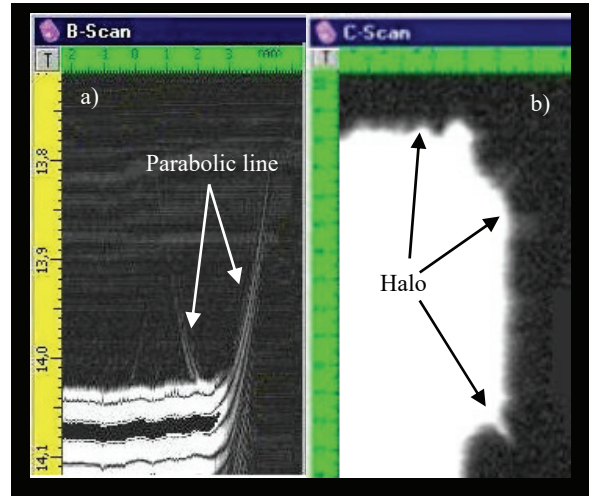


Fig. 4. Edge diffraction and its formation exhibited in B-Scan and C-Scan image.

On the other hand, while the acoustic lens moves along x and y direction, and, by setting the width of electrical gate at the depth on the surface in echo signal pattern, a cross-section image is obtained in the picture b) of Fig. 4 - C-scan image, displaying the surface of this plate specimen. The picture b) exhibits a plenty of halo rim around the outline of this plate specimen obviously. Just this plenty of halo rim results in a blurry outline of specimen in C-Scan image. The appearance size (area) of this specimen in C-Scan image is enlarged than its native size.

The diffraction formation in two pictures a) and b) of Fig. 4 is a couple of relevant view each other for the same outline of the specimen. For the reason of edge diffraction, different formation in two kinds of images makes the imaging characterization becomes more complicated for investigators.

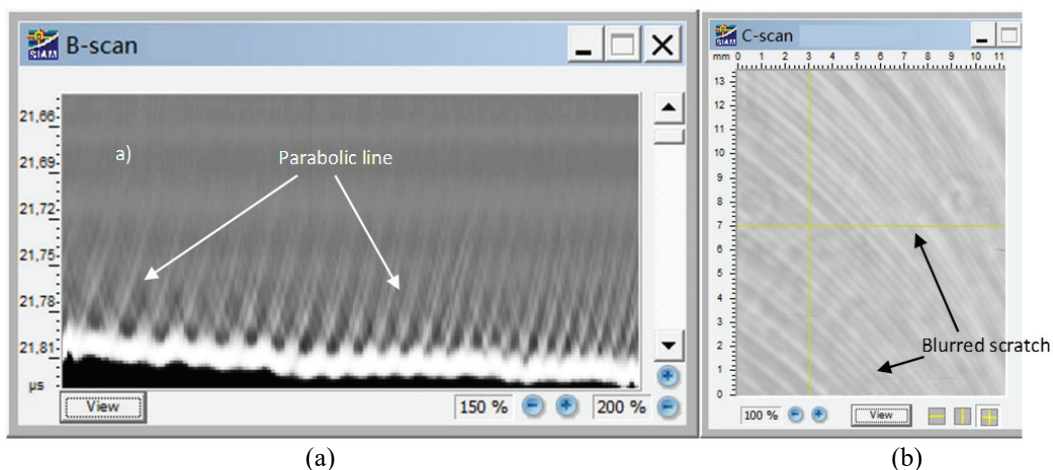


Fig. 5. Edge diffraction and its influence on 2D acoustical imaging for a surface evaluation.

3.2. Surface Characterization in Acoustic Image

A metallic machining parts is polished, and still remained with many mechanical scratches on its surface. The picture a) in Fig. 5 is the surface of it in a transversal B-Scan image. While the focus of convergent ultrasound beam is below the surface of this specimen, many parabolic lines arise upward at every minim burr on the surface of machining parts in B-Scan image.

Correspondingly in the picture 2) in Fig. 5 - C-Scan image, these mechanical scratches are observed with many curves tightly distributed on its surface. This C-Scan image provides scratches distribution on the surface qualitatively. All scratches on the surface are blurred in C-Scan image. The outlines or edges of all scratches cannot be distinguished explicitly. The imaging precision is damaged by edge diffraction.

3.3. Internal Structure in Acoustic Image

SAM is a convenient technology to investigate internal microstructure for bulk materials. Fig. 5 gives an acoustical imaging for the characterization of a piece of bulk materials with an internal laminated structure within a local area.

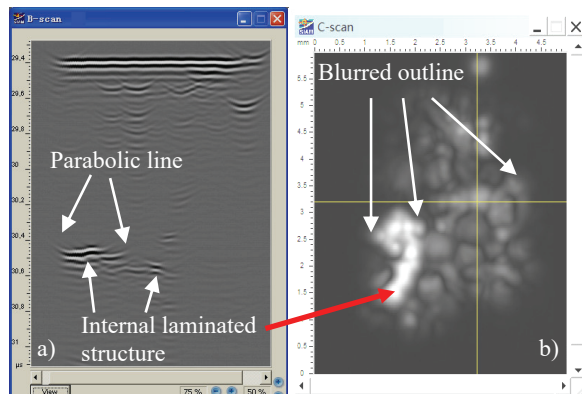


Fig. 6. Visualization of internal microstructure in 2D acoustical imaging and its appearances.

The picture a) and b) in Fig. 6 exhibit two 2D images - B- and C-scan image, showing the profile of some internal structure inside a solid bulk specimen. The ripples with some parabolic lines are the internal laminated microstructure in B-Scan image. The C-Scan image (the picture b) gives a bright area relevant to the ripples areas in picture a).

The brightness of local area with a different contrast represents some internal local area – laminated internal interface and its distribution in a horizontal level along x and y in C-Scan image.

It also obviously shows that the bright areas are surrounded by their own blurred rim. It also provide unclear outline of internal microstructures in the image, and the areas size of internal local microstructures are enlarged too.

3.4. Internal Structure in 3D Acoustic Image

Three-Dimensional acoustical imaging for bulk specimen by SAM is proposed and realized. The method - isosurface technique and square column model which is employed in 3D SAM, which is sensitive to catch the weak signal variance, and exhibit the variance in a full direction way for a bulk materials [7, 8, 10].

Therefore, as the convergent beam reaches and excites the micro edge of internal structures or big particles inside a specimen, phenomena of scattering and diffraction is more sensitive and evident displayed in 3D acoustical imaging than in 2D acoustical imaging.

The picture a) in Fig. 7 shows some internal microstructure (void, defect or inclusion) inside a piece of bulk materials in 3D acoustical imaging. The arrows point out the minim rim surrounding its kernel - internal microstructure in picture a). By the procedure to adjust the signal process for 3D imaging, the investigator may more conveniently find the involving regularity to catch the kernel - the real internal microstructure for characterization using 3D acoustical imaging technology.

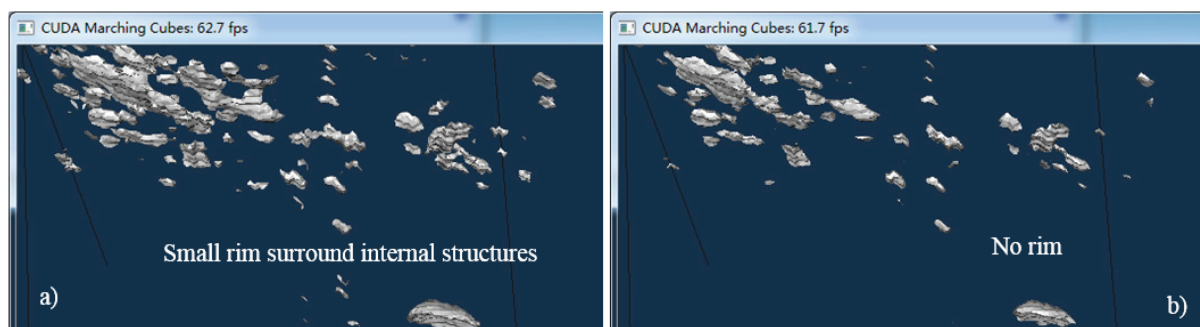


Fig. 7. 3D visualization of internal microstructure and the influence by phenomena - Scattering and diffraction in three-dimensional acoustical imaging.

So, the picture b) presents the internal microstructures in 3D image, by reducing the influence from acoustic scattering and edge diffraction. Comparing two pictures between picture a) and b), the volume of all internal microstructures with their own rims in picture a), are bigger than the volume of all same particles in picture b). Phenomena - scattering and edge diffraction also enlarge the volume size than its real volume of internal microstructures for evaluation and characterization in 3D acoustical imaging.

4. Calculation

The above experimental results show that, in immersion as a particle or an edge is placed within a field of convergent ultrasound beam, the particle rise up an acoustic response - scattering or edge diffraction responding to this source radiation.

Fig. 8 provides the physical interaction model which interprets the acoustic interaction, between an arbitrary spatial particle in a field of convergent ultrasound beam and a spherical cavity of an acoustic lens. In the focusing system, the spherical cavity of acoustic lens produces its physical focus in immersion - symbol O . In fact, the virtual focus by a spherical cavity in water is deeper than its physical focus. In this paper, the authors use a physical focus model to investigate this interaction.

The line $A'A$ is the symmetry line of the acoustic lens pass through its focal position - focus, which is perpendicular to the interface of cavity; the line $B'B$ is the one pass through the arbitrary position B and focal position, which is also the one perpendicular to the cavity; the angle between these two lines is an angle θ ; the parameter θ_m is the maximal half angle of the cavity of acoustic lens; parameter c is the sound velocity in water.

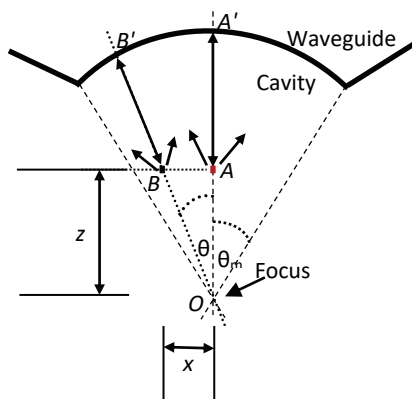


Fig. 8. The schematic about a scattering (diffraction) interaction between a particle (edge) and a spherical cavity.

An arbitrary particle is placed on a horizontal plane in water inside a convergent beam, where its vertical displacement from the focus is variant z ; on

its horizontal plane this particle shifts from position B to A . The horizontal displacement from position B to A is variant x . Position A is just located on the central symmetry line of acoustic lens.

In this convergent ultrasound field in water, the perpendicular distance to the cavity from the position A and B is different individually. The distance - A' to A is bigger (longer) than the distance - B' to B . The time interval (difference) between the cavity and two position of particle - position - A and - B is induced in equation (3) [6].

$$\tau_D = \pm \frac{\sqrt{z^2 + x^2} - |z|}{c}, \quad x \leq |z| \cdot \tan \theta_m \quad (3)$$

The value of variant τ_D is the time interval between the position A - equivalent to the main reflected signal from the surface of a specimen, and the position B - equivalent to the diffracted signal from the particle or edge of a specimen. The equation (3) reveals that diffraction is tightly relative to Time-Of-Flight (TOF), which depends on the direction and the route of acoustic wave propagation.

The sign of equation (3) reveals the time interval changed as the focus of acoustic lens cavity is below or up than the front face of plate specimen. The branches and its open direction of a parabolic line in B-Scan image, are directed upward or downward as the focus of acoustic lens is below or over than an observation object.

5. Discussion

Comparing to the diffraction model above, the formation of edge diffraction in an echo signal pattern is shown in Fig. 9. The picture shows two signal formation difference as an edge of a plate specimen shift from position A to B under a convergent ultrasound beam.



Fig. 9. The formation of a diffracted echo pulse in echo signal pattern as the edge located at two positions.

The formation in the picture a) is relevant to signal response as the surface of plate specimen occupying the position A , showing a typical reflected main pulse signal; and the picture b) is relevant to the moment, which the edge of specimen shifts to the

position B , at this moment a diffracted echo signal respond, with a signal aberration appears in echo signal pattern.

Theoretically, the equation (3) gives the explanation that, once the object is located at a defocus condition inside a convergent ultrasound beam, all these formations by the diffracted echo pulse take part into the imaging process, impacting on one-, two- and three- dimensional images:

1) In A- (O) -Scan imaging, also in echo signal pattern, a diffracted echo pulse signal from the edge, is attached and even merges with the main reflected pulse (signal) which is from the specimen surface;

2) In B-Scan imaging, as the outline (sharp edge) of a microstructure located on the surface or inside the bulk specimen, a symmetrical parabolic line is opened upward or downward at its end position of edge. The open degree of parabolic line is determined by the variant – the value of horizontal and vertical displacement from the focus;

3) In C-Scan imaging, as the outline (sharp edge) of microstructure located on the surface or inside the bulk specimen, a plenty of halo rim surrounds all microstructures. It blurs the outline and enlarges the area size of microstructures in image, and results in the image worse precision for visualization and its characterization. The blurry degree is also determined by the variant - the value of horizontal and vertical displacement from the focus;

4) In 3D imaging, all halo rims caused by scattering or diffraction expand in full direction. It makes the visualization and characterization complicated. The volume of microstructure in image is enlarged too;

5) The model in Fig. 8 and equation (3) induces that, as the focus of convergent beam is just concentrated on a horizontal level, at which the surface of a microstructure (object) is located, the phenomena diffraction can be lessen maximally. Only at this moment and in this way, it is possible to obtain a high precision imaging with all these acoustic images for testing and evaluation using SAM technology.

5. Conclusion

Scanning Acoustic Microscopy is a sensitive technology to investigate internal microstructure for a nontransparent bulk material. Its imaging precision is a basic consideration for some new potential applications. The authors concisely point that, the imaging precision of SAM technology is not only determined by the native properties (frequency and maximal half angle) of acoustic lens, the external possible element - high precision mechanical scanning system is also a necessary operative condition. Indeed, the authors emphasize that acoustical imaging precision is also determined and influenced by an external additional acoustic interacted behavior – scattering and diffraction phenomena.

Phenomena scattering and diffraction is widely exist in nature. The authors introduce that, in the application of SAM edge diffraction arises as a specific condition satisfied – the defocusing in a convergent ultrasound field, the acoustic interaction between a spherical cavity of acoustic lens and the micro interface (particle, edge, sharp outline) of an object in immersion.

The authors emphasize that the phenomena diffraction is an inevitable behavior taking part in the imaging process of SAM. The paper presents all representative formation in 2D acoustical imaging (A-(O-), B- and C-Scan) and 3D acoustical imaging: a parabolic line around the particle of edge of a structure in B-Scan image, a blurred outline and its enlarged area of a microstructure in C-Scan image, and its enlarged volume of a microstructure in 3D acoustical image.

The authors interpret its essential reason in physics about this acoustic interaction. It gives a clue that, to realize a high precision acoustical imaging employing SAM, the key is to arrange the focus of acoustic lens concentrated on the structures which the investigator are interest on/inside a specimen. Finally, the authors remind that the investigators should take into account edge diffraction and its influence while evaluation and characterization process, to promote the evaluating accuracy in NDT/E field by using Scanning Acoustic Microscopy.

Acknowledgements

This work is funded by the National Natural Science Foundation of China (NSFC) under Grant No.61271403 and Grant No.61671423, also supported by CAS Strategic Priority Research Program under Grant No.XDB10030402, and also by Scientific Research and Technology Development Program of PetroChina CNPC-CAS Strategic Cooperation Research Program under Grant No.2015A-4812.

References

- [1]. Lemons R. A., Quate C. F. Acoustic Microscopy - Scanning Version, *Appl. Phys. Letter*, 1974, 24, 4, pp. 163-166.
- [2]. Kino G. S., Acoustic Waves: Devices, Imaging and Analog Signal Processing, *Prentice-Hall*, Englewood Cliffs, New Jersey, 1987.
- [3]. Briggs A., Acoustic Microscopy, *Clarendon Press*, Oxford, 1992.
- [4]. Harris J. G., Edge Diffraction of a Compressional Beam, *Journal of Acoustic Society of America*, 1987, 82, 2, pp. 635-646.
- [5]. Zinin P. V., Kolosov O. V., Lobkis O. I., Maslov K. I. Imaging of Spherical Objects in a Reflecting Acoustic Microscope., *Acoustical Physics*, 1993, 39, 4, pp. 343-346.
- [6]. Ding J. W., Levin V. M., Petronyuk Y. S., Edge Diffraction Phenomena in High-Resolution

- Acoustical Imaging, *Acoustical Imaging*, 2012, 31, pp. 299-312.
- [7]. Ding J. W., He G. Ch, Li K., Dong L. F, Yao Ch. M., Li F., A Construction Model for 3D Imaging of Scanning Acoustic Microscopy, *ICIG2013, IEEE Image and Graphics*, 2013, pp. 1-4.
- [8]. He G. Ch., Ding J. W., Levin V. M., Dong L. F, Bogachenkov A. N., Li K., Yao Ch. M., Zakutailov K. V., Petronyuk Yu. S., Li F., Morokov E. S., Three Dimensional Acoustical Imaging Based on Isosurface Technique for Bulk Material, *Sensors and Transducers, Vol. 156, Issue 6, June 2013*, pp. 168-175.
- [9]. Ding, J. W., Zhang, Q. P., Levin, V. M., Li, K. and Liu, W., A Model For Acoustic Ultra short Pulse by a Disc-shaped Transducer, in *Proceedings of the Symposium on Piezoelectricity, Acoustic Waves, and Device Applications (SPAWDA'14)*, 2014, pp. 48-51.
- [10]. Ding J. W., Li K., Li N., He G. Ch, Zhang Q. P., The Micro-sized Internal Structure in Acoustic Image by 3D Impulse Scanning Acoustic Microscopy, *Proc. SPIE 9903, Seventh International Symposium on Precision Mechanical Measurements*, 99032N, 2016, pp. 99032N-1-99032N-6.



Published by International Frequency Sensor Association (IFSA) Publishing, S. L., 2017.
(<http://www.sensorsportal.com>).

Easy and quick sensors systems development



- 16 measuring modes
- Frequency range from 0.05 Hz up to 7.5 MHz (120 MHz)
- Programmable accuracy from 1 % up to 0.001 %
- RS232 (USB optional)

sales@sensorsportal.com
http://www.sensorsportal.com/HTML/E-SHOP/PRODUCTS_4/Evaluation_board.htm

Aims and Scope

Sensors & Transducers is established, international, peer-reviewed, open access journal (print and electronic). It provides the best platform for the researchers and scientist worldwide to exchange their latest findings and results in science and technology of physical, chemical sensors and biosensors. The journal publishes original results of scientific and research works related to strategic and applied studies in all aspects of sensors: reviews, regular research and application specific papers, and short notes. In comparison with other sensors related journals, which are mainly focused on technological aspects and sensing principles, the *Sensors & Transducers* significantly contributes in areas, which are not adequately addressed in other journals, namely: frequency (period), duty-cycle, time-interval, PWM, phase-shift, pulse number output sensors and transducers; sensor systems; digital, smart, intelligent sensors and systems designs; signal processing and ADC in sensor systems; advanced sensor fusion; sensor networks; applications, etc. By this way the journal significantly enriches the appropriate databases of knowledge.

Sensors & Transducers journal has a very high publicity. It is indexed and abstracted very quickly by Chemical Abstracts, EBSCO Publishing, IndexCopernicus Journals Master List (ICV=6.13 in 2011), ProQuest Science Journals, CAS Source Index (CASSI), Ulrich's Periodicals Directory, Scirus, Google Scholar, etc. Since 2011 to 2014 *Sensors & Transducers* journal was covered and indexed by EI Compendex (CPX) index (including a Scopus, Embase, Engineering Village and Reaxys) in Elsevier products. The journal is included in the IFSA List of Recommended Journals (up-dated 9.12.2015), which contains only the best, established sensors related journals.

Topics of Interest

Include, but are not restricted to:

- Physical, chemical sensors and biosensors
- Digital, frequency, period, duty-cycle, time interval, PWM, pulse number output sensors and transducers
- Theory, principles, effects, design, standardization and modelling
- Smart sensors and systems
- Intelligent sensors and systems
- Sensor instrumentation
- Virtual instruments
- Sensors interfaces, buses and networks
- Signal processing, sensor fusion
- Remote sensing
- Frequency (period, duty-cycle)-to-code converters, ADC
- Technologies and materials
- Nanosensors and NEMS
- Microsystems
- Applications

Further information on this journal is available from the Publisher's web site:
http://www.sensorsportal.com/HTML/DIGEST/New_Digest.htm

Free Access and Subscriptions

Sensors & Transducers is the open access journal. All single articles are available for free download (article by article) without any registration and embargo period. For those who want to get the full page journal issue in print and/or pdf format there is an annual subscription. It includes 12 regular issues and some special issues. Annual subscription rates for 2016/2017 are the following: Electronic version (in printable pdf format): 590.00 EUR; Printed with b/w illustrations: 950.00 EUR; 15 % discount is available for IFSA Members.

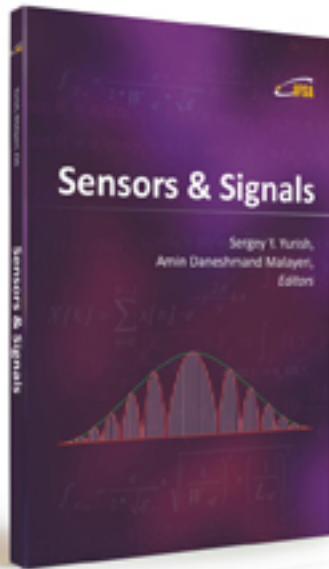
Further information about subscription is available on the IFSA Publishing's web site:
http://www.sensorsportal.com/HTML/DIGEST/Journal_Subscription.htm

Advertising Information

If you are interested in advertising or other commercial opportunities please download our Media Planner 2016:
http://www.sensorsportal.com/DOWNLOADS/Media_Planner_2016.pdf

Instructions for Authors

http://www.sensorsportal.com/HTML/DIGEST/Guides_for_Authors.htm



Sensors & Signals

Sergey Y. Yurish,
Amin Daneshmand Malayeri,
Editors

Sensors & Signals is the first book from the Book Series of the same name published by IFSA Publishing. The book contains eight chapters written by authors from universities and research centers from 12 countries: Cuba, Czech Republic, Egypt, Malaysia, Morocco, Portugal, Serbia, South Korea, Spain and Turkey. The coverage includes most recent developments in:

- Virtual instrumentation for analysis of ultrasonic signals;
- Humidity sensors (materials and sensor preparation and characteristics);
- Fault tolerance and fault management issues in Wireless Sensor Networks;
- Localization of target nodes in a 3-D Wireless Sensor Network;
- Opto-elastography imaging technique for tumor localization and characterization;
- Nuclear and geophysical sensors for landmines detection;
- Optimal color space for human skin detection at image recognition;
- Design of narrowband substrate integrated waveguide bandpass filters.

Each chapter of the book includes a state-of-the-art review in appropriate topic and well selected appropriate references at the end.

With its distinguished editors and international team of contributors *Sensors & Signals* is suitable for academic and industrial research scientists, engineers as well as PhD students working in the area of sensors and its application.



Order: http://www.sensorsportal.com/HTML/BOOKSTORE/Sensors_and_Signals.htm



www.sensorsportal.com

ISSN 2306-8515



9 772306 851006